

TECHNISCHE
UNIVERSITÄT
DRESDEN



Physical vapour deposition of Perovskite for solar cell application

Dissertation
zur Erlangung des akademischen Grades
Doctor rerum naturalium
(Dr. rer. nat.)

vorgelegt von

M. Sc. Martin Kroll
geboren am 20.07.1990 in München

Dresden Integrated Center for Applied Physics and Photonic Materials (IAPP)
und Institut für Angewandte Physik
Fakultät Physik
Technische Universität Dresden
2022

Eingereicht am 19. Juli 2022

1. Gutachter: Prof. Dr. Karl Leo
Institut für Angewandte Physik
Technische Universität Dresden
2. Gutachter: Prof. Dr. Frank Schreiber
Institut für Angewandte Physik
Universität Tübingen

Kurzfassung

Hybride Metall-Halogen Perowskit basierte Solarzellen haben im letzten Jahrzehnt eine noch nie dagewesene Entwicklung hinsichtlich ihrer Effizienzsteigerung erzielt. Dies ging mit einem rapiden Anstieg des Interesses der Forschungsgemeinschaft einher. Ein wichtiger Faktor für die Realisierung von Forschungsergebnissen ist der Übergang von Laborskalen zu industriellen Dimensionen, was grundlegende Anpassungen im Herstellungsprozess notwendig macht. Hier hat sich die physikalische Gasphasenabscheidung für andere Materialklassen bereits als gute Lösung bei der Herstellung von qualitativ hochwertigen Dünnschichten erwiesen.

In dieser Arbeit wird die Vakuumabscheidung von $\text{FA}_{1-x}\text{Cs}_x\text{PbI}_{3-x}\text{Br}_x$ für die Anwendung in Solarzellen durch Dreiquellenkoverdampfung erforscht. Durch eine Kombination aus optischen und Röntgen-basierten Messverfahren konnte eine Veränderung der Aufnahme des organischen Halogensalzes, Formamidiniumiodid (FAI), in die Perowskitverbindung in Abhängigkeit vom Kammerdruck festgestellt werden. Dadurch tritt eine Stöchiometrieänderung auf, welche sich in einer Bandlückenverschiebung niederschlägt. Außerdem wurde eine Veränderung der Kristallorientierung beobachtet. Diese Ergebnisse motivieren eine genauere Untersuchung des Verdampfungsverhaltens des organischen Halogensalzes. Mit Hilfe von Massenspektrometriemessungen und einer detaillierten Erfassung der Prozessparameter konnte eine Zersetzung von FAI während der Verdampfung festgestellt werden. Desweiteren wurden weitere Besonderheiten im Abscheideverhalten, wie zum Beispiel Verdampfungsgrenzen und Veränderungen des Toolingfaktors beobachtet. Die Ergebnisse leisten einen wesentlichen Beitrag zum tieferen Verständnis der Vakuumabscheidung von organisch-inorganischen Metall-Halogen Perowskiten.

Abstract

In the last decade, hybrid metal halide perovskite-based solar cells have enjoyed an unprecedented surge in development within the research community. The next steps to further improve this technology will involve the transition from the laboratory to commercial-scale production, which will require adjustments in their fabrication processes. Here, physical vapour deposition has proven to be a good option for the fabrication of high-quality thin films for perovskites and other materials, like organic semiconductors.

In this work, triple-source co-evaporation deposition of $\text{FA}_{1-x}\text{Cs}_x\text{PbI}_{3-x}\text{Br}_x$ for the production of thin films for solar cell applications is investigated. With a combination of optical and X-ray-based measurement methods, a decrease in the incorporation of the organic halide salt formamidinium iodide (FAI) was found with increasing background pressure. This decrease results in a change in stoichiometry of the compound and, with it, a shift of the band gap. Furthermore, a change in crystallite orientation was observed. These findings motivate the examination of the evaporation behaviour of formamidinium iodide in more detail. With mass spectrometry measurements and detailed tracking of the process parameters, a degradation of FAI during evaporation was found. Furthermore, several effects of the deposition behaviour, evaporation limits, and tooling shifts were observed. These findings will be substantial for the deeper understanding of vacuum deposition of organic-inorganic metal halide perovskites, and will be significant in the expansion of perovskite-based solar technology.

List of publications

- Enhancing Luminescence Efficiency by Controlled Island Formation of CsPbBr₃ Perovskite;
T. Antrack, M. Kroll, L. Merten, M. Albaladejo-Siguan, A. Hinderhofer, O. V. Konovalov, M. Jankowski, J. Benduhn, F. Schreiber, Y. Vaynzof, K. Leo; *Advanced Optical Materials*; 2022 (Submitted)
- Size and Dimensionality Effects on Hot Carrier Cooling in Lead Halide Perovskite Nanomaterials;
B. Carwithen, T. Hopper, Z. Ge, N. Mondal, X.- Zheng, F. Krieg, F. Montanarella, G. Nedelcu, M. Kroll, J. Frost, K. Leo, Y. Vaynzof, M. Bodnarchuk, M. Kovalenko, A. Bakulin; *Nano Letters*; 2022 (Submitted)
- Insights into the Evaporation Behaviour of FAI: Material Degradation and Consequences for perovskite solar cells;
M. Kroll, S. Öz, Z. Zhang, R. Ji, T. Antrack, Y. Vaynzof, S. Olthof, K. Leo; *RSC Sustainable Energy and Fuels*; 2022
- Optical Properties of Perovskite–Organic Multiple Quantum Wells;
T. Antrack, M. Kroll, M. Sudzius, C. Cho, P. Imbrasas, M. Albaladejo-Siguan, J. Benduhn, L. Merten, A. Hinderhofer, F. Schreiber, S. Reineke, Y. Vaynzof, K. Leo; *Advanced Science*; 2022 (Accepted)
- Control of Emission Characteristics of Perovskite Lasers through Optical Feedback;
A. Palatnik, C. Cho, C. Zhang, M. Sudzius, M. Kroll, S. Meister, K. Leo; *Advanced Photonics Research*; 2021
- Roadmap on Organic–Inorganic Hybrid Perovskite Semiconductors and Devices;
L. Schmidt-Mende et al.; *APL Materials*; 2021
- Electrical Pumping of Perovskite Diodes: Toward Stimulated Emission;
C. Cho, T. Antrack, M. Kroll, Q. An, T. Bärschneider, A. Fischer, S. Meister, Y. Vaynzof, K. Leo; *Advanced Science*; 2021
- Efficient Thermally Evaporated γ -CsPbI₃ Perovskite Solar Cells;
Z. Zhang, R. Ji, M. Kroll, Y. Hofstetter, X. Jia, D. Becker-Koch, F. Paulus, M. Löffler, F. Nehm, K. Leo, Y. Vaynzof; *Advanced Energy Materials*; 2021

- Purely Organic Microparticles Showing Ultralong Room Temperature Phosphorescence;
H. Thomas, F. Fries, M. Gmelch, T. Bärschneider, M. Kroll, A. Vavaleskou, S. Reineke; *ACS omega*; 2021
- Thermally Evaporated Methylammonium-free Perovskite Solar Cells;
R. Ji, Z. Zhang, C. Cho, Q. An, F. Paulus, M. Kroll, M. Löffler, F. Nehm, B. Rellinghaus, K. Leo, Y. Vaynzof; *Advanced Energy Materials*; 2020

List of Conference contributions

- DPG-Frühjahrstagung Regensburg 2019: Vacuum-deposited Bismuth and 2D Perovskites as Absorber Material for Solar Cells
- NanoGe Sevilla 2020: Lead-free co-evaporated Perovskites for Solar cell application
- MRS Boston 2021: Understanding the Thermal Evaporation of FAI for Perovskite Solar Cells

Contents

| | |
|--|----|
| Kurzfassung | iv |
| Abstract | v |
| List of publications | vi |
| 1. Introduction | 1 |
| 2. Theoretical background | 5 |
| 2.1. Basics of thin-film solar cells | 5 |
| 2.2. Status of current thin-film solar cell technologies | 7 |
| 2.3. The Perovskite system | 13 |
| 2.4. Organic-inorganic mixed-halide metal perovskites | 14 |
| 2.5. Deposition methods of metal halide perovskite | 18 |
| 2.6. Vacuum deposition of perovskite | 21 |
| 3. Experimental methods | 27 |
| 3.1. Physical vapor deposition | 27 |
| 3.2. Vacuum deposition of perovskite layers | 29 |
| 3.3. Analytical techniques | 32 |
| 4. Pressure dependent triple-source co-evaporation of methylammonium-free perovskite | 39 |
| 4.1. Precursor purification | 40 |
| 4.2. Film deposition procedure | 42 |
| 4.3. Crystallographic characterisation | 43 |
| 4.4. Optical characterisation | 49 |
| 4.5. Incorporation of FAI into thin-films | 50 |
| 4.6. Photovoltaic devices | 51 |
| 4.7. Summary | 55 |
| 5. Evaporation properties of formamidinium iodide | 57 |
| 5.1. Degradation reactions of formamidinium iodide | 57 |

Contents

| | |
|---|-----------|
| 5.2. Evaporation behaviour of formamidinium iodide | 58 |
| 5.3. Theoretical considerations during the deposition process | 61 |
| 5.4. Tooling behaviour of Formamidinium iodide | 63 |
| 5.5. Summary | 68 |
| 6. Summary & Outlook | 71 |
| A. Appendix | 75 |
| List of Figures | 81 |
| List of Tables | 82 |
| List of Abbreviations | 86 |
| Bibliography | 86 |

1. Introduction

The most intriguing question for the development of human society has been the issue of energy sources. The first humans used crude campfires for warmth and light and moved on to burning candles and animal fats and oils as civilisation progressed. More recently, in the past two centuries, fossil fuels like coal and oil have been used in ever-increasing quantities. It has, unfortunately, become apparent that the use of these fossil fuels causes irrevocable damage to our environment. With the population and demand for energy increasing, the planet is being pushed to its limits. The consumption of non-renewable energy sources is heating up the planet, bringing irreversible climate changes that will keep affecting humankind for the next centuries. After decades of careless energy consumption, much of the world has realised that the biggest challenge of the imminent future is to curb man-made global warming. The international agreement of the climate conference in Paris in 2015 to limit the collateral temperature increase to 1.5 °C. To achieve this crucial objective, a transition towards renewable energy sources is inevitable. All renewable energy sources, e.g. wind energy, water-based energy, biogas, and solar-radiation-based energy sources, are cornerstones of this transition and must be developed further.

Solar cell technology is one of the main building blocks on the path to a future based on renewable energies. Photoactive materials and their potential to produce voltage and current were discovered by several inventors in the late 19th century. Albert Einstein explained the mechanism behind these materials with his theory of the photoelectric effect in 1905 [1]. A major breakthrough for modern photovoltaics (PV) was made by the development of the silicon-based semiconductor industry in the 1950s. This technology made it possible to power the first satellites in the 1960s, and then in the 70s and 80s, it became commercially available for use in other sectors as well. Over the years, the efficiency of silicon solar cells increased, and the processing techniques of silicon wafers became more and more energy-efficient. This led to a sharp decrease in price per watt, making current photovoltaics accessible for private households. Nowadays, large MW-photovoltaic power plants can produce energy for only 3-5.5 ct/kWh, while small private roof-mounted systems produce energy for 6-

1. Introduction

11.5 ct/kWh [2]. Over the last decades, the price of PV modules has decreased by one order of magnitude about every ten years and has now reached a level of just a few cents per watt. At the same time, the volume of production is increasing such that more and more solar energy is produced every year. The price and cumulative output of the solar energy sector are depicted in Fig. 1.1a).

With the new German government's plan to increase the amount of installed power per year from 5 to 22.5 GWh, it will be necessary for the production of solar panels to increase simultaneously. The outline of this planning is shown in Fig. 1.1b). Since the decrease of the subsidisation of the German solar cell production in 2012, a lot of the primary production has moved to Asia, especially China, which now dominates the market for solar wafer production. This shift was due to the relatively low cost of energy from nuclear energy and coal for the energy-intensive production of high-purity silicon wafers in China. Production in Europe was not profitable anymore. The European production of solar panels will need to follow new technologies to reenter the global market and to fulfil the need of humanity for a future with limited global warming.

One of the most promising technologies for the future are thin-film solar cells. Although these devices are still lagging behind conventional silicon-based solar cells in terms of overall production, their market share is growing every year, opening up a lot of new possible applications. The leading established thin-film solar cells are based on CdTe and copper indium sulfide (CIS). Furthermore, innovative technologies like solar cell foils based on organic semiconductors are about to enter the market.

Over the last decade, a new material system has caught the attention of the research community. This system, known as perovskite, combines the advantages of both inorganic and organic semiconductors. Perovskite is the name of an already well-known material class of mineral, which has now been discovered to have many advantageous properties to change the solar cell market. Metal halide perovskites have increased their power conversion efficiency (PCE) since the first publication of a 3.8% solar cell by Kojima et al.[3] to 25.7% [4] by the UNIST within a little more than a decade. This increase in efficiency is unprecedented for any photovoltaic technology developed before. Organic-inorganic halide lead perovskite combines the advantages of both the inorganic and organic world of photovoltaic materials. It has the high optical absorption and charge carrier mobility of direct inorganic semiconductors, but their ease of production resembles that of organic semiconducting materials. These include the

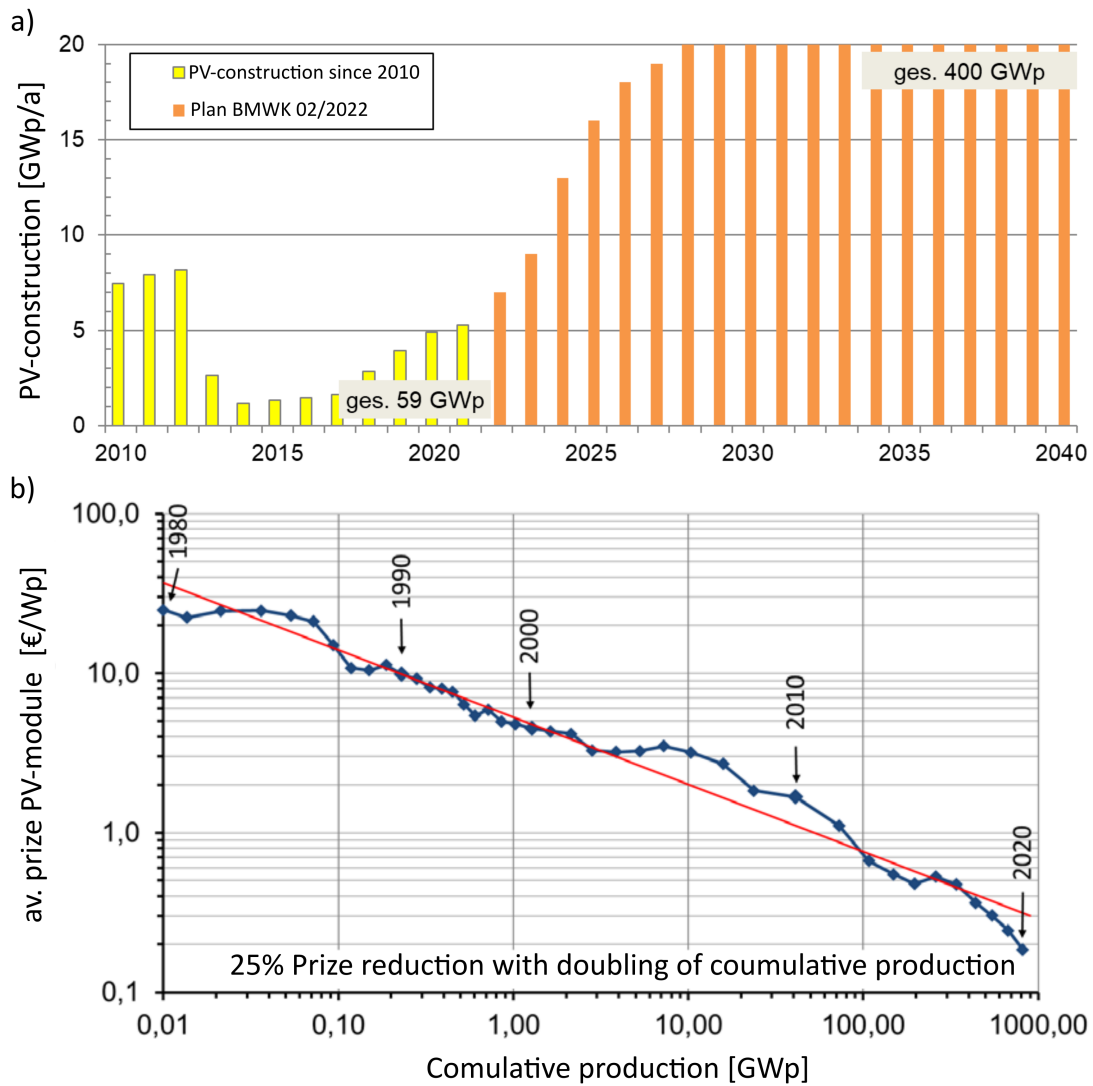


Figure 1.1.: a) Planned photovoltaic construction according to the Bundesministerium für Wirtschaft und Klimaschutz, b) prize development of photovoltaic modules [2].

1. Introduction

possibility of processing thin films from solution or by low-temperature evaporation.

With perovskite's promising properties and their rapid development on the lab scale, a transition to industrial-scale production is the next big step needed for their introduction into the solar cell market. Vacuum deposition has been proven here to be the best deposition technique for up-scaling the production of organic solar cells and light-emitting devices [5, 6]. For metal halide perovskites, vacuum deposition has also shown very promising results. Important works contributing to this include the first breakthrough by Liu et al.[7] in 2013, where a PCE of 15% was reported, and the first device with over 20% efficiency by Momblona et al. in 2016 [8]. In the last years, the transition to larger-scale devices has also shown encouraging results. The work of Li et al.[9] in 2020 described the first efficient mini-modules, and large-area films by Feng et al.[10] in 2021 are prime examples. However, one of the rarely-mentioned key issues with perovskite devices is the reproducibility and process stability of the vacuum deposition process. These problems need to be solved for future commercialisation since an industrial production line has no tolerance for variations in the final product.

These issues lead to the main focus of this work: What is happening during the evaporation, and what are factors that have to be taken into account during the evaporation process? The focus of this study is on the production of inorganic-organic mixed-halide perovskites without the addition of methylammonium. In particular, the evaporation properties of the record-efficiency material formamidinium iodide are investigated[11].

2. Theoretical background

This work focuses on vacuum-deposited perovskite solar cells. For a deeper insight into this topic, an understanding of several basic principles is necessary. First, the basics of solar energy conversion and thin-film solar cells are explained. This is followed by a description of the perovskite system and the properties of metal halide perovskites. Then, the vacuum deposition of perovskite and the characteristics of this material are introduced. A good understanding of these topics is necessary to follow the scope of this thesis.

2.1. Basics of thin-film solar cells

Thin-film solar cells are the second generation of photovoltaic technology after the conventional silicon-based solar cells, which are not described in more detail here [12]. For the description of thin-film solar cells, the general concept of solar energy conversion is first described, and then the focus is laid on the implementation of this concept in thin-film devices.

2.1.1. Solar energy conversion

The photoelectric effect is the ground laying principle of solar energy conversion, producing electrical energy from solar radiation. Three underlying conditions have to be fulfilled:

- The incident radiation, in general sunlight, has to be absorbed
- The light absorption has to generate mobile positive and negative charge carriers
- The charge carriers must be separated to generate potential and current, and with it, electrical energy.

Most semiconducting materials fulfil the first two conditions. An incoming photon with sufficient energy is absorbed by transferring its energy to an electron

2. Theoretical background

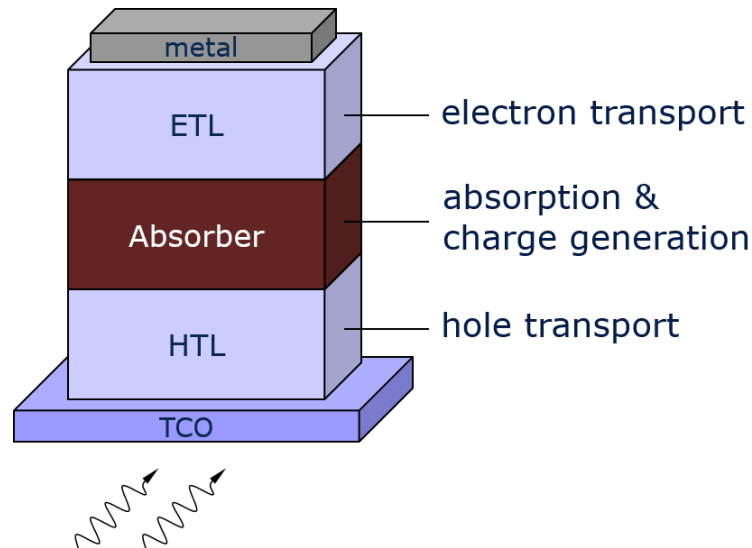


Figure 2.1.: Typical device stack for a thin-film solar cell with bottom illumination in p-i-n structure.

in the valence band, thus exciting it into the conduction band. The thereby generated electron-hole pair is either bound, a so-called exciton, or mobile and has to be separated in either case. The separation can be realised by putting two different semiconductors together (a heterojunction) or varying the doping level within a single semiconductor (a homojunction). The electron-hole pair is then split at the interface between materials, and both charges must be guided to front and back contact, respectively. These three processes: absorption, charge carrier generation, and separation and extraction, must be optimised for efficient devices.

2.1.2. Structure of thin-film solar cells

In contrast to conventional silicon-based solar cells, where functional layers are implanted or deposited on top or bottom of thin monocrystalline wafers, thin-film solar cells are deposited directly onto a substrate. This makes all thin-film solar cell technologies multilayer systems with sequentially processed, thin, functional films. A typical structure for a thin-film solar cell with bottom illumination is shown in Fig. 2.1. In general, this cell type has the following layers. Glass is the most common substrate material, but flexible polymer substrates [13, 14, 15] or metal sheets [16], which then work as electrical back contact, are also possible. For a solar cell with bottom illumination, a transparent conductive material is deposited as the first layer. The conduction layer can be a transparent conductive

oxide (TCO), which is sputtered on the substrate [17] or metallic nanostructures, for example wires [18] or thin films [19]. Common TCO materials are indium tin oxide (ITO), a mixture of indium oxide and tin oxide, or fluorine-doped tin oxide (FTO). In most cases, silver is used as a metal electrode, but gold and aluminium are also possible. This layer has to be optimised for low electrical resistance and high light transmittance across the desired spectrum. For a solar cell with a p-i-n structure, as is displayed in Fig. 2.1, the transparent electrode is followed by a charge selective transport layer, in this case, the hole transport layer. This hole-transporting layer (HTL) can consist of a metal oxide, like NiO or CuO, but organic semiconductor layers are also common. Here, a variety of materials have been investigated [20, 21]. For a device to work properly, the energy alignment with respect to the absorber layer has to be optimised to avoid charge blocking [22] and recombination [23]. A high material conductivity for an efficient charge extraction is beneficial [24]. The next layer in the thin-film device is the light-absorbing layer. This generally consists of a bilayer that absorbs the incoming light and separates the electrons and holes generated. The type of material used here varies depending on the thin-film technology. The electron transport layer follows the active layer. Here, fullerenes like C₆₀ or PCBM, or other organic materials are often used, since the high processing temperatures or a sputtering process for inorganic layers can damage the absorber layer. The electron transport layer underlies the same energy alignment and conductivity conditions as the hole transport layer. Finally, the back contact is deposited. This is usually a thin layer of metal that has a well-fitting work function, high conductivity, and, if necessary, a high reflection for increased recycling of unabsorbed light [25]. Other functional thin films can be inserted between these layers, like charge-selective blocking layers [26] or passivation layers [27] to reduce carrier recombination. Furthermore, anti-reflection coatings [28] or coupling structures [29, 30] can be used to increase light absorption. Each of these layers has to be optimised and adjusted for high-efficiency thin-film solar cells.

2.2. Status of current thin-film solar cell technologies

This section gives an overview of existing thin-film solar cells and their functionality, along with future technologies which are still under development. Today's most prevalent photovoltaic technology is based on monocrystalline silicon. The solar modules are cut from large monocrystals, or ingots, and are between 150 and 200 μm thick. These ingots are produced by the Czochralski method

2. Theoretical background

[31] from a silicon melt. Due to the high melting point of silicon, this process is very energy-intensive, thereby limiting this technology's cost efficiency. Currently, passivated emitter and rear cells (PERCs) are most common in the solar cell market [32]. Rear contact passivation reflects otherwise unused red and infrared light back into the solar cell, making it accessible for energy harvesting. This technology has improved the device efficiency to over 22% [33]. Although cells produced by this working principle still dominate the market, new possibilities and advantages are accessible with thin-film solar cells or the second/third generation of photovoltaic devices. The current status of these technologies will be presented in the following.

2.2.1. Existing thin-film solar cell technologies

Thin-film solar cells are referred to as the second generation of photovoltaic technologies after those based on Si, and in recent years their power conversion efficiency has improved significantly. It is now higher than polycrystalline silicon-based photovoltaics, and for some technologies now ranges in the region of monocrystalline silicon solar cells [34]. This increased efficiency, together with a lower energy consumption during production, reduces the energy amortisation time. Consequently, thin-film solar cells are already a greener energy source than conventional photovoltaics [35].

Three different thin-film technologies evolved to a substantial market share in the current solar cell economy. With about a market share of roughly 5%, cadmium telluride solar cells are now the most successful technology [36]. First reported by Bonnet and Rabenhorst in 1972 [37] with an efficiency of 6%, current lab-scale devices reach an efficiency of 21.0% and commercial modules around 19% [36].

Industrial-scale CdTe solar cells are usually produced with different vacuum deposition techniques on either thin soda-lime glass sheets or flexible polymer substrates using a sputtered TCO layer as the front contact. The most commonly used deposition technique is a high-rate vapour transport deposition process. This involves a carrier gas transporting Cd and Te₂ vapour onto a heated substrate, where it then condenses to form a uniform thin film. A heterojunction is formed by deposition of a p-type window layer of cadmium sulfide (CdS) on an underlying n-type absorber material. The cell is finished with a metal back contact [38, 39]. CdTe solar cells are now the cheapest and most energy-efficient solar cells on the market, with an energy payback time of as little as 0.5 years [40]. Unfortunately, CdTe has some problematic drawbacks. These include the high

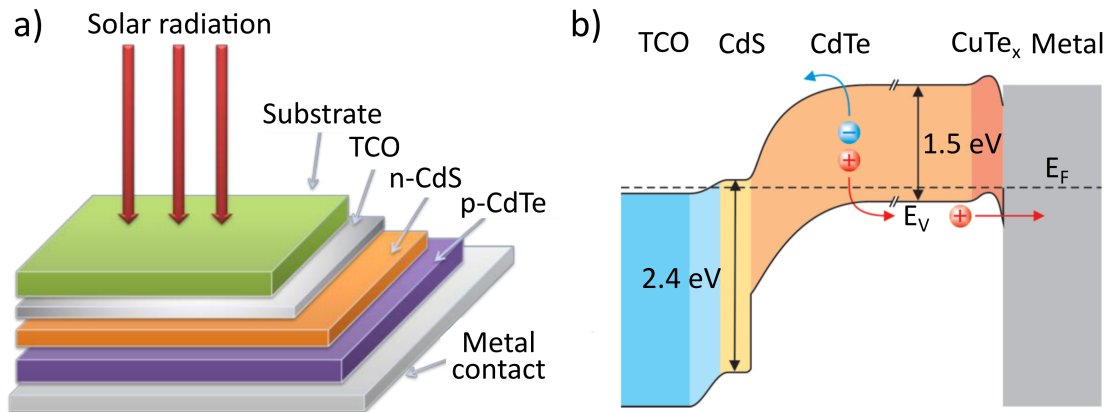


Figure 2.2.: Working principle of a CdTe thin-film solar cell: a) Exemplary stack of CdTe solar cells and b) the band structure of the device, reproduced from Kapadnis et al.[38] and Perrenoud et al.[39].

toxicity of cadmium, which raises issues in regard to public health and waste disposal. Another downside is the scarcity of tellurium. This element is as rare as platinum, which increases production costs and complicates upscaling [41, 42].

The second-largest thin-film technology is based on copper indium gallium diselenide (CIGS, chemical formula $\text{CuIn}_x\text{Ga}_{(1-x)}\text{Se}_2$), with a market share of approximately 1.5% [36]. A typical way to produce CIGS solar cells is by co-evaporation, comparable to the deposition process of perovskite explained in Sec. 2.6. The absorber material is deposited on a substrate with a molybdenum back contact, usually as a p-type semiconductor. After an alkali post-treatment, a thin n-doped buffer layer of CdS is added from a chemical bath. The cell is finished with an aluminium-doped zinc oxide (ZnO) layer as a conductive window material and a nickel/aluminium grid as electrical front contact [43, 44]. With this configuration, SolarFrontier reached a PCE of 22.3% for a lab-scale device of 0.5 cm²[45] and large modules have efficiencies of over 19% [46]. The issue of toxic waste presents itself again with these cells, as they contain cadmium. Furthermore, acquisition of the indium components is problematic, since it is as rare as tellurium and is also in demand in other types of semiconductor devices. Other noteworthy thin-film photovoltaic technologies include those based on amorphous silicon (α -Si) and gallium arsenide (GaAs). Both have severe disadvantages for commercial realisation. α -Si has shown insufficient stability and relatively low efficiencies, and GaAs, though being the most efficient of all thin-film technologies, is too expensive for conventional use so is only implemented in space-related applications.

2.2.2. Emerging solar cell technologies

While the second generation of solar cells increases its footprint in the growing market, the third generation is already in the starting gate. This technology is also based on thin-films, but different absorber materials are used. The next one to enter the market are solar modules based on organic semiconductors. In contrast to the previously mentioned inorganic materials, the functional layers here are made from hydrocarbon compounds, like polymers or small aromatic molecules. They show semiconducting properties due to the delocalisation of their electrons over the molecule. In contrast to inorganic semiconductors, the materials are usually amorphous due to a lower intermolecular interaction. In this material class, excited electron-hole pairs are bound more strongly due to a lower dielectric constant of the organic materials and can not move as freely as in inorganic crystals. These so-called excitons have to be separated to produce electrical energy. Like in conventional solar cells, this separation is facilitated by bringing the absorber layer in contact with a different material, a so-called acceptor layer, that encourages charge separation. This heterojunction is then sandwiched between electron- and hole-selective transport layers to extract the separated charges to the electrodes. These layers usually consist of a TCO and a metal back contact. By using different molecule mixtures, the light-absorbing properties can be tuned to adjust them to the desired absorption, making it possible to build transparent devices. The highest efficiency achieved with organic thin-film solar cells right now is 18.2% [47], so slightly lower than the inorganic modules presented beforehand. With growing demand and exceptional versatility in applications, the market has been expanding over the recent years and is expected to grow further [48].

With organic solar cells already being realised, the next promising candidates for the future of photovoltaic technology are perovskite-based solar cells, which are the point of interest of this work.

2.2.3. Status of Perovskite solar cells

Success in the development of perovskite solar cells has skyrocketed in the last decade, with efficiencies approaching the Shockley-Queisser limit [49] for power conversion efficiency. In this section, a more general classification of this technology into the field of thin-film solar cells is given. After the first realisation of perovskite solar cells, a steep increase in PCEs between 2012 and 2015 led to efficiencies of over 20% [50, 51]. One problem in this field of research is that many

groups have recurring problems reproducing these results, despite relative simplicity of the process [52]. This gives insight to recurring problems in this field of research. Many important process parameters remain unknown, unpublished or overlooked. Some to mention here are soft parameters, like the distance of the pipette tip to the sample during spin coating, or the local atmosphere in the spin coater. These concerns are known to experienced researchers, but few published studies can be found on these topics. One of these factors has recently been published by Taylor et al.[53], where a comprehensive study about the application of the antisolvent was made. Further aspects that remain unmentioned batch-to-batch variations from inconsistent precursor quality, or the influence of fluctuating ambient conditions in the lab. The development of the perovskite research field is demonstrated by an open-access database project by Jacobssen et al.[54], where the authors collected data from various groups all over the world. These graphs, displayed in Fig. 2.3, are the result of the analysis of this data collection showing the often unmentioned problems of current perovskite research.

Although record-breaking devices are frequently reported, the overall average of device PCE is developing slowly, despite the fact that more and more samples are produced and characterised over the years. The majority of laboratory-produced devices are small, usually smaller than one cm², which makes upscaling the fabrication process to industrial standards the main focus of future research. And finally, the long term stability T_{80} , which indicates the time it takes for the efficiency to drop under 80% of the initial value, is still in the range of 100-1000 hours, which is not suitable for real-life applications.

Nonetheless, the fast development of the field has led to an early industrialisation of perovskite solar cells and perovskite-based tandem solar cells. There are currently four companies, located in England (Oxford P.V.), China (Microquanta Semiconductor) and the US (Hunt Perovskite Technologies, Energy Materials), that work on the realisation of perovskite solar cells as the newest generation for photovoltaics. Although these companies are famous for their secrecy, Oxford P.V. has published reports of tandem silicon devices with efficiencies close to the benchmark of 30% with a 2000h stability [55, 56].

The final problematic factor that will be discussed here is the presence of toxic heavy metals in perovskite solar cells. In contrast to the previously-mentioned cadmium in CdTe and CIGS solar cells, the highly toxic heavy metal lead is present in perovskite-based devices. This lead is in a water-soluble form, making it even more problematic for the environment and aquatic life. Other factors besides

2. Theoretical background

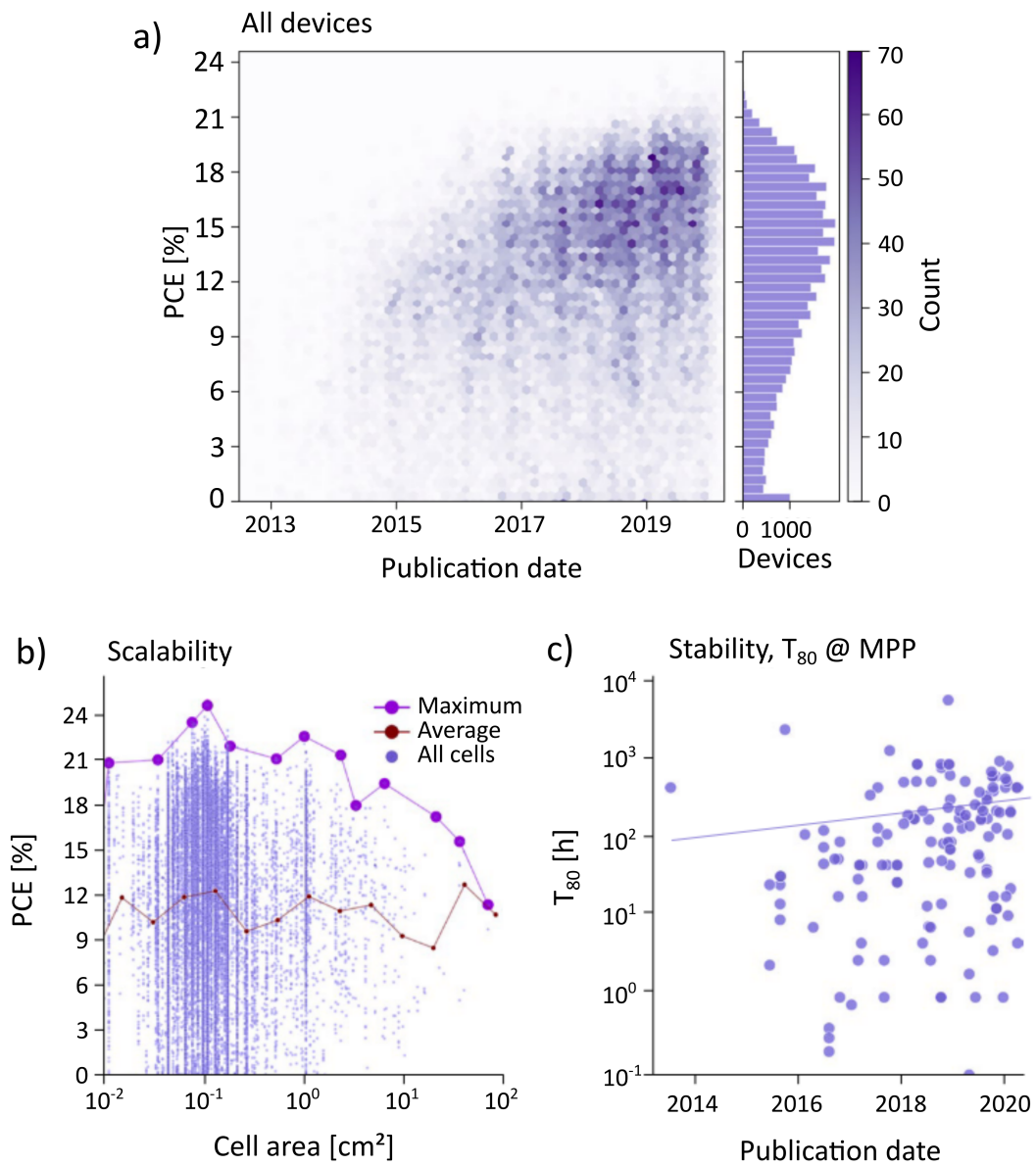


Figure 2.3.: Data analysis from the perovskite database-project: a) development of overall device efficiency, b) device efficiency depending on the active area, c) development of T_{80} stability under AM1.5 illumination and with maximum power point tracking, reproduced from Jacobssen et al.[54].

the toxicity also have to be taken into account, like the problematic and material-consuming synthesis of the transport layers of the best-performing configurations [57].

In conclusion, perovskite solar cells have experienced exceptional development over the last years, but some obstacles remain. This makes further research necessary, and the field is going from the hunt after new record efficiencies to now focus on stability, scalability and reproducibility, which could lead to the next breakthrough of this technology.

2.3. The Perovskite system

The main focus of this work are metal halide perovskites. Perovskites are a well-known class of semiconductor material which has caught a lot of interest in recent years. After being known for decades in other technologies like superconductors or ferroelectrics, metal halide perovskite is now one of the most promising materials to revolutionise the field of solar cells. Perovskites' unique structural characteristics, the semiconducting properties, and possibilities of compositional engineering, all make perovskite an excellent candidate for future photovoltaic technologies, as explained in the following.

2.3.1. Structure of Perovskite

The prototypical perovskite material is calcium titanium oxide CaTiO_3 . This material was first discovered by Gustav Rose in 1839 and is named after the Russian mineralogist Lev Perovski [58]. CaTiO_3 crystallises in a characteristic ABX_3 structure. Nowadays, the name "Perovskite" is used as a general term for all ABX_3 -compounds with the characteristic crystal structure. In this structure, a B-cation is surrounded by six X-anions, forming an octahedron with the B-cation in the centre. This cation is also surrounded by eight A-cations, holding the structure in place. The structure is displayed in Fig. 2.4.

The crystallisation in perovskite structure is dictated by the radii of the used elements. The bond lengths of the ionic bonds between A-X and B-X have to fulfil the tolerance criteria described by the Goldschmidt rule [59]:

$$t = \frac{(R_A + R_X)}{\sqrt{2}(R_B + R_X)} \quad (2.1)$$

with R_A , R_B and R_X the radii of the respective ions and t the Goldschmidt toler-

2. Theoretical background

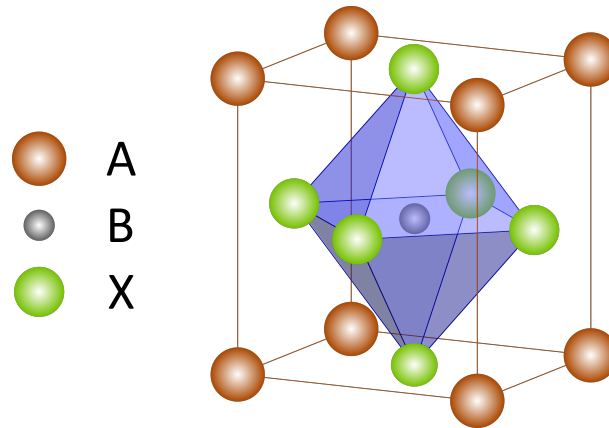


Figure 2.4.: Perovskite structure in orthorhombic crystallisation

ance factor. The value of t determines the crystal structure of the perovskite lattice. When $t > 1$, the structure is hexagonal or tetragonal, for $0.9 < t < 1$ a cubic structure is the most stable and for $0.71 < t < 0.9$, an orthorhombic or rhombohedral structure is formed. If $t < 0.71$, the criteria for a perovskite structure is no longer fulfilled, and it has to crystallise in a different structure [60].

2.4. Organic-inorganic mixed-halide metal perovskites

In contrast to the original perovskite material CaTiO_3 , metal halide perovskite is a monovalent system that can have a variety of different compounds as part of the crystal. On the A-site, small organic molecules like methylammonium (MA), formamidinium (FA) or inorganic caesium can fulfil equation 2.1. In small amounts, guanidinium (Ga) [61], and rubidium [62] can be incorporated into the crystal lattice. The B-site metal ion is generally lead, due to it having the ideal ion size and an electronic structure, that leads to a direct band gap semiconductor material. The slightly smaller tin atom has similar properties as lead so it can be used as well, although its required 2^+ oxidation state is not entirely stable. The X-position in the crystal is occupied by halide ions, in most cases iodine, but bromine or chloride can also be used. A further discussion on composition engineering can be found in Sec. 2.4.2.

Organic-inorganic mixed-halide metal perovskites have shown exceptionally advantageous properties. These include absorption over a wide spectral range [63], a tunable band gap [64], long diffusion lengths [65, 66], low recombination [67], and high charge carrier mobility [68]. Together with a low production cost, these properties have made this material class one of the most promising

candidates for future photovoltaic applications. One of the earliest of these devices came about in 2009, when Kojima et al.[3] first reported a functional photovoltaic cell with a methylammonium lead triiodide (MAPbI₃) absorber layer. This first device had a power conversion efficiency (PCE) of 3.8%. From these promising results, perovskite-based photovoltaic technology improved rapidly over the next years, with present record efficiencies of over 25% [11].

2.4.1. Semiconductor properties of metal halide perovskite

As mentioned beforehand, metal halide perovskite shows exceptionally advantageous semiconductor properties. The band gap of perovskite is mainly determined by the atomic states of the metal and the halide. In the case of lead halide perovskite, a direct band gap is formed. The valence band maximum is formed by the antibonding hybridised lead 6s orbital and the halides' 5p orbital. The antibonding conduction band minimum consists of the hybridised orbitals of lead 6p with the 5p of the halide. Due to a more ionic character of this orbital overlap, it is mainly determined by the 6p orbital of lead. This orbital splitting is illustrated in Fig. 2.5a). Density functional theory calculations (DFT) of these hybridised orbitals show a direct band gap. The calculated band structure of MAPbI₃ is depicted in Fig. 2.5b). Besides the direct band gap, metal halide perovskites exhibit a low exciton binding energy of 16 meV and an effective mass of the exciton of $\mu \sim 0.1m_0$ with m_0 being the free electron mass [71]. These three properties: the direct band gap, the low exciton binding energy, and low effective mass result in a very high absorption coefficient [63] and high charge carrier mobility [68], all of which are beneficial for efficient photovoltaic devices. Another favourable property of metal halide perovskites is a high defect tolerance, meaning that the energetic states induced by crystal defects are close to the band edges. The energetic levels of defects in CsPbBr₃ are depicted in Fig. 2.5. These shallow energy states are actually beneficial, as they do not introduce deep traps in the band gap, which would induce charge carrier recombination. Instead they work as doping states to induce more mobile charge carriers.

2.4.2. Compositional engineering for mixed-halide perovskites

Besides the excellent semiconductor properties described above, metal halide perovskite exhibits another useful property. Since several different elements can fulfil equation 2.1 to form a perovskite crystal lattice, and because the band gap of a compound depends on the orbitals of its atoms, the band gap of per-

2. Theoretical background

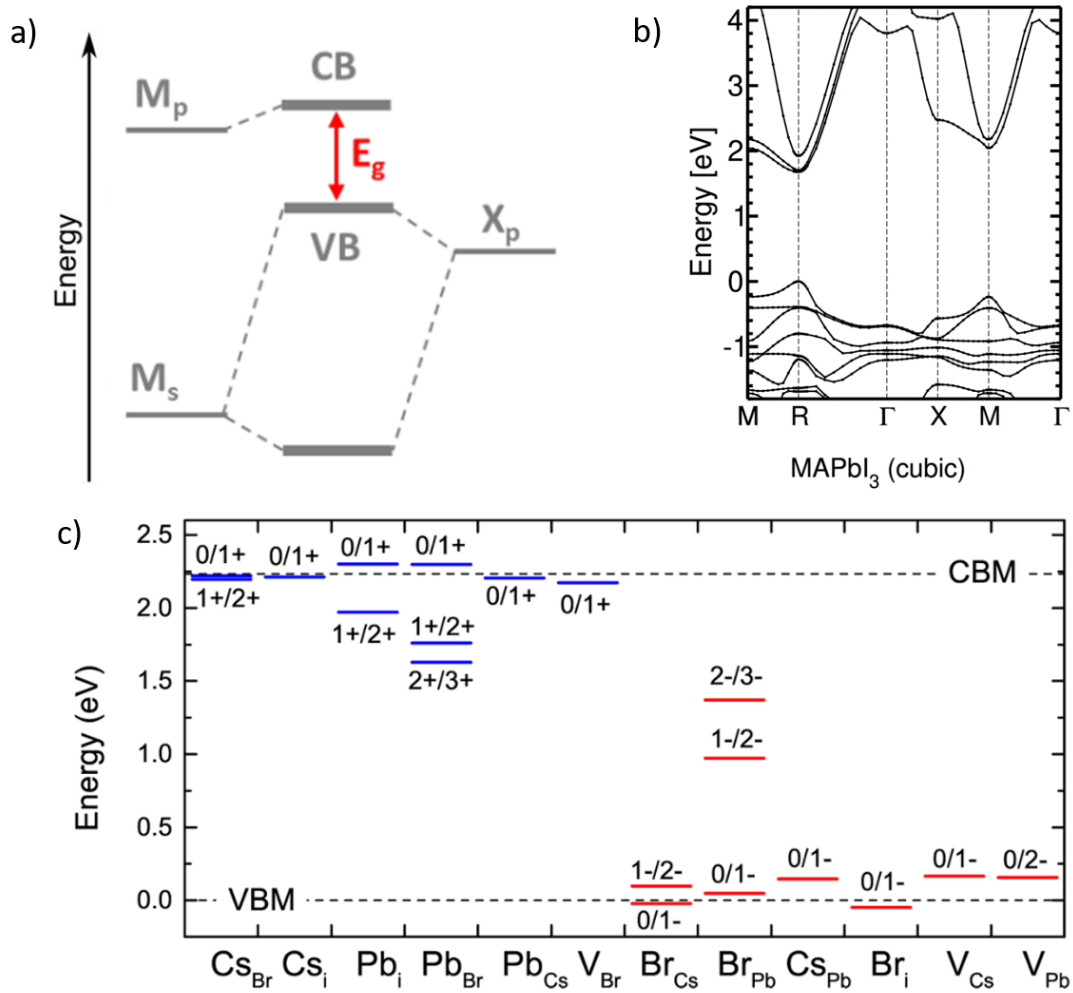


Figure 2.5.: a) An illustration of the origin of the perovskites band gap by the splitting of the hybridised metal-halide orbitals, reproduced from [69]; b) calculated band structure of MAPbI₃ with density functional theory (DFT) performed by Dr. Reinhard Scholz; c) Defect levels calculated with DFT for caesium lead bromide, reproduced from [70]

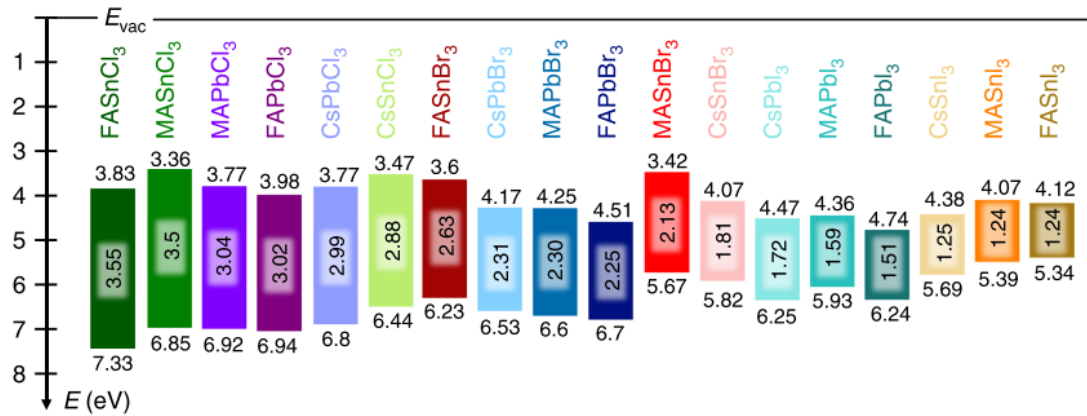


Figure 2.6.: Schematic of 18 metal halide perovskites with the respective ionisation energy, electron affinity and optical band gap, reproduced from Tao et al.[72]

ovskite can be tuned. Besides the optoelectronic properties, other important factors are influenced, like the material's long-term stability. These factors make perovskite-based materials very versatile, as explained in the following. A simple change of the precursors can give perovskite a wide range of different properties. For a substitution of the A-site cation, when the ionic radii of Pb^{2+} and I^- are considered as restrictions for the lattice, the possibilities are limited to organic molecules with two (methylammonium) or three (formamidinium) C-C and C-N bonds or the inorganic caesium atom. As explained in the section above, the energetical orbitals of the A-site cation do not contribute to the electronic states at the band edges, but the different size of the ions influences the semiconducting properties by the consequential change in lattice size. The band gap increases from the smallest ion caesium to the largest ion formamidinium. For lead iodide-based perovskite, this shift is about 200 meV [72]. When used in optoelectronic devices, the A-cation influences the resulting perovskite film in terms of stability [73], efficiency [74] and hysteresis [75]. The exchange of the B-cation from lead to the smaller tin has a similar effect on the crystal lattice and, with it, the band gap. The smaller tin ion reduces the band gap by about 350 meV. One problem of tin is the self-induced change of oxidation states from Sn^{2+} to Sn^{4+} , which induces degradation of the material since the doubling of the charge does not fulfil the requirements for the perovskites ABX_3 structure.

The most impactful way to customise the properties of perovskite, even more so than changing the A or B cation, is by changing the type of the halide. As explained in Sec. 2.4.1, the valence band maximum is highly influenced by the electronic state of the halide. By introducing bromide or chloride instead of io-

2. Theoretical background

dine, the band gap can be tuned from 1.59 eV to 3.06 eV [72] when going from pure iodine to pure chloride in methylammonium and lead-based perovskite. This effect can be observed by following the graph in Fig. 2.6 from left to right. By intermixing the ions mentioned above, continuous transitions of the optical band gap are possible. This mixing of different ions can unfortunately induce photoactivated halide segregation, which is a separation of the composite material into, for example, iodine and bromine-rich regions [76]. This demixing can induce unfavourable degradation and defects in the perovskite [77]. With careful adjustments, the properties of the perovskite can be tuned to fulfil the desired specifications for the application as a light absorber in a photovoltaic device and also for light emission in a perovskite-based LED.

2.5. Deposition methods of metal halide perovskite

The properties of metal halide perovskites are explained in the chapter above. Now the focus will be shifted to the methods used to fabricate perovskite. One of the big advantages of this material are the various production methods that can be used to produce high-quality, low-cost semiconducting material. After presenting the most prominent solution-based deposition methods, the focus will be shifted to vacuum-deposited perovskite and the influence of different evaporation parameters and effects during the deposition.

2.5.1. Spin coating process

The most common processing technique for perovskite thin-films is via spin coating. Here, the precursor salts are dissolved in polar aprotic solvents such as dimethylformamide (DMF) or dimethyl sulfoxide (DMSO) or a mixture of both. The precursor solution is then distributed uniformly on the substrate by spinning it at several thousand rotations per minute. Advantages of this technique are the relatively inexpensive equipment, a fast deposition, and a high throughput. This method offers several ways to control the crystallisation process. Some examples include the necessary annealing step [78, 79, 80], applying antisolvents [53, 81], or including additives to the solution [82, 83]. There are some drawbacks involved with the spin coating method. One of the biggest disadvantages is the limitation to lab-scale devices and the complexity of automatised processes. Furthermore, the material waste is high and toxic solvents are necessary.

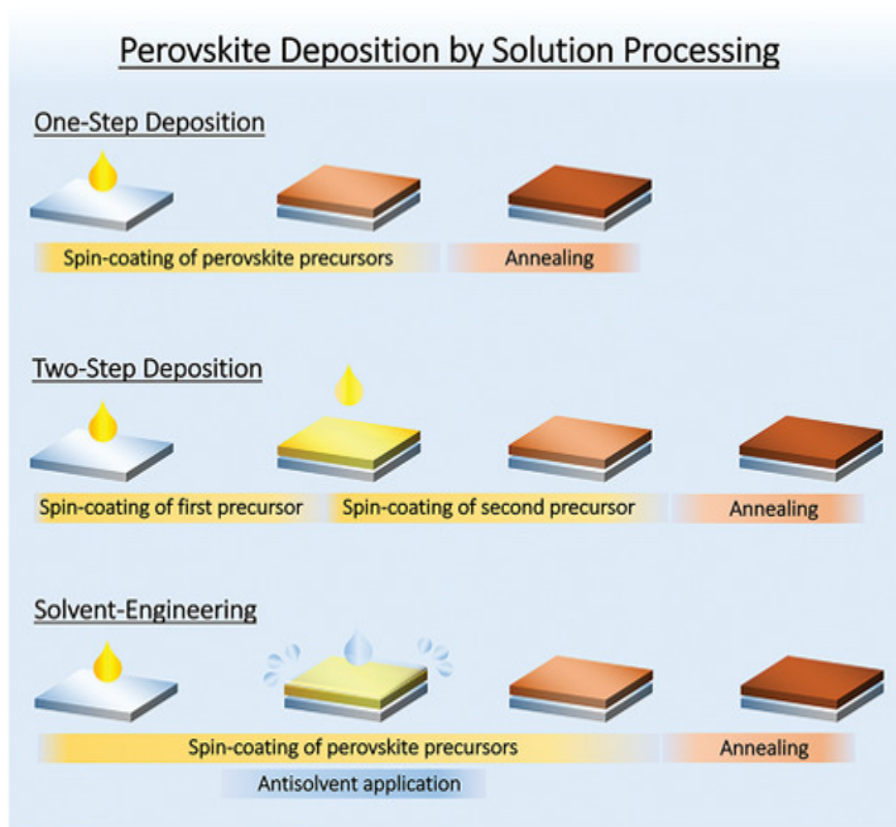


Figure 2.7.: Schematic illustration of different perovskite deposition methods via spin coating, reproduced from Vaynzof (2020) [84].

Over the recent years, several spin coating approaches have been found to obtain high-quality thin-films. The processes are illustrated in Fig. 2.7. First is the one-step deposition. Here, the precursor solution is deposited equally on the substrate, followed by an annealing step to evaporate the solvent and induce crystallisation [85]. This technique is not very common anymore but still finds application in certain recipes [86].

Another possibility to get high-performing perovskite films is by a two-step method. Here, an inorganic metal halide layer is prepared first, either by solution processing [87] or by vacuum deposition [88]. This layer is then converted into perovskite by applying a solution of A-cation salt to convert the metal halide into perovskite. With this method, an efficiency of 24% and high stability of over 2000 h has been achieved recently [89].

The most popular and commonly used deposition technique is the so-called solvent engineering method, where an antisolvent is applied during the spin coating of the film. This antisolvent removes the solvent and induces crystalli-

2. Theoretical background

sation of the perovskite [90]. A wide selection of antisolvents are available, and high precision in all steps of the preparation is required to yield high-quality films [53]. By optimising the deposition process and introducing additives to control the crystallisation process [81], as well as applying passivation layers at the interfaces of the active layer [27], high-efficiency devices with increasing stability and reproducibility can be produced. Latest advances have pushed the efficiency to over 25% [11], which shows that spin coating is a technique to achieve high-performing devices.

2.5.2. Scalable processes for perovskite deposition from solution

An important consideration in the field of solar cell science is whether a fabrication method can be upscaled for commercial mass production. Although most research groups focus on spin coating due to the cheap equipment cost and high throughput for small devices. It is not amenable to upscaling, since the substrate size is limited due to edge inhomogeneity appearing in the coated film [91]. Fortunately, there are several linear deposition techniques to solve these problems and allow coverage of large areas. The most promising techniques will be presented in the following.

In recent years, scalable processes like blade coating [92, 93], slot die coating [94] and inkjet printing [95] have been investigated in more detail for the preparation of perovskite thin-films and solar cells. Illustrations of these processing techniques are depicted in Fig. 2.8. Blade coating and slot die casting are meniscus guided deposition techniques. Here, the precursor solution is drawn over a moving, heated substrate, where the solution forms a film with decreasing thickness, the so-called meniscus. At the end of the meniscus, the solvent evaporates and the crystallisation begins. The crystallisation can be controlled by varying the deposition parameters, like the substrate temperature and the casting speed [96]. The working principle of these two techniques are shown in Fig. 2.8a) and b). For small area devices, efficiencies of 20% [92] and 18% [97] have been achieved with blade coating and slot-die casting respectively. Unfortunately, for devices $>10\text{ cm}^2$ the efficiency goes down to 15.3% [98] and 11.8% [99]. In contrast to the previously described techniques, inkjet printing is a contact-free deposition which offers the advantage of printing arbitrary patterns. Here, the solution is deposited via a piezoelectric print head and afterwards dried in vacuum and annealed. The process is illustrated in Fig. 2.8c). This technique results in small devices with up to 21% efficiency [95] and up to 13.3% for devices $> 1\text{ cm}^2$ [100, 101]. In conclusion, all these techniques have

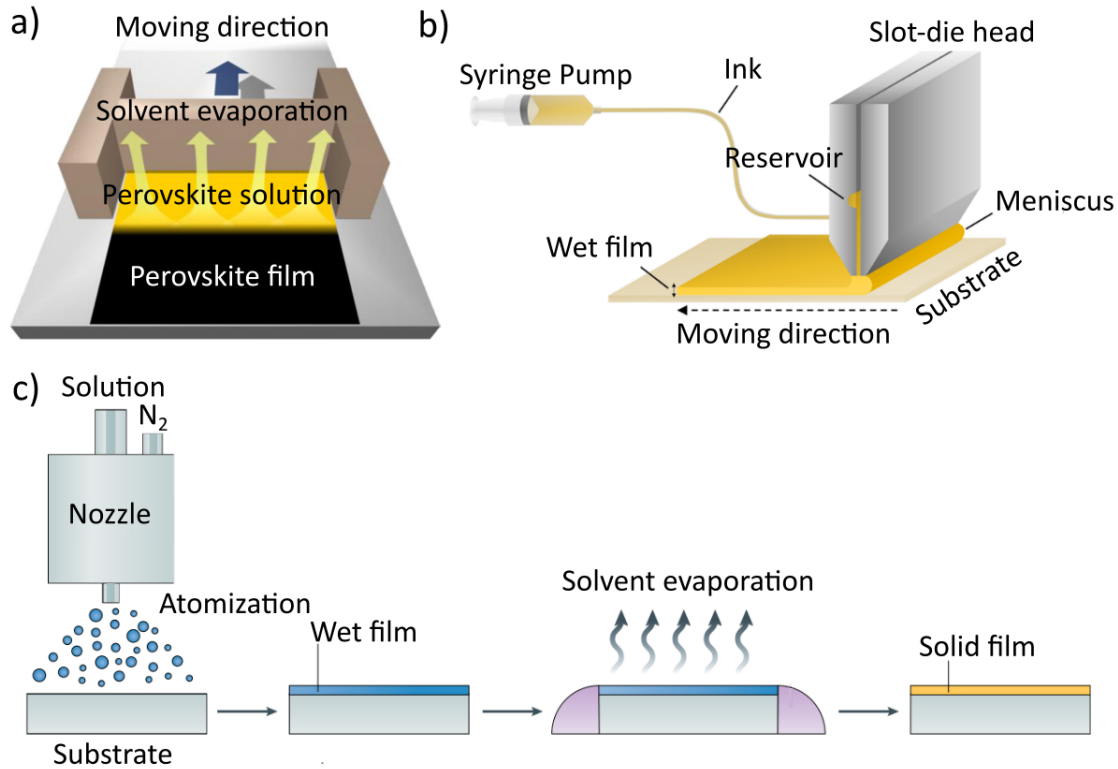


Figure 2.8.: Schematics of scalable linear solution processing techniques: a) blade coating, reproduced from Park et al.[102], b) slot die casting, reproduced from Patibar et al.[94], c) inkjet printing, reproduced from Park et al.[102]

the possibility to produce high-efficiency devices on the lab-scale but still have to prove their advantages for module-size photovoltaics.

2.6. Vacuum deposition of perovskite

Vacuum deposition is a well-established method for preparing thin-films, with applications ranging from organic LED displays [103], solid-state battery production [104] to packaging in food industry. In this section, this method is explained for the processing of metal halide perovskites and the influence of different process parameters, like the substrate material, the substrate temperature, and the deposition properties of the organic cation on the resulting thin-film. However, first, an introduction to the possible approaches and an overview of the development of the field, with some milestone works, are presented.

Analogous to one-step and two-step spin coating methods, there are two different approaches to vacuum deposition, namely co-evaporation and sequential deposition. For co-evaporation, all precursor salts are sublimed simultaneously

2. Theoretical background

such that the composite material forms directly on the substrate. For this process, annealing is not always required, or even detrimental [105, 106, 107]. This makes one energy-consuming step redundant, which is advantageous for potential future industrial processes. The sequential deposition approach is comparable to the two-step spin coating method. Here, the metal halide film is deposited first and then covered with the A-cation salts. With this process a multilayer structure is also possible. The layered structure transforms into perovskite by an inevitable annealing step [108]. This shows the versatility of the deposition technique and the applicability for the production of high-quality perovskite solar cells.

In 2013 Liu et al.[7] showed that the co-evaporation process can make highly efficient perovskite solar cells. In this work, methylammonium iodide (MAI) and lead chloride (PbCl_2) were co-evaporated in a molar ratio of 4:1, leading directly to dark brown films and very efficient devices with 15.1% PCE, a record at that time. The perovskite was deposited on compact titanium dioxide (TiO_2) and covered with lithium-doped Spiro-OMeTAD, making this one of the standard configurations over the past years. By further optimisation of the process, Momblona et al.[8] broke the benchmark of 20% PCE in 2016 by using fully evaporated doped organic transport layers. Here, the authors produced the absorber layer comparably to Liu et al.[7] by co-evaporation of PbI_2 and MAI, in a similar ratio. In the years since, many variations of metal halide perovskite have been vacuum processed successfully: methylammonium-free [107, 109], triple-cation [110], pure FAPbI_3 [111], stabilised cubic FAPbI_3 [112] with organic and inorganic transport layers from deposited solution, as well as fully evaporated devices. Another advantage of evaporation-based deposition techniques is the accurate film control and high homogeneity over large areas. This was already shown for module-size devices by Li et al.[9] in 2020 using a co-deposition approach. Here, over 20% for small cells and 18% efficiency for minimodules of 21 cm^2 were achieved. In 2021 Feng et al.[10] demonstrated 400 cm^2 homogeneous films with sequential deposition of PbI_2 , FAI and CsBr and in-vacuum annealing. When used in small devices (0.09 cm^2) in the established TiO_2 , Spiro-OMeTAD architecture, the champion cell showed a PCE of 21.32%, a record for vacuum-deposited perovskite at the moment. These promising results show that the vacuum deposition process has a high potential for the industrial-scale production of highly efficient perovskite solar cells. The main research topics in recent years that have led to these remarkable results are described in the following.

2.6.1. Deposition of the organic cation

One of the biggest challenges in vacuum depositing perovskite is a well-controlled deposition of the organic cation. In the beginning, mainly methylammonium was used as the A-cation in vacuum-deposited perovskites. This material presents some difficulties during vacuum deposition. The small molecule is known for its high vapour pressure and gas-like behaviour in vacuum. Together with a low adhesion coefficient, this complicates the control over the evaporation and led several groups to control the MAI rate via the partial pressure of the material [106, 113, 114, 115].

These problems were addressed by Borchert et al.[116] in 2019, where the evaporation behaviour of MAI from several different suppliers, as well as self-synthesised material, were investigated. The authors found a correlation between phosphorus-containing impurities and the possibility of measuring a rate at the quartz crystal microbalances (QCM). It was found that the presence of impurities increases the detected rate or the adhesion on the gold-covered QCM surface. The difference is clearly observable by comparing Fig. 2.9 a), and b), where an SEM picture of two QCM surfaces with different types of MAI evaporated on top is shown. With new technological developments such as the application of strongly cooled QCMs, the rate detection became more reliable, but other crucial factors were left unaddressed. One of these factors involves the adhesion of the organic cation salt to the substrate. In 2020 Roß et al.[117] found a strong decrease in adhesion of MAI to the substrate with increasing substrate temperature. The authors also found a difference between two commonly used underlying organic substrate layers. In Fig. 2.9c), the observed tooling properties at the investigated temperatures are shown, illustrating the reduced adhesion of the organic salt to a surface with increasing temperature. The influence of substrates will be discussed in more detail in Sec. 2.6.2.

Further insight into the deposition kinetics was obtained in 2020 by Kim et al.[118] via monitoring the deposition rate at different positions in the chamber during MAPbI₃ co-evaporation. The authors found that the monitored deposition rate of the organic cation is very different depending on the presence of lead halide. This observation indicates a chemical vapour deposition component in the co-evaporation of MAPbI₃, which means that the adhesion of MAI to an unreacted lead halide surface is increased by a diffusive component driving the conversion to perovskite. This diffusion is only possible when unreacted lead halide is present. Similar effects were seen by other groups as well, where a partial conversion with a closed shutter was observed [106].

2. Theoretical background

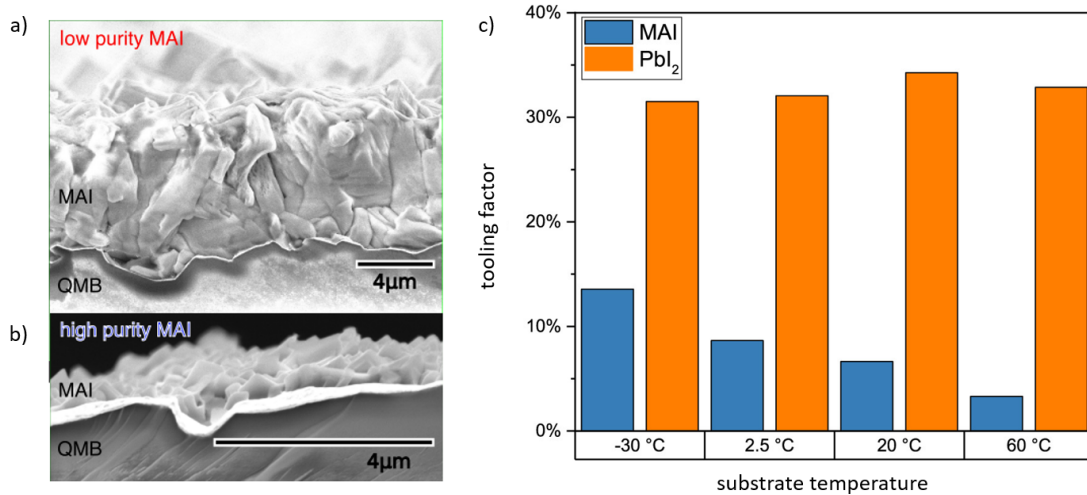


Figure 2.9.: The adhesion of MAI to the substrate: SEM-images of an as-deposited MAI layer on a QCM, a) with impurities, b) without impurities, reproduced from Borchert et al.[111]; c) temperature dependent tooling factor of MAI to a polymeric surface, reproduced from Roß et al.[117]

It can be concluded that a well-controlled deposition of the organic cation is one of the critical factors for a precise perovskite deposition. The properties of the process are influenced by a series of aspects that have consequences on the quality of the final material.

2.6.2. Influence of the substrate material on the crystallisation of vacuum-deposited perovskite

The substrate material significantly affects the crystallisation properties of a vacuum-deposited film. Several studies on this topic showing the impact on a well-controlled deposition are presented in the following.

Abzieher et al.[106] recently published a comprehensive study about the MAPbI₃ growth on various popular organic and inorganic substrate materials. The growth properties were investigated by XRD and SEM, and the polarity of the substrate layers was found to be a critical factor in the growth process. The authors found that non-polar samples induced a columnar growth of the crystallites. In contrast to disordered nucleation on polar substrates, this columnar growth reduces grain boundaries horizontal to the transport layer, which is beneficial for the device's performance. The different growth properties are illustrated in Fig. 2.10. In general, a higher nucleation density was found for vacuum-processed perovskite in comparison to solution-processed layers, lead-

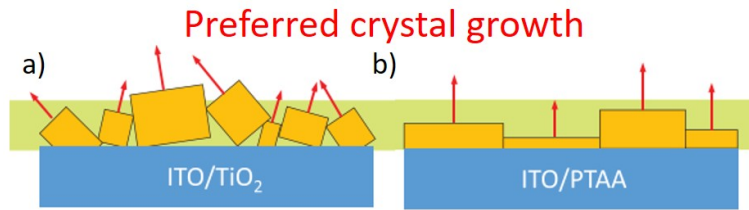


Figure 2.10.: Illustration for growth conditions: a) disordered growth on a polar TiO_2 layer in contrast to b) columnar growth on a non-polar PTAA layer, reproduced from [106]

ing to the often-reported smaller crystallite size [119].

In 2020, Klipfel et al.[120] also found a preferred growth orientation on a TiO_2 substrate layer depending on the evaporation rate. This is found by combining GIWAX, absorption and UPS measurements. An increase in upward-directed crystallites was found for a growth rate of 0.54 \AA/s , which also resulted in an increase in device performance. These findings contradict the study by Abzieher et al.[106], which found no columnar growth on TiO_2 . Furthermore, a change in band gap and Fermi level was observed for the differently oriented films. The Fermi level moved from a p-type to a nearly intrinsic material for well-oriented crystals. Besides the influence of the deposition rate, different types of substrate layers induced a shift in doping level. Here, the transport layers induced a well-centred Fermi level in the band gap of the semiconductor, leading to the best-performing devices. This result emphasises that the growth conditions are crucial for good solar cell devices.

These growth conditions were investigated in detail by Olthof et al.[121] via photoelectron spectroscopy measurements of very thin films during the deposition process. Depending on the substrate material, it was found that the catalytic action of metal oxides impedes the perovskite formation due to an increase in methylammonium degradation. The perovskite growth can only begin after a passivation layer has formed. This $\sim 30 \text{ nm}$ thick interlayer does not form on organic contact layers, where a distinct perovskite feature can be measured after only 3 nm . Furthermore, it was found that the contact layers and interface structure can induce dipoles at the interface, which lead to band bending and a change in the materials' work function, which still can be measured after 200 nm in the case of metal oxide substrate materials.

These findings show that the crystallisation process and resulting material quality are strongly dependent on the substrate layer. The substrate influences the film's crystallographic and energetic properties. It further shows that the

2. Theoretical background

deposition process must be adjusted when the underlying layer material is exchanged.

2.6.3. Influence of substrate temperature on the crystallisation process

One important factor not yet discussed in the crystallisation of perovskite in vacuum is the effect of the substrate temperature. The temperature is known to influence not only the adsorption of the organic molecule, as was found by Roß et al.[117] and discussed here in chapter 2.6.1, but also impacts the crystal formation, as found in recent studies.

In 2020, Lohmann et al.[122] compared cooled and room temperature substrates and a sequence of both. The authors were able to tune the crystallite size of evaporated MAPbI₃ films reducing the substrate temperature. At temperatures of -2 °C, extraordinary large grains in the mm range were found, which is unusual for vacuum-deposited perovskites. Although increased grain size is often associated with improved performance in solution-processed perovskite solar cells, this is not the case for vacuum-deposited perovskite. Besides the change in crystallinity, the samples prepared at room temperature have an excess of lead iodide, which hints at a change in stoichiometry due to the adhesion of MA. Despite the stoichiometry of the film and a reduced crystallinity, the photovoltaic performance was the best for films deposited at room temperature. Similar behaviour was found by Kottokkaran et al.[123], where an elevated substrate temperature was investigated. By adjusting the partial pressure of MAI, the stoichiometry was kept constant, and an increase in crystallite size could be observed for substrate temperatures of 50 °C and 75 °C. Similar to the study of cooled substrates, the photovoltaic performance was best for devices produced at room temperature.

3. Experimental methods

3.1. Physical vapor deposition

Physical vapour deposition, or PVD, is a collective term for several thin film deposition techniques. Typical film thicknesses range from a few nanometers to some micrometres, and an accurate thickness control is desired. The coating is realised by vaporising a solid material in a vacuum and depositing it on the desired surface. The variety of processable materials ranges from metals over compound materials and semiconductors to organic materials and plastics. Depending on the deposition material and the desired film properties, the vaporisation process can vary significantly. Common techniques are sputtering, here the solid material is extracted from the surface by hitting it with ions or plasma and thermal evaporation, where the material is transferred into the gas phase by thermal energy. This can be realised through exposure to thermal radiation, Joule heating in a resistive boat or hitting the material with a guided electron beam or a high current pulsed arc. Also, pulsed lasers can be used to evaporate the material. These techniques have differing properties regarding the material requirements like stability, vapour pressure or electrical conductivity[124].

3.1.1. Theoretical description of thermal evaporation

Several conditions define the evaporation and deposition characteristics of a material and a deposition setup. The process is illustrated in Fig. 3.1. Firstly, the evaporation properties of a material are mainly defined by its vapour pressure and thermal stability. Both are intrinsic material properties. The equilibrium vapour pressure P_{eq} of a material is adjusted by the evaporation temperature T_{source} or the input of thermal energy in the case of an electron beam or arc evaporation. With increasing temperature, more material sublimates and leaves the effusion cell. Besides the temperature, the geometry of the evaporation source and especially the orifice size δA influences the material beam intensity J_w leaving the source. For an ideal effusive cell, the angular distribution approaches the cosine law of emission. The ideality depends on factors like the probability

3. Experimental methods

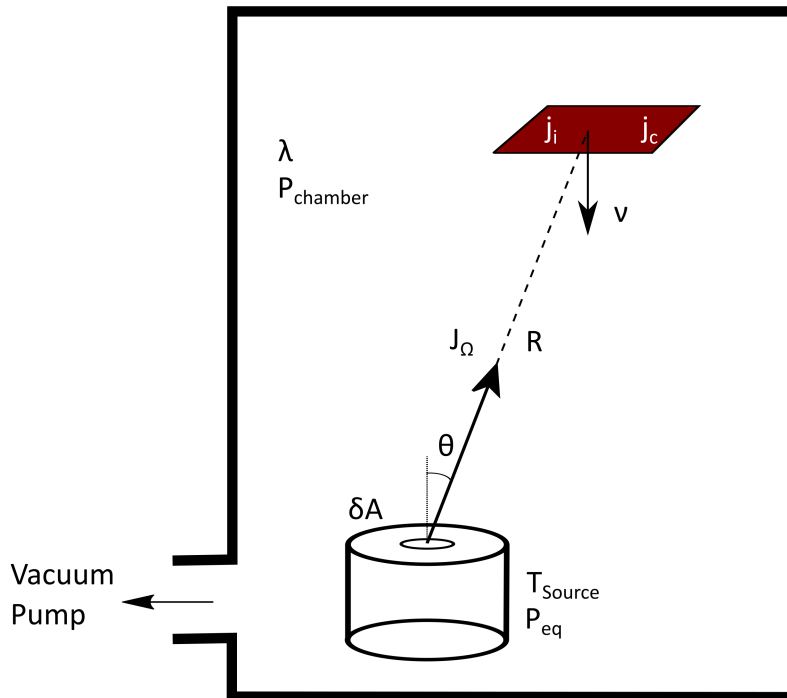


Figure 3.1.: Illustration of the vapor deposition of a thin film, from a Knudsen cell evaporation source.

of collisions of the particles on their path to the substrate. This depends on the background pressure P_{chamber} and is given by the free mean path l of the particle. The incident flux j_i , of particles hitting the substrate further depends on the angle of source and substrate θ , the deposition angle ϕ and the distance R . Together with the condensation coefficient of the material and any possible re-evaporation from the substrate, which is especially significant for heated substrates, the condensation flux j_c is determined. From all these factors, the deposition rate v , which gives the thickening of the film on the substrate, can be calculated. The deposition rate is usually given in \AA per s.

3.1.2. Experimental realisation

For a well-controlled evaporation, several variables have to be considered. As described beforehand, the most essential variable is the source temperature, which is usually controlled by regulating the current through the boat or the filament, and with it, the energy input. Secondly, the vessel pressure defines the equilibrium vapour pressure and with it the amount of material subliming from the source, as well as the mean free path of the evaporated material on

the way to the substrate to reduce scattering. The last process to control is the condensation on the substrate, which can be influenced by surface treatments, adhesion layers and, most important, the substrate temperature. To ensure a uniform deposition, the substrate can be rotated.

The most common way to measure deposition rate is using a quartz crystal microbalance (QCM). Here the quartz micro frequency of a quartz crystal resonator is measured. The frequency is dependent on the mass deposited on the surface of the crystal. For a known material, the deposited thickness change can be measured in sub angstrom accuracy. For an accurate rate measurement at the substrate, the geometrical relation of the QCMs position to the substrate has to be calibrated. This process is called tooling.

3.2. Vacuum deposition of perovskite layers

3.2.1. Vacuum deposition chamber

The materials were deposited in a MiniPerovap deposition chamber from Crea-Phys. The chamber has a water-cooled inner sheath to prevent re-evaporation from the walls and ensures a lower base pressure. It is cooled with a Huber cc-508 cooling system. The cooling agent is held at $-22\text{ }^{\circ}\text{C}$, which results in $\sim 12\text{ }^{\circ}\text{C}$ at the inner surfaces. The chamber is equipped with four LTE-evaporation sources with a designed temperature range of $\sim 100\text{ }^{\circ}\text{C} - 800\text{ }^{\circ}\text{C}$, also from Crea-Phys. The deposition rates of the four sources can be measured individually with QCMs located 8 cm above each of the sources. The rates are read out with a four-channel Inficon SQC-310c rate monitor with a resolution of 0.01 \AA/s . The sources and QCMs are separated with metal blinds attached to the cooled base plate to avoid cross-talk and contamination between the sources. The experiments are controlled and recorded with the software SweepMe!.

3.2.2. Materials

The perovskite precursor materials, formamidinium iodide (FAI), CsBr and PbI_2 were bought from Sigma Aldrich. 3H-Cyclopropa(1,9) (5,6)fulleren-C60-1h-3-butanoic acid-3-phenyl-methylester (PC_{61}BM) (99.5%) was purchased from Solenne BV, and Poly[bis(4-phenyl)(2,4,6-trimethylphenyl)amine] (PTAA) and bathocuproine (BCP) were purchased from Sigma Aldrich and used as received. Pre-patterned ITO coated glass substrates were purchased from Yingkou Shangneng Photoelectric material CO., Ltd. The pre-patterned ITO substrates were ultrasoni-

3. Experimental methods

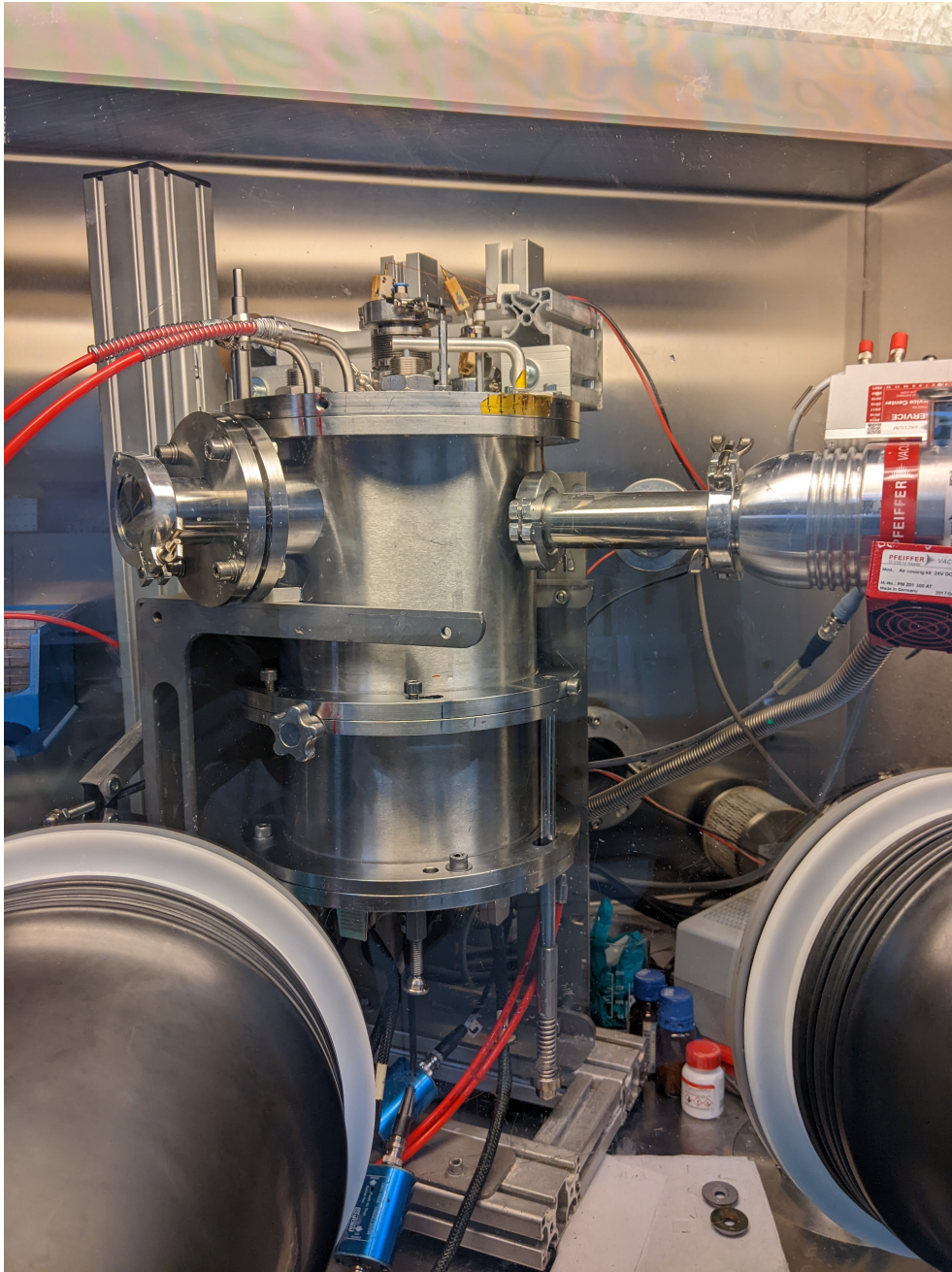


Figure 3.2.: Picture of the vacuum deposition setup

cally cleaned with acetone, ethanol and isopropanol, followed by a 10 min oxygen plasma treatment.

3.2.3. Tooling process

Tooling experiments were performed in the chamber by comparing the signals of two QCMs located at the top of the chamber, one close to the substrate and one close to the crucible. Since the quartz at the height of the substrate is slightly off-centre, the most accurate way to determine the geometrical tooling factor is by measuring the thickness of a deposited layer and comparing it to the signals read out by the QCMs. In the used deposition setup, described in Sec. 3.2.1, the geometrical tooling factor was determined to be 22% of the signal of the QCM at the crucible. The dynamic tooling factors are measured with the top QCM compared to the bottom QCM.

3.2.4. Charge transport layer preparation and device fabrication

The PTAA solution was prepared by dissolving 1.5 mg/ml PTAA in anhydrous toluene and stirring overnight at 70 °C. For the preparation of the hole extraction layer, the freshly cleaned ITO substrates are dynamically spin-coated with 30 µl solution for 30 s at 2000 rpm. After the spin coating, they are annealed at 100 °C for 10 min. The ITO-substrates with the hole extraction layer are stored in inert nitrogen atmosphere before the perovskite deposition. For the electron extraction layer, 20 mg/ml PCBM is dissolved in anhydrous chlorobenzene by stirring the solution for 3 hours at 70 °C. Afterwards, the solution is filtered with a PTFE filter. The thin film is prepared by spin-coating 20 µl for 30 s at 2000 rpm on the perovskite layer. This step is followed by 10 min annealing at 100 °C. The electron extraction layer is followed by the hole blocking material BCP. The solution is prepared by dissolving 0.5 mg/ml BCP in anhydrous isopropanol by stirring it at 70 °C overnight. The thin film is prepared by dynamically spin-coating 40 µl of solution for 30 s at 4000 rpm. No annealing is needed for this film. The device is finished by thermally evaporating 80 nm of silver in a Mantis evaporation system integrated into a glovebox. The initial deposition rate was 0.1 Å/s until 20 nm are reached when it was increased to 1 Å/s. The pixel size is defined by the overlap of the ITO-bottom contact and the silver back contact to 4.5 mm².

3.3. Analytical techniques

3.3.1. UV-Vis spectroscopy

In UV-Vis spectroscopy, the light from a continuously emitting light source over the whole spectrum of interest, in this case, 300-1200 nm, is sent through a monochromator and guided through the sample. The transmitted light is recorded at every wavelength with a photodiode in an integrating sphere. To determine the absorbance of a film, the reflected ratio of the incident light has to be subtracted. This is measured in the same setup by switching the sample position and reversing the reference and measurement beam. If the layer thickness d is known, the absorption coefficient $a(\lambda)$ can be determined by the Beer-Lambert law:

$$A = \log \left(\frac{I_0}{I} \right) = a(\lambda)d \quad (3.1)$$

From the absorbance measurements, the band gap is calculated with a Tauc-plot calculation for a direct band gap semiconductor[125]. In this work, a Shimadzu UV-3100 spectrometer with an integrating sphere was used to measure the UV-Vis absorption spectra.

3.3.2. Photoluminescence measurements

The photoluminescence of the thin-films was measured using an integrating sphere (Ulbricht-sphere). As excitation source a 405 nm laser from Coherent with 50 mW intensity in cw-mode was used. The spot size was determined to roughly 1 mm². The emission spectra were recorded with a QE65 Pro spectrometer from Ocean Optics.

3.3.3. Mass spectrometry

In a quadrupole mass spectrometer, ions are separated by selecting one stable flight trajectory in an oscillating electric field. Two pairs of conductive rods generate the field with an applied radio frequency voltage (RF) and a DC voltage. In a full range scan, the RF amplitude and the DC voltage are scanned, and only ions with the right m/Z -ratio can pass the fields.

The residual gas analysis in the vacuum system was performed with an XT300M quadruple RGA system from Extorr In. (USA). It was directly attached to the vac-

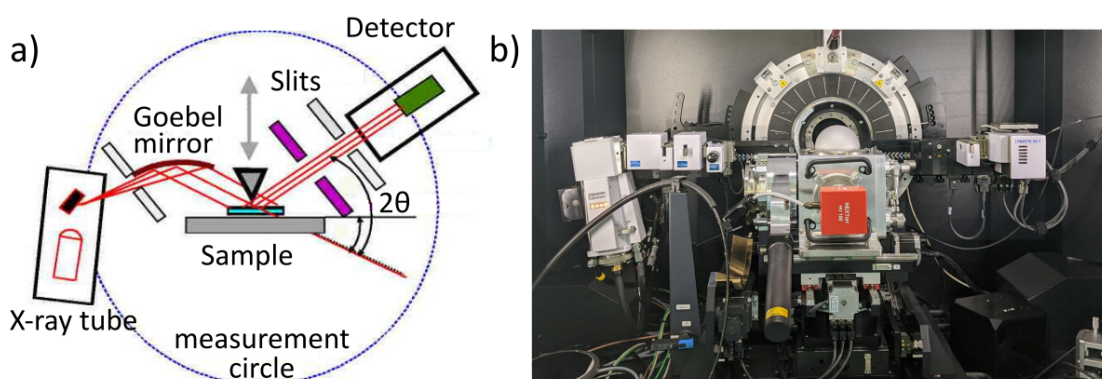


Figure 3.3.: XRD-measurement setup: a) Schematic of the measurement geometry, reproduced from [126], b) picture of the measurement setup, with attached vacuum measurement chamber.

uum chamber, and the full range of $m/Z = 1$ to 300 AMU was scanned three times per minute.

3.3.4. X-ray diffraction (XRD)

X-ray diffraction is used to determine the crystal structure. When Bragg's law 3.2 is fulfilled, X-rays reflected from a crystalline material interfere constructively. This causes intensity maxima, so-called Bragg peaks.

$$n\lambda = 2d\sin(\theta) \quad (3.2)$$

with λ the wavelength of the incident radiation, d the distance between two crystal planes, and θ the diffraction angle. By measuring the diffracted X-ray intensity depending on the diffraction angle, the crystal structure, and information about the orientation can be determined. For the measurements in this work, a Bruker Discover D8 with 1.6 kW Cu- $K_{\alpha 1}$ radiation with a wavelength of 1.54 Å was used. The measurements were performed in parallel-beam geometry in reflection mode. The geometry is depicted in Fig. 3.3. The diffractometer is equipped with a Lynxeye 1D-detector, which was read out in continuous mode with the software DiffracMeasurementCenter. The measurements were background corrected with the software DiffracEva.

3.3.5. GIWAXS

Grazing incidence wide-angle X-ray scattering (GIWAXS) gives insight into the crystal arrangement of thin films, especially the orientation of the crystal planes

3. Experimental methods

is investigated. For GIWAXS measurements, intense, highly-brilliant synchrotron radiation is used. In the case of the measurements displayed here, the X-ray hits the sample under a very shallow angle, 0.1° and 0.3° . These small angles lead to a control of the surface sensitivity since at angles below the critical angle for X-rays, only an evanescent wave penetrates the sample at the surface, and no signal from the bulk is observed. The scattered radiation is detected with a planar detector, which also allows detection of the signals from structures oriented in-plane of the sample surface. This is not possible for XRD measurements, which only probe crystal planes perpendicular to the scattering plane.

The GIWAXS experiments were performed at the European Synchrotron Radiation Facility (ESRF) in Grenoble at beamline ID10, employing a Pilatus 300K area detector. Beam energy was 22 keV, and all experiments were conducted under nitrogen atmosphere.

3.3.6. Scanning electron microscopy (SEM)

Scanning electron microscopy (SEM) is based on the interaction of accelerated electrons and the sample. In the used instrument, electrons are emitted from a field emission gun, subsequently accelerated and then focused on the sample with a system of magnetic lenses. The focus point is about 1 nm in diameter which is then also the resolution limit. The electron beam is scanned over the sample, where it interacts with the to-be-measured sample. By this interaction several characteristic signals are produced: secondary electrons (SE), reflected and elastically backscattered electrons (BSE) and characteristic X-ray emission (EDX). The pictures displayed in this work were taken with an inlens detector. This detector mode measures low-energy secondary electrons emitted from the surface region, which are emitted in a low-angle cone in the direction of the incident beam. A schematic setup is displayed in Fig. 3.4. The scanning electron microscopy images were taken with a Zeiss Gemini SEM 500. The primary electron beam had an energy of 2 keV, and the microscope was operated at a working distance of 2.4 mm, and a magnification of 100.000. The samples were mounted on a standard SEM-sample holder, and a thin layer of gold was sputtered on the sample to prevent electron beam-induced charging. This layer is 2-3 nm thick and does not interfere with the image acquisition. The measurements were taken in high vacuum ($5 \cdot 10^{-6}$ mbar).

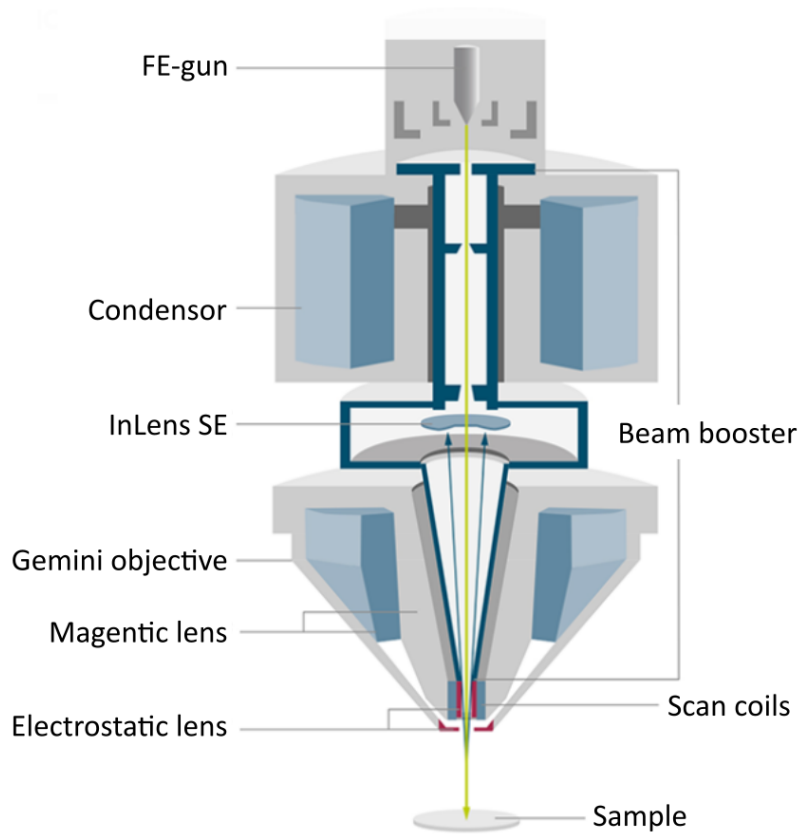


Figure 3.4.: Schematic of an SEM-setup with an InLens SE detector. Taken from [127]

3. Experimental methods

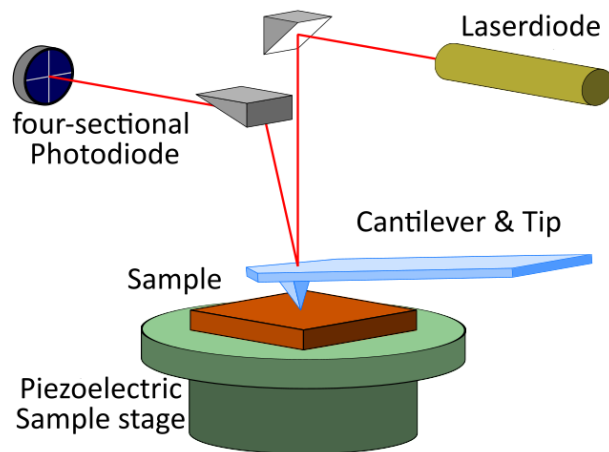


Figure 3.5.: Schematics of a typical AFM configuration, to determine the surface topology of a sample, reproduced from [128]

3.3.7. Atomic force microscopy

Atomic force microscopy is a surface-sensitive measurement technique used to determine surface roughness and layer thicknesses. A cantilever with a very small tip is scanned over the surface. For all measurements, the so-called tapping mode is used. Here, the cantilever tip is vibrated near its resonant frequency and brought into close proximity to the substrate. By the vibration of the cantilever, the tip touches the substrate only very shortly in the periodicity of the resonant frequency, reducing the force on the underlying substrate. This makes it a less invasive measurement procedure than contact mode, where the cantilever is drawn over the substrate. In both cases, the amplitude of the interaction is measured with a deflection-sensitive photodiode. The working principle of an AFM is illustrated in Fig. 3.5.

3.3.8. Profilometer

For the film thickness measurements, a Veeco Dektak 150 is used. The profilometer has a three μm diamond stylus, which is drawn over the sample with a contact force of 3 mg. By tracking the stylus amplitude, a one-dimensional surface profile is measured. The film thickness is determined by either scratching the sample with a razor blade and determining the deepness of the resulting scratch or by removing a stripe of Kapton tape, which was put on the substrate before the deposition and measuring the resulting step.

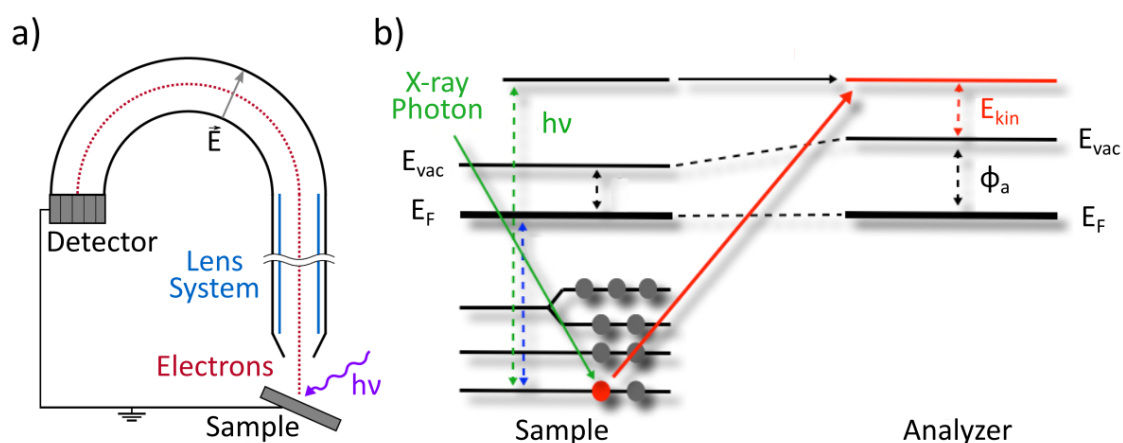


Figure 3.6.: Illustration of XPS-measurement: a) Schematic of the Phoibos 100 setup used for XPS measurements, b) Schematic diagram of the excitation process responsible for with XPS measurable photoelectrons. a) Reproduced from [129] and b) from [130].

3.3.9. X-ray photoelectron spectroscopy (XPS)

XPS probes the core levels of an atom by measuring the collected photoelectrons produced upon X-ray illumination. The measured binding energy is specific for each element and its electronic configuration. By comparing the peak intensities of the measured atomic species taking a correction factor about the atomic sensitivity into account, XPS can determine the chemical composition of a material. Roughly the top 10 nm of material are probed, determined by the inelastic free mean path of the emitted electrons in the material. The photon-electron interaction and the resulting photoelectron are illustrated in Fig. 3.6.

X-ray photoelectron spectroscopy measurements were performed in a custom design UHV system at a base pressure of $6 \cdot 10^{-10}$ mbar using a hemispherical electron energy analyser (Phoibos 100, Specs). For excitation, a non-monochromatic X-ray source was used with an Mg anode ($h\nu = 1252.6$ eV, probing depth=10 nm) at a pass energy of 10 eV and the energy resolution is 800 meV. The XPS peaks were fitted with the XPS Peak Fit 4.1 program.

3.3.10. Solar cell characterisation

Solar cell devices were characterised under standardised testing conditions. An ABET AAA Sun 3000 solar simulator was used as the light source to simulate a 100 mW/cm^2 AM1.5G spectrum. The light intensity was calibrated using a refer-

3. Experimental methods

ence silicon diode (NIST traceable, VLSI) and corrected by the spectral mismatch between the AM1.5G spectrum and the spectral response of the sample. The solar cells were scanned with a Keithley 2450 source measurement unit from 1.2 V to 0 V and back in steps of 0.025 V with a dwell time of 0.1 s.

4. Pressure dependent triple-source co-evaporation of methylammonium-free perovskite

As already discussed in chapters 2.6.1, 2.6.2 and 2.6.3, vacuum deposition is a delicate process, where variations in any number of parameters can strongly influence the outcome. One point that was highlighted during the research of Ji et al.[107] or Gil-Escrig et al.[131] is the necessity for an excess of the organic cation. In previous studies on methylammonium-based perovskites, a ratio in the order of 3 or 4 parts organic cation to one part of B-cation salt was often reported [7, 132]. A similar trend in the ratio of organic to B-cation was observed in the scope of the here-presented study. Since one of the factors observed during the evaporation was a fluctuation in the chamber pressure, and since many groups in the past used this parameter as an adjustment screw for the composition of the thin-film[113, 114], the influence of the background pressure on the co-evaporation of the material is investigated.

Parts of this chapter were taken from our publication "Insights into the evaporation behaviour of FAI: material degradation and consequences for perovskite solar cells", which was created in collaboration with, among others, Seren Dilara Öz and Dr. Selina Olthof (XPS measurements, Universität Köln). Further measurements presented here were performed by Zongbao Zhang (SEM, Technische Universität Dresden), Oleg Konovalov and Maciej Jankowski (GIWAXS experiment, DESY Hamburg), Lena Merten, Dr. Alexander Hinderhofer, and Prof. Dr. Frank Schreiber (GIWAXS analysis, Universität Tübingen).

In this chapter, the vacuum deposition properties of formamidinium iodide for later implementation in a triple source co-evaporation were investigated, using both in-situ mass spectrometry measurements and detailed tracking of the evaporation conditions. With these methods, it was possible to reveal an inevitable decomposition during the evaporation, further highlighting the necessity of pretreatment of as-received material to remove remaining impurities. The decomposition reaction strongly influences the background pressure. This

4. Pressure dependent triple-source co-evaporation of methylammonium-free perovskite

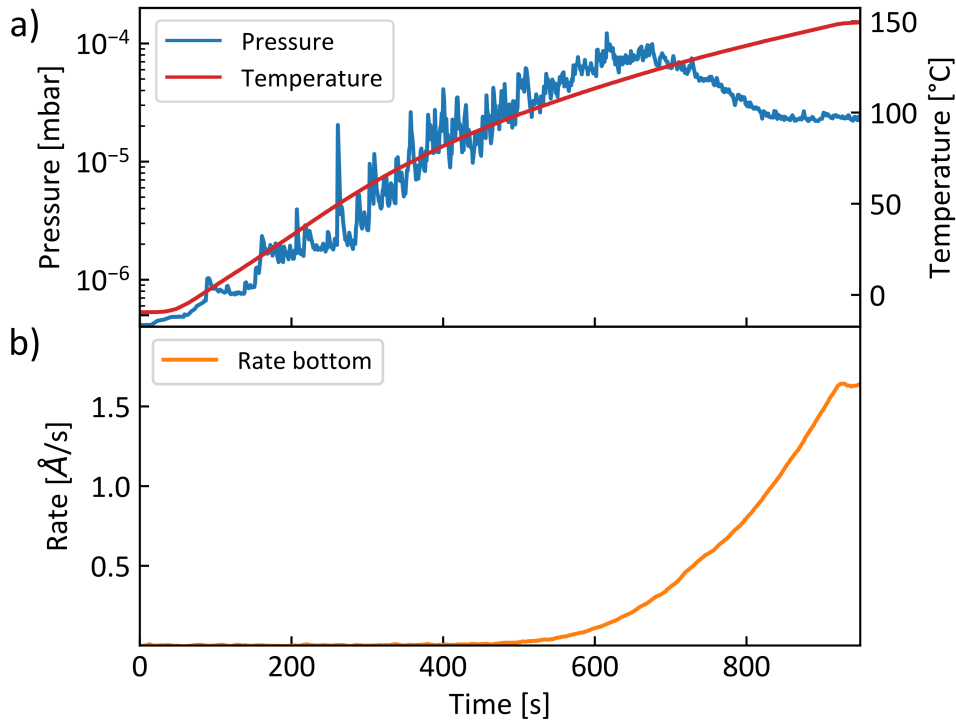


Figure 4.1.: Preheating of fresh FAI: a) chamber pressure and crucible temperature, b) deposition rate at bottom QCM at the crucible.

leads to a detailed investigation of this process parameter on the deposition. Here, the focus is laid on the tooling properties of the organic cation salt.

4.1. Precursor purification

Before investigating the evaporation behaviour of FAI, a close look must be taken at the material itself. Material purity and quality are vital factors for the production of high-quality semiconductors. A sublimation step to rid the material of impurities is usually employed during the synthesis and purification of organic materials when used for semiconductor devices. This purification step is not standard for perovskite precursor materials, leaving the production of thin films prone to unwanted contamination. For the vacuum deposition process, this problem can be ameliorated by an in-situ purification step prior to the deposition to increase the material purity and stabilise the deposition conditions.

To increase batch-to-batch reproducibility, each deposition is started with fresh precursor material. Furthermore all evaporation parameters, like pressure, temperature and deposition rate, are recorded for further analysis. The first step

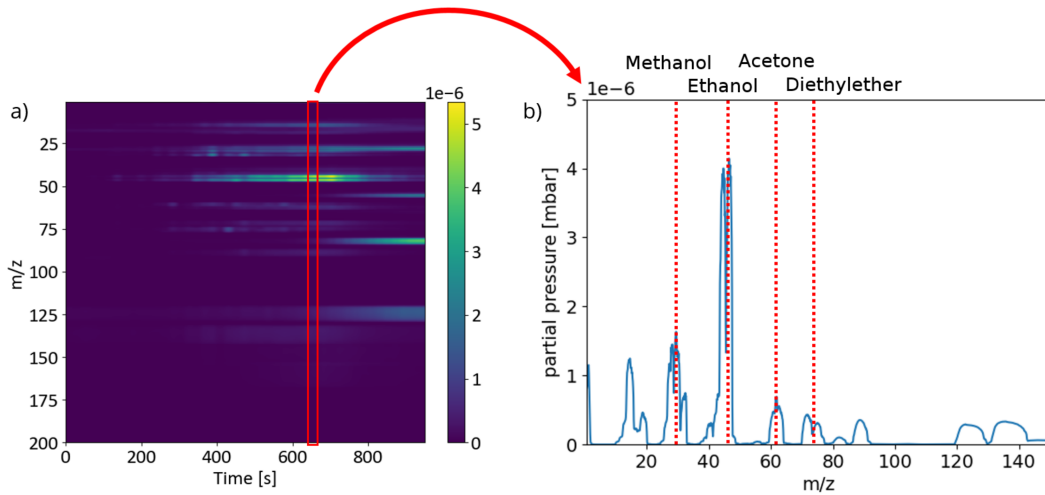


Figure 4.2.: Preheating procedure of fresh FAI: a) illustration of the development of the composition of the background atmosphere during the preheating procedure, b) single mass spectrum at the highest pressure with the probable components highlighted.

| m/Z | Likely molecule | Molecular Formula |
|-----|-----------------|---|
| 18 | Water | H ₂ O |
| 32 | Methanol | CH ₃ OH |
| 46 | Ethanol | C ₂ H ₅ OH |
| 58 | Acetone | C ₃ H ₆ O |
| 74 | Diethyl ether | (C ₂ H ₅) ₂ O |

Table 4.1.: Table of molecules leaving the material during preheating.

involves heating the crucible until the target deposition rate is reached, in this case 1.6 Å/s. During this initial heating of the fresh material, a strong increase in chamber pressure was observed. The development of the chamber pressure and the crucible temperature during the preheating step is depicted in Fig. 4.1 a). The pressure increases from a base pressure $P_{\text{base}} = 5 \cdot 10^{-7}$ mbar to about $1 \cdot 10^{-4}$ mbar at approximately 125 °C. This increase of over two orders of magnitude starts before the detection of a deposition rate (Fig. 4.1 b)). After the initial pressure peak, a decrease is observed when a temperature of approximately 150 °C is reached.

To better understand what underlying causes lead to the appearance of this peak in pressure, the chamber's atmosphere is continuously probed with a mass spectrometer.

In Fig. 4.2 a) both the evolution of the partial pressure of the detected molecules and their m/Z-ratio are plotted over the time of the evaporation procedure.

4. Pressure dependent triple-source co-evaporation of methylammonium-free perovskite

The increase in pressure can be attributed to a variety of materials leaving the precursor during this initial heating. The most dominant signals are those associated with organic solvents, as highlighted in Fig. 4.2 b). The m/Z -ratio of each of the detected solvents is presented in Table 4.1. From the decrease in pressure after the initial heating out, it can be deduced that the material is not dried properly after the synthesis, resulting in residual solvents in the material if used as received from the supplier. FAI from several popular suppliers was tested, and a similar outgassing behaviour was found for all of them. The measurement results are depicted in the Appendix in Fig. A.1. Since most research groups use the precursor materials as received directly from the vendor, it can be assumed that these material impurities are pervasive in perovskite research.

The same preheating procedure was performed before every evaporation of FAI in the following to ensure a reproducible evaporation behaviour.

As already illustrated in Sec. 2.6.1, is the deposition of the organic cation one of the most sensitive process parameters involved during the vacuum deposition of perovskite. For a well-controlled co-evaporation, high accuracy is required in all parts of the deposition since small variations influence the resulting material. Many studies report the necessity of an excess amount of organic cation for the deposition of a stoichiometric film [107, 131, 133]. The same was observed during the preparation of methylammonium-free $\text{FA}_{1-x}\text{Cs}_x\text{Pb}(\text{I}_{3-x}\text{Br}_x)$ mixed halide metal perovskite in preliminary experiments, which led to a deeper investigation of the evaporation behaviour of the organic cation.

4.2. Film deposition procedure

The deposition of thin-films is a delicate process due to the thin layers and various factors influencing the film properties. Especially for perovskites, this has been shown previously, as already discussed in Sec. 2.6.

All films characterised in this section were co-evaporated in a dedicated deposition tool, which is described in the experimental section 3.2.1. The deposition procedure is defined precisely to reduce possible variations and increase reproducibility. Methylammonium-free, $\text{FA}_{(1-x)}\text{Cs}_x\text{Pb}(\text{I}_{(3-x)}\text{Br}_x)$ was chosen as perovskite material. This was co-evaporated from FAI, CsBr and PbI_2 . For every deposition, fresh FAI was used and prepared as described in Sec. 4.1. The inorganic salts were used for several depositions since they do not degrade in the chamber and show reproducible evaporation behaviour. The film composition is controlled by constant tracking of the deposition rates. First, the CsBr rate is

set between 0.09 - 0.1 Å/s. Due to noise in the sensing electronics, a more accurate control is not possible. The CsBr rate is reached at approximately 400 °C and 50% source power. Then the rate of PbI₂ was set to 0.6 Å/s, and stabilised via a power control of the PID-module implemented in SweepMe!, which tracks and controls the evaporation parameter. This rate is reached at around 290 °C and 38.5% of the output power. Lastly, a rate of 1.6 Å/s is achieved in the same way for FAI as for PbI₂, but at 125 °C and 29% power. To ensure steady heating of the material and keep the degradation as low as possible during the heating procedure, the source power is limited to 40%. The molar ratio of the deposited precursors adds up to 1.6:0.25:1 for FAI:CsBr:PbI₂, which means that an excess of 85% of A-cation salt has to be deposited to form the perovskite layer. Throughout the deposition process, the substrate holder is kept at room temperature to ensure constant crystallisation properties.

4.3. Crystallographic characterisation

The microstructure and composition of a perovskite thin-film influence its properties in various ways, the most important being their stability [134] and performance [135]. The influence of different background pressures on the crystallinity and morphology of the co-evaporated perovskite thin-films was characterised by XRD, GIWAXS and SEM, and is described in the following section.

4.3.1. XRD

The X-ray diffraction measurements, shown in Fig. 4.3, confirm the perovskite structure of the as-deposited films. The dominant peaks at $q = 1.00 \text{ \AA}^{-1}$ and $q = 2.00 \text{ \AA}^{-1}$, correspond to the (100) and (200) crystal planes of the pseudo-cubic α -phase of FA-based perovskite systems. Only a small contribution of the non-photoactive hexagonal δ -phase can be found. This crystal phase is indicated by a δ in Fig. 4.3. The small peak observed at $q = 0.70 \text{ \AA}^{-1}$ corresponds to the δ -phase of CsPbI₃ and the small shoulder at $q = 0.83 \text{ \AA}^{-1}$ to the one of FAPbI₃. Furthermore, an excess of PbI₂ is seen for all films, indicated by the characteristic reflection at $q = 0.89 \text{ \AA}^{-1}$, marked with an asterisk. The PbI₂ excess rises with increasing background pressure, indicating a change in the material composition. Since the deposition ratio of A-cation salts to B-cation salt is approximately 2:1, no PbI₂ excess should be expected. However, previous studies have shown that a small lead iodide excess can passivate surface defects, benefitting the

4. Pressure dependent triple-source co-evaporation of methylammonium-free perovskite

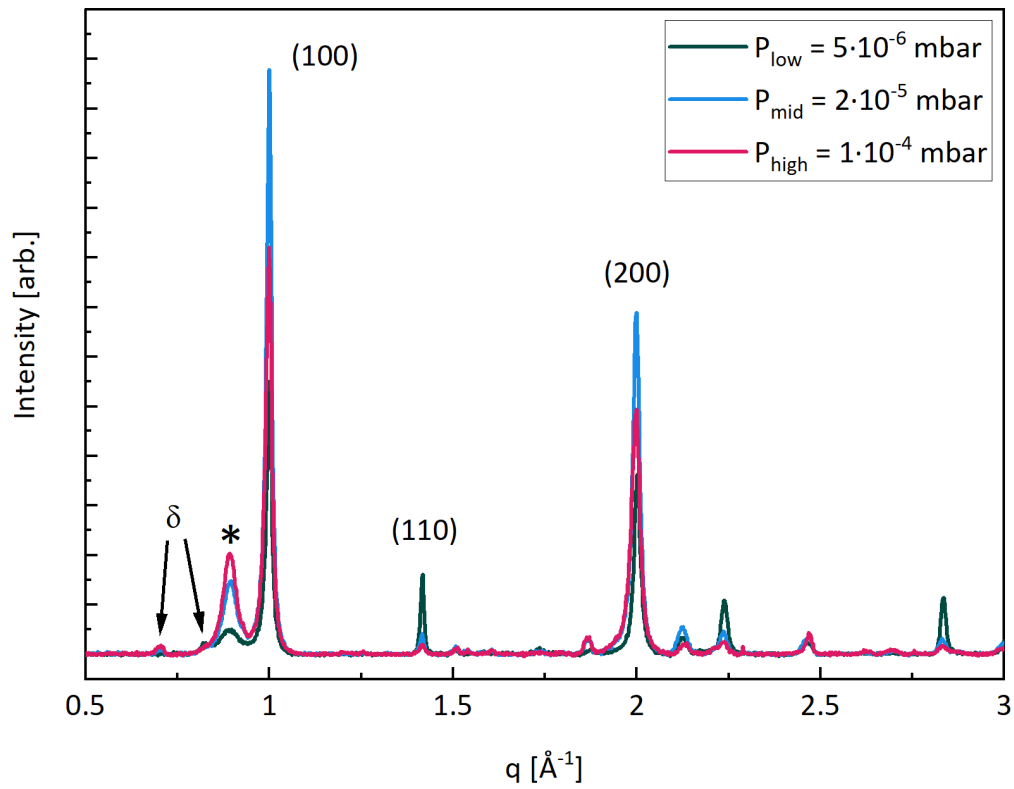


Figure 4.3.: X-ray diffractogram of as-deposited $\text{FA}_{1-x}\text{Cs}_x\text{PbI}_{3-x}\text{Br}_x$: a) at low pressure $5 \cdot 10^{-6}$ mbar, b) at medium pressure $2 \cdot 10^{-5}$ mbar, c) at high pressure $1 \cdot 10^{-4}$ mbar, the signal of PbI_2 at 0.89 \AA^{-1} is marked with an asterisk, the corresponding lattice planes of the perovskite diffraction signal are labeled. The signals corresponding to the hexagonal crystal phases are labeled with a "δ".

| Pressure | Peak position (100) | FWHM (100) | Peak Ratio (100)/(110) |
|------------------------|---------------------|------------|------------------------|
| $5 \cdot 10^{-6}$ mbar | 1.000 | 0.0194 | 3.26 |
| $2 \cdot 10^{-5}$ mbar | 0.999 | 0.0181 | 29.30 |
| $1 \cdot 10^{-4}$ mbar | 0.998 | 0.0215 | 42.73 |

Table 4.2.: Analysis of the peak fits from Fig. 4.3

performance of perovskite-based photovoltaic devices [136].

By analysis of the XRD pattern, further insight into the crystallinity and crystallite orientation can be gained. The peaks were fitted with a Gaussian, and the extracted parameters are displayed in table 4.2. From the peak position of the (100) reflection, the lattice spacing of the pseudo-cubic crystal structure can be calculated via the Bragg condition to 6.29 \AA , which corresponds well to a perovskite composition of approximately $\text{FA}_{0.7}\text{Cs}_{0.3}\text{PbI}_{2.7}\text{Br}_{0.3}$ [137]. The difference in the peak positions between the as-deposited films is very small, so the assumption that the lattice constant increases at elevated pressures cannot be made. The margin of error of the peak fits and the measurement is higher than the difference in the peak position. The crystallite size of a polycrystalline thin-film is related to the peaks' full width at half maximum (FWHM). A narrower FWHM corresponds to larger crystallites. From the peak analysis, no clear trend for a change in crystallite size to the pressure during the deposition of the thin-films can be deduced. Additionally, the height of the peaks corresponding to the (100) and (110) lattice planes are compared. The higher contribution of the (110)-reflection of the film, prepared at low pressure, indicates a different orientation of the crystallite growth compared to the other two samples. The orientation of the crystallites is further confirmed via GIWAXS measurements, as presented in the following section.

4.3.2. GIWAXS

The GIWAXS measurements presented in the following section were performed by Oleg Konovalov and Maciej Jankowski (ESRF). The data was analysed and prepared by Lena Merten (AG Schreiber, Universität Tübingen).

From the analysis of the GIWAXS measurements performed on as-deposited films and those annealed at $100 \text{ }^\circ\text{C}$ for 10 min, a change in orientation with the deposition pressure can be observed. At low pressures, the crystallites have a slightly preferred orientation with the (100)-lattice plane parallel to the substrate, as illustrated in Fig. 4.5 a). This is indicated by a higher proportion of the angular maxima marked in blue in Fig. 4.4 a), c) and d). Annealing the sample

4. Pressure dependent triple-source co-evaporation of methylammonium-free perovskite

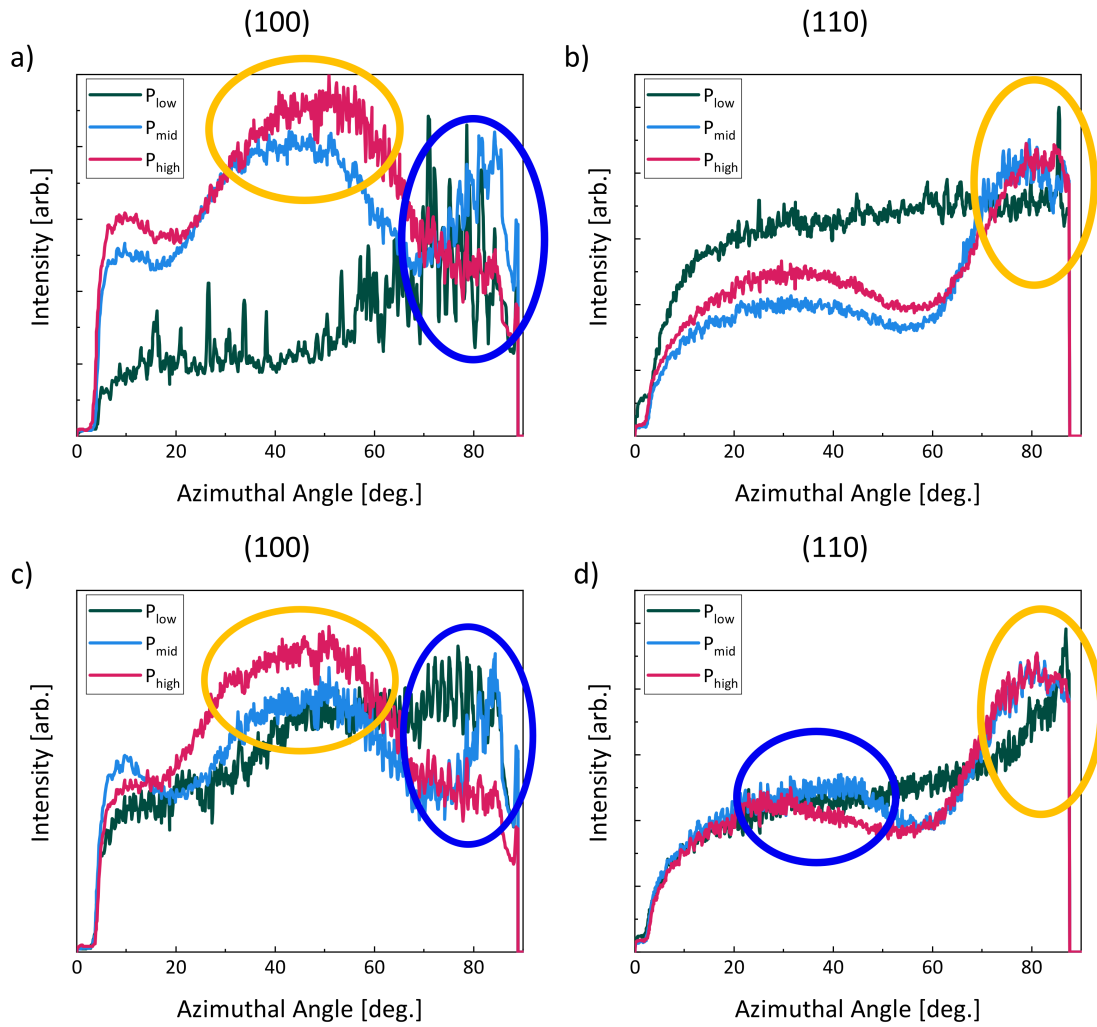


Figure 4.4.: The angular profile of the 1.00 \AA^{-1} reflection corresponding to the (100)-lattice plane and the 1.40 \AA^{-1} corresponding to the (110)-lattice plane of an unannealed perovskite film a) and b). For an annealed film c) and d). The data is extracted from the reciprocal space maps shown in Fig. A.3 in the appendix. GIWAXS measurement analysed by Lena Merten.

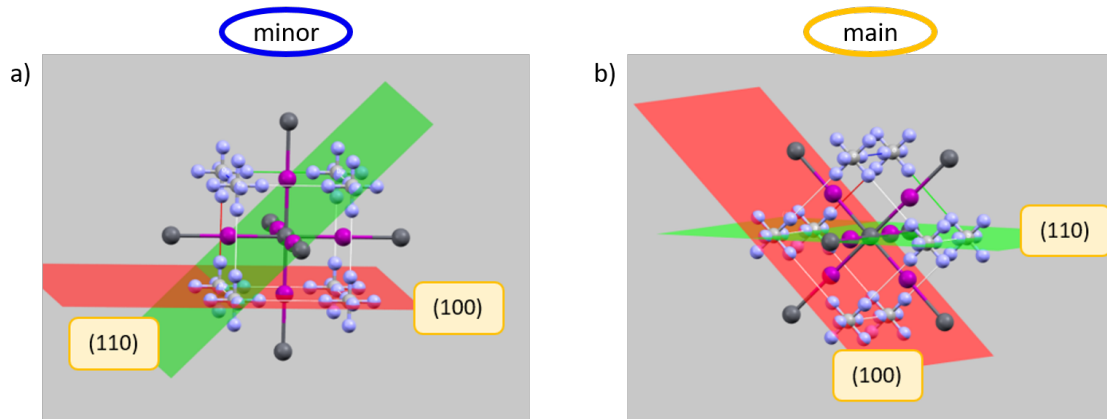


Figure 4.5.: Schematics of the minor (blue) and main (orange) perovskite crystallite orientation observed in the GIWAXS measurements.

evaporated at low pressure seems to make the crystal orientation more similar to the high-pressure samples. In the annealed low-pressure films, the (110)-plane tends to grow in parallel to the substrate, as illustrated in Fig. 4.5 b). This is indicated by a higher proportion of the peaks highlighted in orange. Annealing does not have much influence on the crystal orientation of samples deposited at higher pressure. The difference in orientation of the as-deposited material shows the influence of the background pressure on the crystallisation process of the co-evaporated material. In other studies, crystal growth in the here minor orientation has shown beneficial effects on the photovoltaic performance of the thin-film [106].

4.3.3. Scanning electron microscopy

To get more insight into the microstructure of the deposited thin-films, the crystal morphology of the samples evaporated at three different pressure levels is investigated by SEM. The images are displayed in Fig. 4.6.

The pictures at all pressure levels show small crystallites, with grain sizes smaller than 100 nm. This grain size is typical for vacuum-deposited perovskites and has been observed in other studies as well [117, 110]. Due to the diminutive grain size, microscopic structures such as terraces were not observed. Therefore further information on crystal orientation could not be gleaned from this measurement, and XRD measurements cannot be validated by this method. Furthermore, no excess PbI_2 crystals on the surface can be seen, which would be indicated by bright hexagonal or needle-like crystals [138]. This leads to the conclusion that the excess of PbI_2 detected by XRD is well distributed through the

4. Pressure dependent triple-source co-evaporation of methylammonium-free perovskite

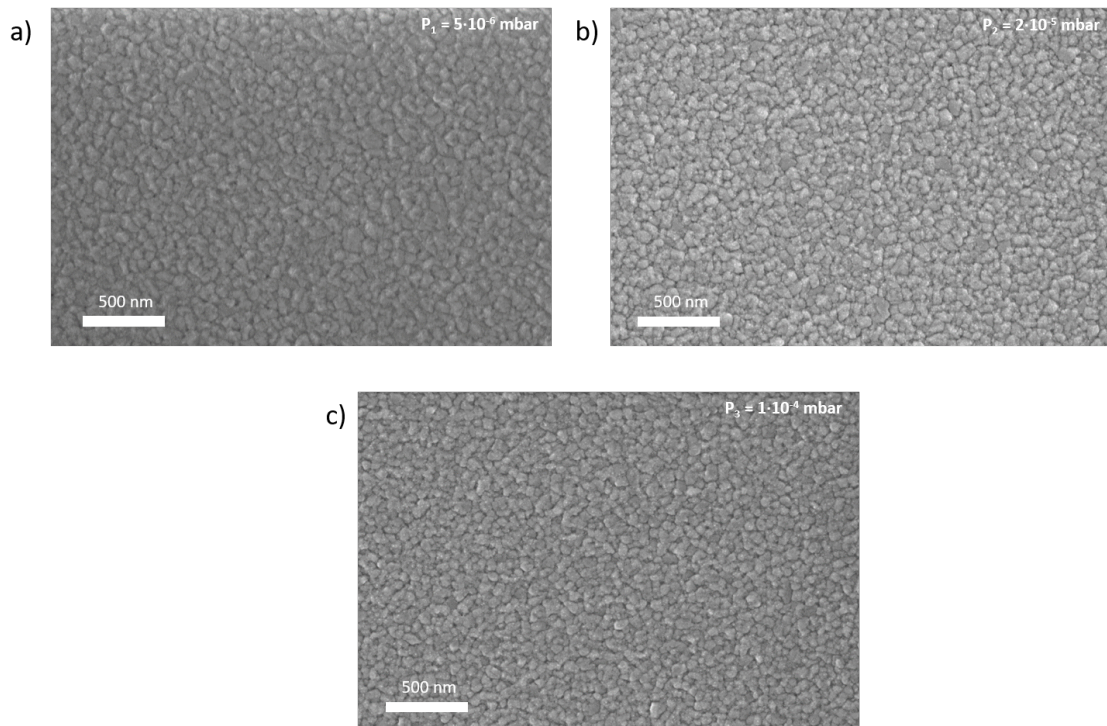


Figure 4.6.: SEM-pictures of as-deposited $\text{FA}_{1-x}\text{Cs}_x\text{PbI}_{3-x}\text{Br}_x$, a) at low pressure = $5 \cdot 10^{-6}$ mbar, b) at medium pressure = $2 \cdot 10^{-5}$ mbar, c) at high pressure = $1 \cdot 10^{-4}$ mbar. The measurements were performed by Zongbao Zhang at DCN Dresden.

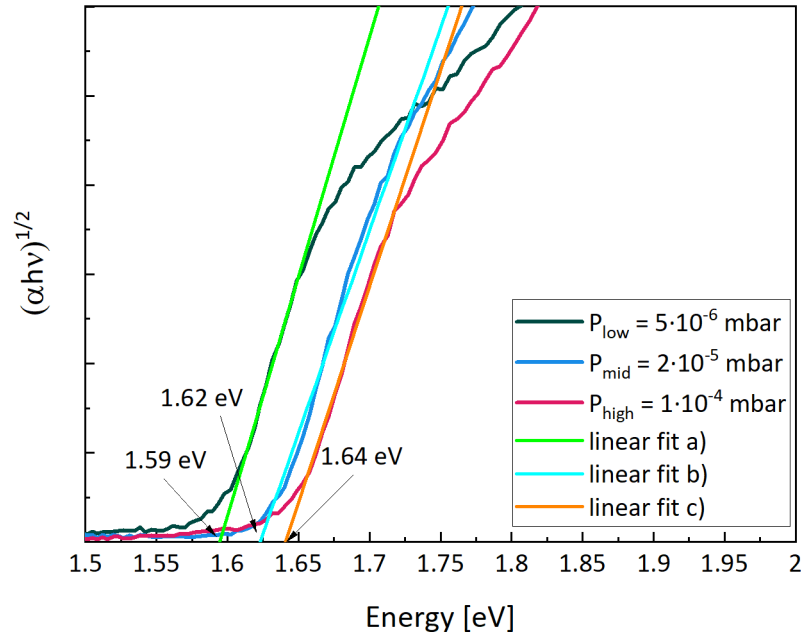


Figure 4.7.: Tauc plot from absorption measurements for perovskite films deposited at different pressures

whole layer. This will be discussed in more detail in Sec. 5.4.3. All films are very homogeneous and pinhole-free with no surface flaws.

4.4. Optical characterisation

The increased PbI_2 excess observed in the X-ray scattering experiment hints toward a lack of incorporation of the organic A-cation salt into the film at elevated pressures. Although this change in the stoichiometry of the thin-film was not resolvable in XRD measurements, it has to be visible in optical measurements. The composition of $\text{FA}_{1-x}\text{Cs}_x\text{PbI}_{3-x}\text{Br}_x$ was checked by determining the optical band gap from absorption measurements via the Tauc method, and photoluminescence measurements were performed to confirm the result.

A band gap of approximately 1.6 eV can be determined for the different perovskite compositions. By comparing this to the results of a comprehensive study of solution-processed perovskite by Bush et al.[139] a value of $x = 0.25$ can be deduced for the $\text{FA}_{1-x}\text{Cs}_x\text{PbI}_{3-x}\text{Br}_x$ composition. This result is also in good agreement with the results of Chiang et al.[140], who worked on a comparable perovskite composition. For the perovskite deposited at different pressure levels, a

4. Pressure dependent triple-source co-evaporation of methylammonium-free perovskite

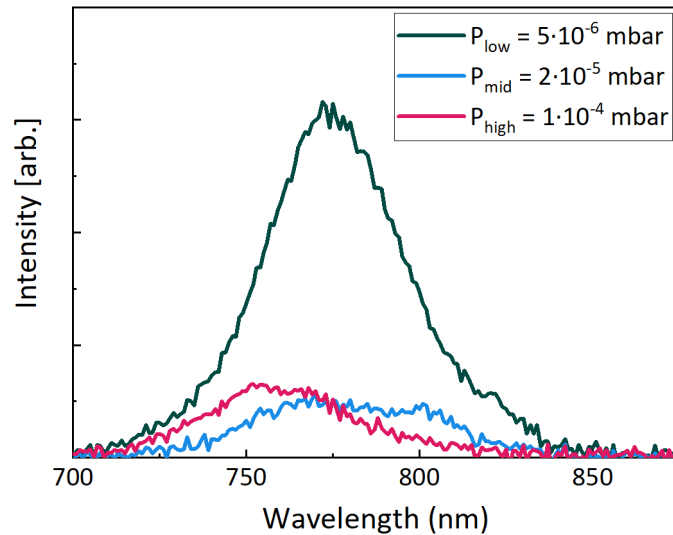


Figure 4.8.: Photoluminescence spectra of $\text{FA}_{1-x}\text{Cs}_x\text{PbI}_{3-x}\text{Br}_x$ -films deposited at varying pressures. The films were excited with a 405 nm laser in cw-mode and measured inside an integrating sphere.

band gap shift of 0.05 eV, from 1.59 eV to 1.64 eV, can be deduced from the absorption measurement. This band gap shift can be related to a lower amount of FAI incorporated in the film, which implies a composition 10% richer in bromine for the samples prepared at elevated pressure compared to the ones at low pressure.

The samples prepared at increased background pressures show a decrease in PL intensity, the corresponding measurements being displayed in Fig. 4.8. This decrease suggests a lower perovskite quality[67]. Furthermore, the blue shift of the emission peak further verifies the band gap shift of the deposited layer. For the layers deposited at elevated pressures, the photoluminescence spectrum shows a slight double peak. This could hint toward a light-induced demixing into iodine-rich and bromine-rich regions of the thin-film, which results in crystallites with different emission spectra. Due to the low intensity and low quality of the photoluminescent signal, no reasonable fit of the double peak feature was possible and the result can only be described qualitatively.

4.5. Incorporation of FAI into thin-films

To gain more insight into the incorporation of FAI into co-evaporated perovskite thin-films, dual-source co-evaporated FAPbI_3 films were characterised with XPS.

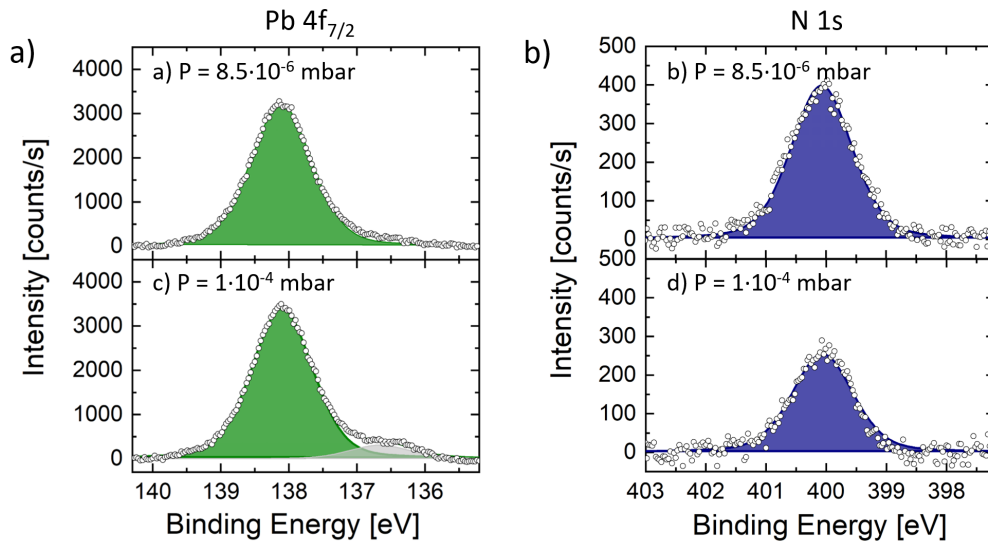


Figure 4.9.: XPS measurement results for the core levels of Pb4f_{7/2} and N1s for FAPbI₃ deposited at low pressure a) and b), and elevated pressure c) and d). The XPS measurements were performed by Seren Dilara Öz

The films were deposited and measured by Seren Dilara Öz in a different preparation setup attached to an XPS system. The deposition ratio in this system was optimised beforehand, and a rate ratio of 3.5:1 for FAI:PbI₂ was found to be optimal for good FAPbI₃ films. The measurements are displayed in Fig. 4.9. The different ratio requirements between evaporation setups highlight that results and recipes are not transferable between deposition setups. The stoichiometry is measured by comparing the peak intensity of the core signals of lead and nitrogen, corresponding to FA. While the Pb signal remains unchanged, the N signal decreases significantly. This leads to the conclusion that only 2/3 of the FAI reaches the sample at elevated pressures. This result is in good agreement with the optical analysis of co-evaporated FA_{1-x}Cs_xPbI_{3-x}Br_x-films, as discussed beforehand.

4.6. Photovoltaic devices

The films prepared at varying pressures were tested in photovoltaic devices to investigate the influence of the crystallisation process on the photovoltaic performance.

The devices are prepared in a well-established p-i-n architecture for high-efficiency devices [27, 141]. The front contact is made of ITO, which is then covered

4. Pressure dependent triple-source co-evaporation of methylammonium-free perovskite

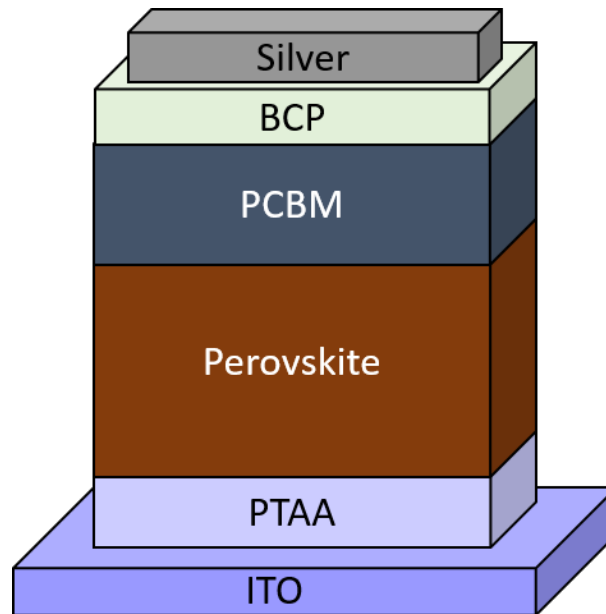


Figure 4.10.: Solar cell stack of the devices prepared in p-i-n architecture.

with 5 nm of the polymeric hole extraction material PTAA by spin coating. After the deposition of the 450 nm thick perovskite layer, the cell is finished with a 20 nm-thick layer of PC₆₁BM with a 8 nm hole blocking layer made from BCP on top. Both layers are also spin-coated from solution. The device is finished with 80 nm of silver as a back contact. The metal is vacuum deposited in a designated evaporation system. More details about the device fabrication process can be found in Sec. 3.2 in the experimental section. The architecture is shown in Fig. 4.10.

4.6.1. Pressure adjustments

As described in Sec. 5.4.2, the material reaching the substrate from the source decreases with higher pressures. The film thickness of the as-deposited films decreases by roughly 25% when the background pressure is increased from $5 \cdot 10^{-6}$ mbar to $1 \cdot 10^{-4}$ mbar. Profilometer measurements illustrate the thickness decrease in Fig. 4.11. The deposition time is adjusted for a reproducible layer thickness to compare the film quality and exclude thickness variations.

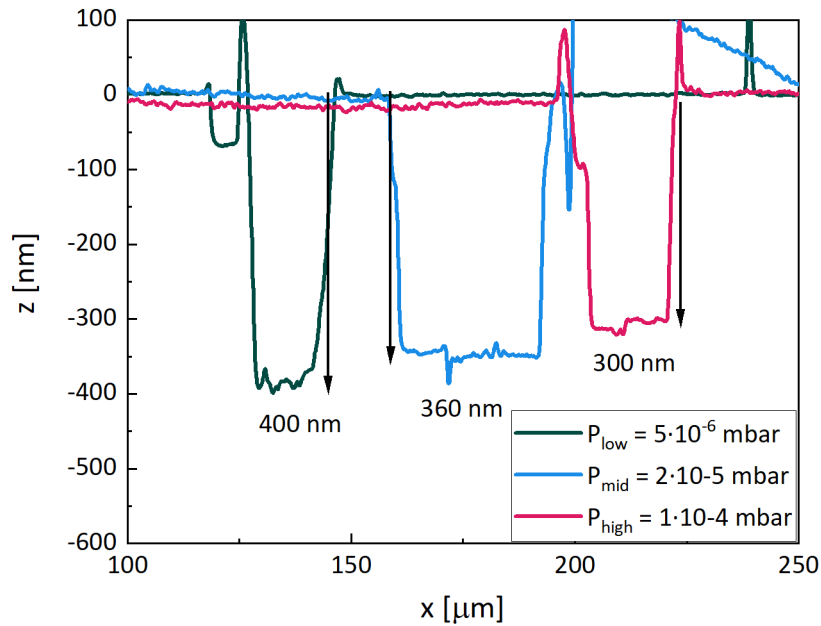


Figure 4.11.: Thickness measurements of $\text{FA}_{1-x}\text{Cs}_x\text{PbI}_{3-x}\text{Br}_x$ -films deposited at pressures from $5 \cdot 10^{-6}$ mbar to $1 \cdot 10^{-4}$ mbar.

4.6.2. Photovoltaic performance

The performance of the described solar cells are measured according to the procedure described in Sec. 3.3.10.

The different batches are displayed together in Fig. 4.12a), b), and c). The other photovoltaic parameters open-circuit voltage (V_{OC}), short current density (j_{SC}), and fill factor (FF) are displayed in the Appendix A.2. Each batch with one sequence of deposition pressures was prepared with simultaneously prepared substrates and transport layers and finished with the back contact in a single metal evaporation. Between each processing step, the devices were stored in the dark under inert nitrogen-filled glovebox atmosphere to reduce degradation by any possible environmental influences. The perovskite depositions were performed consecutively in the same chamber.

The different pressures, at which the samples were prepared, influence the photovoltaic performance of the solar cell devices. Although the process parameters, like substrate temperature, deposition rates, and of course background pressure were kept as constant as possible, the variation from batch to batch is significant. With all pressure configurations, champion devices with close to and over 15% efficiency were produced. In general, the highest pressure

4. Pressure dependent triple-source co-evaporation of methylammonium-free perovskite

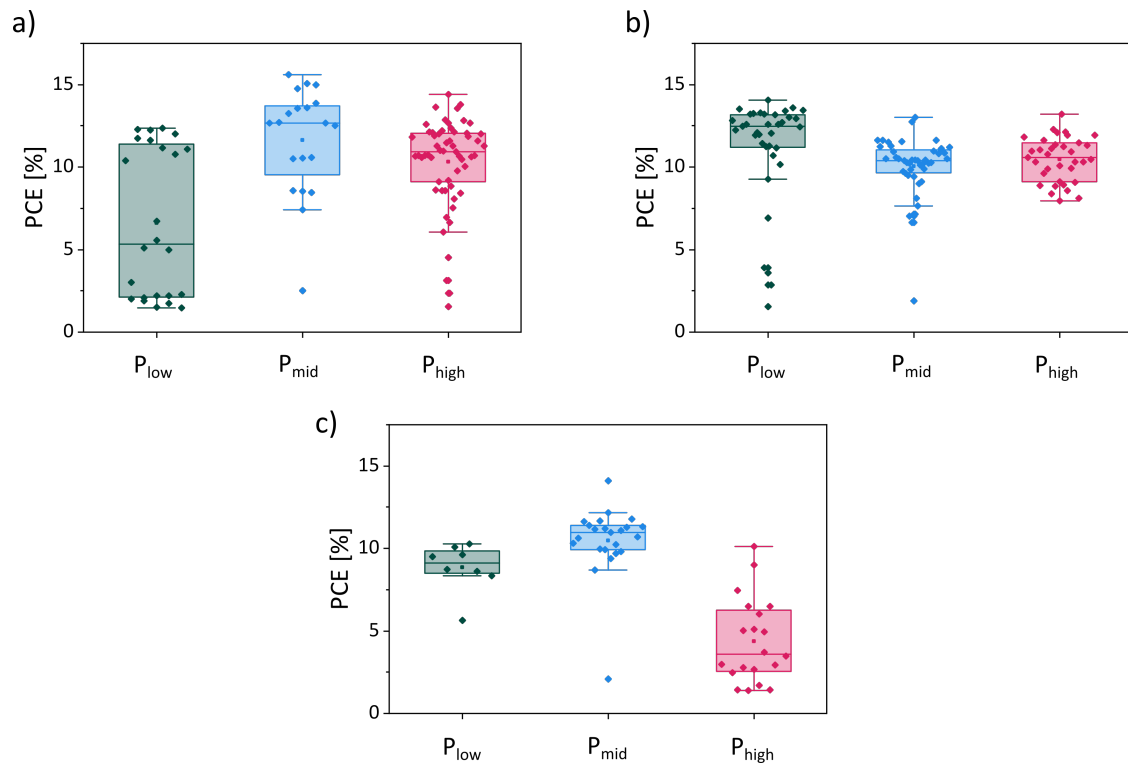


Figure 4.12.: Photo conversion efficiency of consecutive runs of solar cell devices. The devices presented in a), b), and c) were each prepared in consecutive weeks. The open-circuit voltage (V_{OC}), short current density (j_{SC}), and fill factor (FF) are displayed in the Appendix A.2. Non-functional devices were excluded. $P_{low}=5 \cdot 10^{-6}$ mbar, $P_{mid}=2 \cdot 10^{-5}$ mbar, $P_{high}=1 \cdot 10^{-4}$ mbar.

$P_{\text{high}}=1 \cdot 10^{-4}$ mbar showed slightly worse results than samples produced at lower pressures. However, no definitive conclusion about the ideal background atmosphere can be drawn from these experiments. Overall, the results underline the capriciousness of the vacuum deposition process of perovskites.

4.7. Summary

The experiments described in this chapter illustrate the importance of deposition pressure in the evaporation of perovskites. Pressure variations induce changes in the crystal growth orientation. Even more significant is the change in stoichiometry, which is induced by the lower incorporation of the organic cation salt. The FAI deposition is obviously impacted more strongly by the background atmosphere than the inorganic salts. With XPS measurements, a reduction of approximately 30% of the compound was found at elevated pressures as compared to baseline pressure. The reduction is detectable even at pressure variations that are considered normal working pressures, as evidenced by the shift in band gap when increasing the pressure from $5 \cdot 10^{-6}$ mbar to $2 \cdot 10^{-5}$ mbar.

The base pressure is a parameter that is highly dependent on several factors. These include the type of vacuum system used for the deposition, cross-contamination between different source materials, and systemic defects such as leakage. This becomes evident when comparing the recipes and evaporation properties between different deposition setups. The differences in source geometry and background pressure lead to a drastic change in the required excess of the organic cation salt. In the tested setups, a change from 1.85:1 to 3.5:1 was observed. This doubling of the material excess underlies the differences from setup to setup.

By comparing preliminary experiments during the optimisation process, it became evident that the deposition properties of the organic cation salt tend to fluctuate and are the likely reason for the high variation in the results. This inconsistency of results leads this study towards a more specific investigation of the properties of evaporated formamidinium iodide, as presented in the next chapter.

5. Evaporation properties of formamidinium iodide

As made evident in the previous chapter, the evaporation behaviour of the organic salt component is a crucial process parameter for stable and reproducible perovskite co-evaporation. In the following, the evaporation properties of formamidinium iodide and its impact on film formation are investigated.

5.1. Degradation reactions of formamidinium iodide

One of the main problems facing perovskite-based device development is the instability of the organic cation [142, 143]. The degradation of perovskite has been subject to several studies, for example, by thermal degradation with in-situ electron microscopy measurements [144] and in-situ X-ray crystallography [145]. Exposure to high temperatures has been noted to have a detrimental effect. It was also found that humidity [146] and oxygen [147] are reasons for degradation in perovskite thin-films. The thermal instability of methylammonium iodide leads to decomposition into ammonia, and methyl iodide [148], which both have a boiling point under or close to room temperature [149]. These observations led the research community to move away from methylammonium iodide as an A-cation salt, using the more-stable FAI instead [150]. FAI also degrades, as it was investigated by Perez et al.[151] in 2019, but at higher temperatures than MAI. Known degradation routes of formamidinium iodide are depicted in Fig. 5.1. The first step of this degradation involves the deprotonation of FAI, resulting in the formation of formamidine and hydrogen iodide. This reaction is an equilibrium reaction that is used in reverse during the synthesis of FAI and is shifted towards the formamidine and hydrogen iodide with higher temperatures, Fig. 5.1a). The so accruing formamidine can react further by the separation of an ammonia molecule to form hydrogen cyanide, Fig. 5.1b). This is also an equilibrium reaction, influenced by increasing temperature. Lastly, three formamidine molecules can form the circular sym-triazine under the separation of three ammonia molecules in an irreversible reaction.

5. Evaporation properties of formamidinium iodide

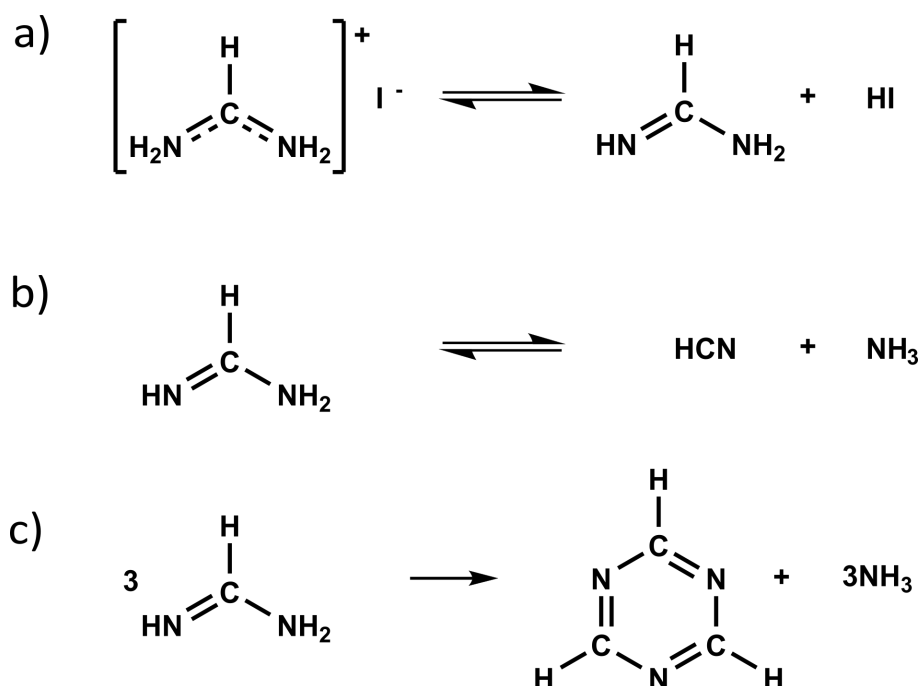


Figure 5.1.: Degradation reactions of formamidinium iodide: a) deprotonation of FAI to formamide and hydrogen iodide, b) degradation of formamide to hydrogen cyanide and ammonia, c) formation of formamide to sym-triazine with ammonia separation

Although formamide and sym-triazine are solids at room temperature, their low vapour pressure leads to their sublimation in high vacuum. All other degradation products are gaseous at room temperature. This was tested by putting pure sym-triazine in a vacuum chamber, where a pressure of $\sim 10^{-2}$ mbar was retained for several hours, which resulted in a complete sublimation of the material. Due to the high background pressure, this could not be measured with the mass spectrometer.

5.2. Evaporation behaviour of formamidinium iodide

Throughout subsequent depositions of perovskite by triple source co-evaporation, issues with replicating the results were noted. Upon closer investigation, the source of these variations was found to stem mainly from the organic cation salt. To determine the deposition behaviour of the salt for a future transition to large scale depositions for industrial-scale production, the organic salt was investigated thoroughly by tracking all deposition parameters and in-situ mass spectrometry measurements.

After the formamidinium iodide was prepared as described in Sec. 4.1, 300 mg of FAI is placed into the crucible, which is then heated constantly at 40% of the maximum power. The evaporation behaviour is investigated by combining in-situ mass spectrometry of the chamber atmosphere, tracking pressure, temperature, and deposition rate at two quartz microbalances, one close to the crucible and one close to the substrate.

The evaporation behaviour can be separated into four distinct regimes. In the first regime (I), the crucible temperature goes from room temperature to about 50 °C. Here we observe a slow increase in pressure from the base pressure of $5 \cdot 10^{-7}$ mbar to $1 \cdot 10^{-6}$ mbar. Notably, no substantial pressure increase like the one observed in the preheating step can be detected, which indicates that the material was successfully purified. The first increase in pressure can be explained by the evaporation of a small amount of adsorbed water condensed on the source's cooled surfaces and close surroundings.

In the second regime (II), in which the source's temperature increases from 50 °C to ~ 120 °C, the partial pressure related to triazine and cyanide starts to increase. This indicates that this temperature range is sufficiently high to initialise the degradation reactions of formamidine to cyanide (Fig. 5.1b)) and triazine (Fig. 5.1c)). It is important to note that in this regime, no rate is yet detected by the QCM so no increase in formamidine partial pressure is recorded (Fig. 5.2 b,c). The signal of I+/HI increases gradually in the meantime, indicating that the reactions occur in solid-state and that the resulting degradation products sublime in vacuum. In this regime, the pressure stabilises at approximately $2 \cdot 10^{-6}$ mbar.

The third regime (III) is marked by the onset of a rate signal detected by the QCMs, which starts in this system at approximately 125 °C. With the onset of FAI evaporation, the pressure as well as the formamidine signal increase. Together with the rate, the pressure increases to $5 \cdot 10^{-5}$ mbar. This is caused by an acceleration of the degradation reactions, which manifests in progressively higher partial pressure of the products.

This trend continues until a temperature of ~ 195 °C is reached, marking the beginning of severe thermal decomposition of the fourth regime (IV). The pressure in this regime rapidly increases to approximately 10^{-3} mbar, forcing the mass spectrometer to shut off (grey shaded area in Fig. 5.2c). The rate quickly rises, reaching up to 32 \AA/s as recorded by the bottom quartz before the source runs empty at approximately 210 °C. Analysis of all the signals detected before and after this point leads to the conclusion that here the material decomposes completely into triazine and hydrogen cyanide at the end of the evaporation. It

5. Evaporation properties of formamidinium iodide

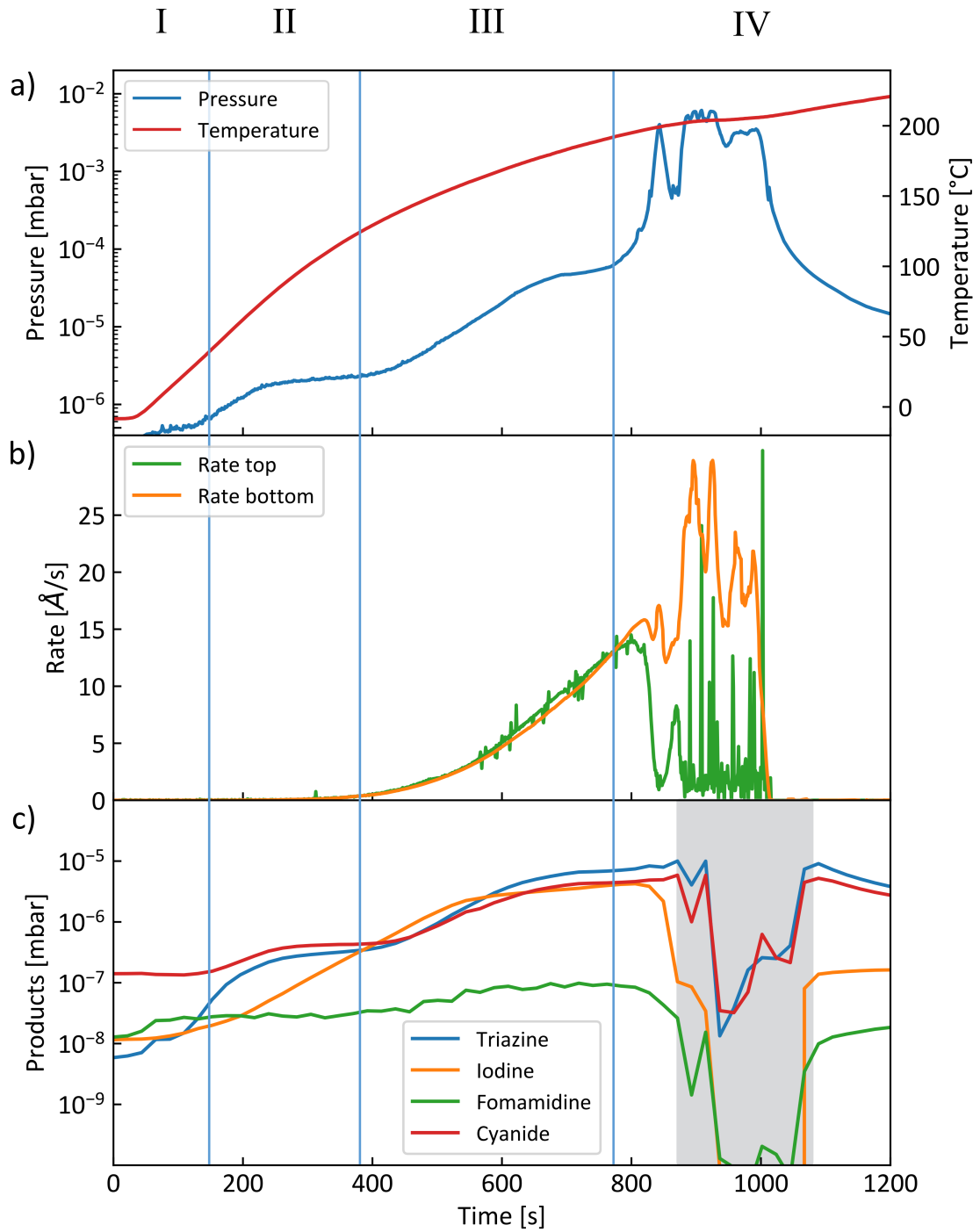


Figure 5.2.: Evaporation of formamidinium iodide: a) chamber pressure in mbar and crucible temperature, b) rate as measured by the bottom sensor close to crucible and by the top sensor close to the substrate, c) evolution of the mass spectrometer signals of the dominant degradation products over the evaporation

is important to note that in this regime, the rate detected by the top QCM decreases significantly, which means that no material can reach the substrate at this pressure level.

All experiments shown in this section were done with FAI purchased from Sigma Aldrich (Purity $\geq 99\%$). Similar measurements with FAI from different suppliers are shown in the Appendix Fig. A.4 and yield comparable results.

5.3. Theoretical considerations during the deposition process

In Sec. 3.1 the general theoretical basis of physical vapour deposition was explained. These considerations will now be applied to the co-evaporation process, particularly in the process involving the organic cation FAI. The focus lies primarily on the organic cation FAI.

To describe the deposition process, we have to recapitulate some formulas from kinetic gas theory. Firstly, the classical gas equation gives us the relation of pressure P , temperature T and particles per volume n :

$$P = nk_B T \quad (5.1)$$

where k_B is the Boltzmann constant. From here, we can follow the mean free path between collisions of one particle (1) in a different particle (2)'s background atmosphere. By considering the radii of the two particles involved, the free mean path in dependence of the particle density n_2 results in:

$$\lambda_1 = \frac{1}{\pi((d_1 + d_2)/2) \left[\frac{1 + \bar{v}_1^2}{\bar{v}_2^2} \right]^2} n_2 \quad (5.2)$$

with \bar{v}_1 and \bar{v}_2 the mean velocities of the respective particles. The mean velocity of a particle depends on the particles' temperature T , and can be followed from Boltzmann distribution for a classical gas:

$$\bar{v} = \left(\frac{8k_B T}{\pi m} \right)^{1/2} \quad (5.3)$$

Where m is the mass of the particle in question. For the list of molecules involved in the evaporation process, see table 5.1.

Keeping the equations mentioned above in mind, we can look at how this affects the experiment results. As already stated in Sec.5.2, the organic salt FAI sublimates separated, in the form of FA and HI, as described by reaction 5.1a),

5. Evaporation properties of formamidinium iodide

| m/Z | Likely molecule | Molecular Formular |
|-----|----------------------|--|
| 172 | Formamidinium iodide | CH ₄ N ₂ I |
| 27 | Hydrogencyanid | HCN |
| 44 | Formamide | CH ₃ N ₂ |
| 81 | Triazine | C ₃ H ₃ N ₃ |
| 54 | Triazine fragment | C ₂ H ₂ N ₂ |

Table 5.1.: Table of reactants and products, involved in the reactions displayed in Fig. 5.1.

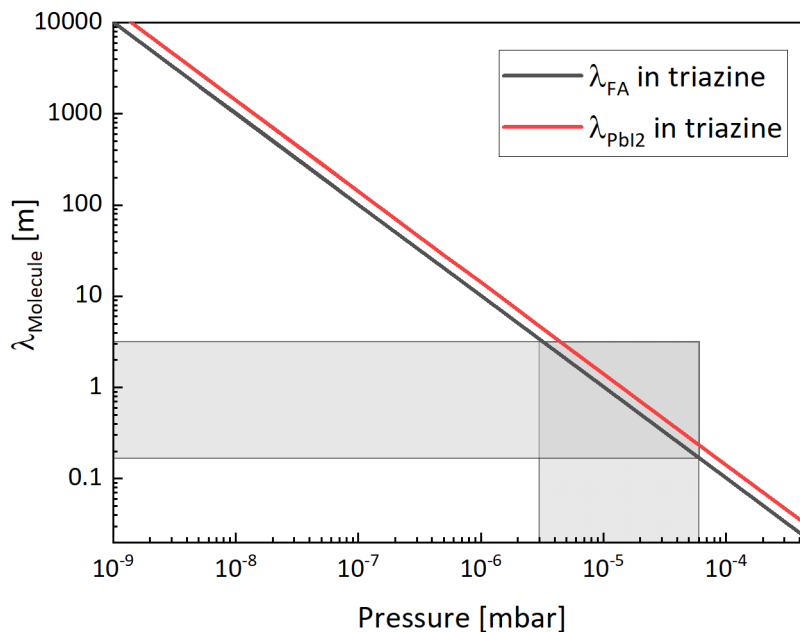


Figure 5.3.: The free mean path of FA and Pbl₂ in triazine atmosphere, the relevant region of evaporation is emphasised in gray.

and can be observed by tracking the background atmosphere (Fig.5.2). Since the molecules' mass and temperature are known, the free mean path can be calculated for the involved particles using formula 5.2 as follows. Using $T_{\text{particle}} = T_{\text{evaporation}} \approx 125 \text{ }^\circ\text{C}$, the diameters $d_{\text{FA}} = 253 \text{ } \mu\text{m}$ [152], $d_{\text{triazine}} = 3 \cdot d_{\text{FA}} = 759 \text{ } \mu\text{m}$ and assuming the atmosphere is pure triazine. The relationship between free mean path and chamber pressure is seen to be directly proportional, as shown in Fig.5.3. From here, we can deduce that the free mean path for a classical gas particle with the properties of FA is in the range of meters for the pressures observed during the evaporation. These calculations show, in contrast to the findings of Abzieher et al.[106], that the organic and inorganic cations are similarly influenced by the pressure. The free mean path of FAI is still high, longer

than the evaporation distance (~ 20 cm). So the difference in deposition rate of FAI and PbI_2 can not be explained by scattering, as described in classical gas theory.

If we now have a closer look at the deposition, it becomes evident that the local pressure above the crucible would be very different from what is measured by the pressure gauge on the chamber walls. By comparing the impingement rate of the evaporated particles on the substrate to the amount of material leaving the crucible, the difference in local pressure can be estimated with Formula 5.1. With a deposition rate $R_{\text{Deposition}} = 1 \text{ \AA/s}$, the density of FAI $\rho_{\text{FAI}} = 2.2 \text{ g/cm}^3$, and the molar mass of FAI $M_{\text{FAI}} = 172 \text{ g/mol}$, the amount of molecules deposited on an area $A = 1 \text{ cm}^2$ results in a particle flow of $n_{\text{Molecules}} = 1.3 \cdot 10^{-10} \text{ Mol/s}$. To estimate the pressure caused by the deposition molecules on the substrate, Volume V is defined by the area A and the distance a molecule travels in one second, which is described by formula 5.3. For an FAI molecule at an evaporation temperature of $T_{\text{evaporation}} = 400 \text{ K}$ this results in $\bar{v}_{\text{FAI}} = 220 \text{ m/s}$. Altogether, this results in a pressure $P_{\text{Molecules}} = 1.95 \cdot 10^{-5} \text{ Pa}$ on the substrate. This value is significantly lower than the chamber pressure, but it gives a rough estimate of the impingement rate of FAI on the substrate. This value has to be compared to the local pressure above the crucible. The weight of a crucible was measured before and after a one-hour 1 \AA/s deposition. The loss in crucible mass $\Delta m_{\text{crucible}} = 69 \text{ mg}$, which yields a particle flow of $n_{\text{Molecules}} = 1.1 \cdot 10^{-7} \text{ Mol/s}$. With the same assumptions as above, the local pressure above the crucible can be estimated to $P_{\text{Molecules}} = 1.7 \cdot 10^{-2} \text{ Pa}$, so three orders of magnitude higher. This higher pressure results in a short free mean path in the order of cm and is accompanied by significant scattering. Since colliding FA molecules can form triazine and fragments of triazine, more material is lost on the way from the crucible than what actually accrues on the substrate.

5.4. Tooling behaviour of Formamidinium iodide

For precise control of FAI deposition, knowledge about not only the material's evaporation behaviour but also its deposition kinetics is essential. Previous studies on the deposition of organic cations during the co-evaporation of perovskite have been described in chapter 2.6.1. In this section, the deposition characteristics and tooling behaviour of FAI found in this work will be presented.

The general aspects of the tooling process are described in Sec. 3.1.2 and will also be applied in this chapter. Since, during co-evaporation, the tooling impacts

5. Evaporation properties of formamidinium iodide

the stoichiometry of the film, an exact determination is essential. The tooling properties of FAI were investigated to determine the influence of an elevated background pressure, which the above-mentioned degradation reaction could cause.

5.4.1. Pressure dependence of the tooling properties

To determine the influence of chamber pressure on the tooling properties, the background pressure was increased via a controlled inlet of nitrogen into the deposition chamber via a mass flow controller. Varying the pressure simulates different evaporation conditions, since the overall pressure is influenced by setup-dependent properties. These properties include things like the pumping speed of the vacuum system, contamination by previous experiments or leakage. This is especially a problem in frequently opened systems, like the one used for these experiments.

The experiment was performed with 300 mg FAI, which was prepared according to the procedure described in Sec. 4.1. The tooling is performed according to the process described in Sec. 3.2.3. The standard deposition rate for perovskite production (1.6 \AA/s) was set via the stabilised rate control of the deposition software.

When the deposition rate of $r_{\text{Deposition}} = 1.6 \text{ \AA/s}$ is reached, the pressure in the chamber increased from the base pressure to $P_1 = 5 \cdot 10^{-6} \text{ mbar}$. This pressure value is stable over the 500 s of the experiment. A tooling factor of $t_1 = 19.5\%$ was measured here. The next pressure value was set to $P_2 = 2 \cdot 10^{-5} \text{ mbar}$, and the tooling measurement was started when the pressure stabilised. Periodic variations in pressure originate from the atmospheric stabilisation of the glove-box, which is connected with the vacuum chamber via the valve of the mass flow controller. At pressure P_2 , the tooling factor decreased to $t_2 = 18.1\%$. At a pressure of $P_3 = 1 \cdot 10^{-4} \text{ mbar}$, the amount of material recorded by the top sensor dropped further to $t_3 = 15.8\%$. This $\approx 4\%$ decrease is well within the range of variation reported in previous studies [107, 153, 154]. This leads to the conclusion that only the chamber pressure influences the amount of material that can reach the top of the chamber.

As a reference measurement, the tooling factors were determined for PbI_2 in the same conditions. Here a decrease from $t_1 = 27.1\%$ at $P_1 = 5 \cdot 10^{-6} \text{ mbar}$ to $t_3 = 24.5\%$ at $P_3 = 1 \cdot 10^{-4} \text{ mbar}$. The measurement is shown in the Appendix Fig. A.5. This $\approx 3\%$ decrease corroborates the idea that less material reaches the top of the chamber at higher pressures, since increased pressure causes

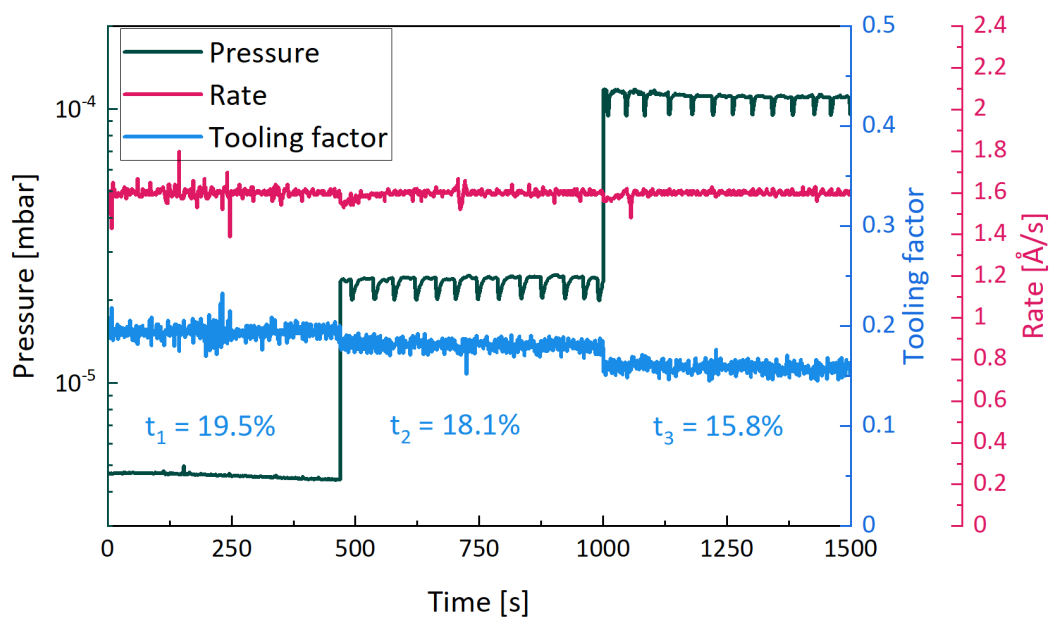


Figure 5.4.: Tooling properties of FAI under different background pressures: black: the background pressure, red: the deposition rate as observed by the bottom sensor, blue: the deposition ratio of top sensor and bottom sensor

more scattering, thereby shortening the free mean path. It is important to note is that the tooling factors of PbI_2 are higher than for FAI, although the geometry is identical. This indicates a higher ideality of the emission characteristics of the inorganic salt compared to the organic salt.

5.4.2. Development of tooling factor

In the experiment described in the previous section, the rate was set to a constant value and stabilised there. However, for applications in commercial production lines, a higher evaporation rate might be necessary to increase the production throughput. As shown in Sec. 5.1, FAI can not be heated higher than $\sim 200^\circ\text{C}$ due to a complete material degradation in this temperature range. The source power was limited to 35% of the maximum to avoid this. This experiment is performed with 300 mg of pretreated FAI, under the same conditions in the experiments described before.

To determine the rate dependence of the tooling factor, the crucible is heated constantly, and the evaporation parameters are recorded. The tooling factor increases throughout the evaporation. After heating for 1500 s, the deposition rate reaches a maximum of 8 \AA/s at a stable temperature of 170°C . It is impor-

5. Evaporation properties of formamidinium iodide

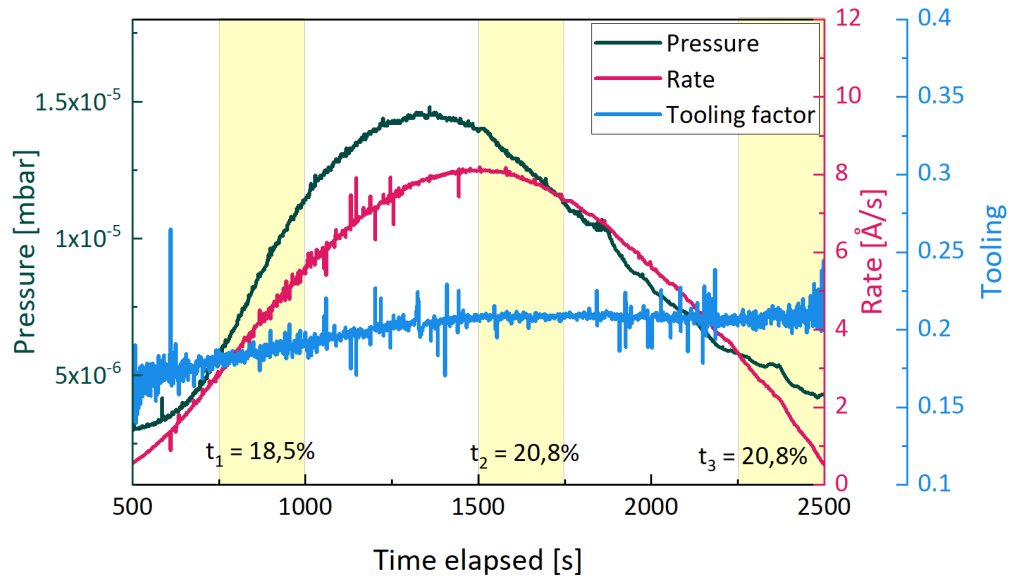


Figure 5.5.: The tooling behaviour of FAI at high rates. The pressure is depicted in black, the measured rates in orange and the tooling factor in blue.

It is important to note that the maximum pressure is detected before the maximum of the deposition rate. This highlights the idea that degradation of FAI with gaseous products is happening in parallel with the evaporation, and the proportion of the reactions depends on the amount of material in the crucible. We observed that the tooling factor changes depending on the deposition rate. Some discrepancies appear upon closer investigation. The difference in the tooling factors cannot be related to any of the processing parameters discussed earlier. The dependence of the tooling factor on the process parameters is depicted in the Appendix A.6. It is evident that the tooling factor does not depend on the pressure, the rate, or the temperature. This leaves only the constantly-changing crucible filling that occurs throughout the evaporation as the critical parameter causing this behaviour.

The tooling factor varies at different points in the evaporation, even when the measured deposition rate stays the same. This clearly shows that the tooling factor is not rate-dependent. Since we have already shown that the background pressure is influenced by the fullness of the crucible because more reactive volume is present. And the tooling factor is pressure and filling dependent. This is a self-influencing cycle that changes throughout the course of one evaporation. A uniform layer is hard to accomplish since the decreasing pressure and the change in evaporation geometry with an emptier crucible both increase the

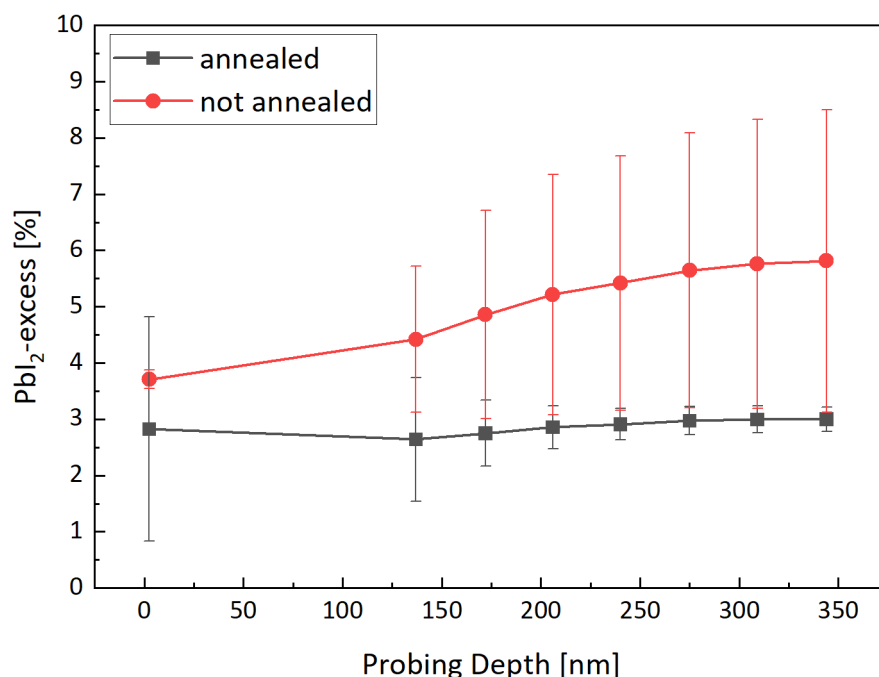


Figure 5.6.: Relative intensity of the PbI_2 -peak at 0.89 \AA^{-1} peak, compared to the amount of overall material, depending on the probing depth.

tooling factor affecting in turn the amount of material reaching the substrate.

5.4.3. Influence on material composition

The gradual increase of the tooling factor of FAI over the course of an evaporation should lead to an FAI-poorer film at the beginning and an FAI-richer stoichiometry at the end of the deposition. To verify this assumption, the films were measured via GIWAXS with a variation of the angle between the sample and the probing beam. By varying this angle, the probing depth increases from low angles to higher angles, thereby providing information about deeper regions of the film. To determine the composition changes through the film, the integrated angular signals of the 0.89 \AA^{-1} peak in relation to the overall amount of material were plotted as shown in Fig. 5.6.

The reduced amount of PbI_2 at different depths in the unannealed sample shows that the material excess decreases towards the surface of the film. This shows that more FAI is incorporated into the film towards the end of the deposition, which becomes evident in an increase of the (100)-perovskite peak at lower probing depth. The development of the intensity of the (100)-perovskite peak is

5. Evaporation properties of formamidinium iodide

depicted in the Appendix Fig. A.7. This diagram nicely shows that the change in tooling factor observed previously influences the material composition throughout the 450 nm-thick deposited layer from top to bottom. The difference is small but still in the range of some percent, which is a common stoichiometric variation[154]. Adding an annealing step post-evaporation then redistributes the material, and the PbI_2 excess becomes constant throughout the whole layer. This change in film stoichiometry makes it evident that an annealing step is necessary for a uniform layer and better device performance since the stoichiometry influences the material's band gap and the doping level, as it was found by Dänekamp et al.[155]. Here, the authors evaporated a homojunction of p- and n-type MAPbI_3 by changing the stoichiometry of the film. This creates a type of self-doping by vacancies and interstitials, as explained in Sec. 2.4.1. Although the stoichiometry variation is higher in this case, a similar effect can be expected for this perovskite composition. This would affect charge carrier extraction in a photovoltaic device since the p-i-n structure used for the solar cell devices (Sec. 4.6.2) is designed in a manner contrary to the n-doping trend induced by an increase of PbI_2 interstitials.

5.5. Summary

In this chapter, we investigated the evaporation behaviour of the most significant material during co-evaporation, formamidinium iodide. Most importantly, the degradation process found by Perez et al.[151], where the material degrades into the highly volatile compounds sym-triazine and hydrogen cyanide, takes place during the deposition process. It was found that these degradation products are the main reason for the high background pressure during the evaporation process. FAI degrades completely above 195 °C, so deposition above this temperature is not possible. Since the degradation reactions start even before the onset of the rate acquisition, we conclude that this process is unavoidable during the deposition. The speed of the degradation reaction and the amount of resulting products in the chamber's atmosphere were found to depend on the amount of material left in the crucible.

Furthermore, it was found that the tooling factor, and thus the amount of material reaching the substrate surface, depends on both the background pressure and the material distribution in the crucible. Since the tooling factor decreases when the background pressure is increased with a nitrogen inlet but increases with less material in the crucible, it was thought that these two effects could com-

compensate each other. The observed decrease in excess PbI_2 shows that this is not the case, leading to a stoichiometric change throughout the whole layer. Annealing the film decreases the amount of excess PbI_2 by redistributing it equally throughout the entire layer. This result underlines the importance of adding a post-evaporation annealing step to compensate for fluctuations during the deposition process.

6. Summary & Outlook

Despite the exceptional optoelectronic properties of hybrid mixed halide perovskite materials, several problems must be addressed for this material to revolutionise solar cell technology. Aside from the problems of instability and toxicity, which were outside of the scope of this thesis, the processability and reproducibility of the perovskite remain a major impediment to perovskite's transition from the laboratory to the factory.

In this work, the vacuum deposition properties of triple-source co-evaporated $\text{FA}_{1-x}\text{Cs}_x\text{PbI}_{3-x}\text{Br}_x$ were investigated. The main focus was on the influence of the background pressure on the properties of the material and the deposition behaviour of the most important component, the organic halide salt formamidinium iodide.

It was found that a change in background pressure during evaporation influences the material in several ways. Most importantly, the stoichiometry of the perovskite material changes since FAI is more sensitive to pressure changes than the inorganic components. With increasing pressure, the incorporation of the organic salt decreases, resulting in a film with a higher bromine content and an increased PbI_2 -excess. The resulting bandgap increase did not lead to a statistically significant increase in the V_{OC} of solar cell devices with a p-i-n structure. Along with stoichiometry deviations, a change in crystallisation orientation was measured, which is also known to influence the resulting device performance [120].

Throughout the experiments, the instability of the co-evaporation process became evident. Measurable process parameters, like background pressure, deposition rates, and substrate temperature, are known to affect the outcome. Additionally, harder-to-control influences like the cleanliness of the chamber (a cleaning step does not necessarily lead to a better result) or variations in crucible fillings have an influence on the result. It was found that fluctuations of the evaporation behaviour of formamidinium iodide are the main culprit of problems with reproducibility. This led to a thorough investigation of the evaporation behaviour of FAI specifically.

The organic halide salt formamidinium iodide has shown several problematic

6. Summary & Outlook

properties that hinder reproducible evaporation. Firstly, the material is sold with a significant amount of impurities, which have to be gassed out before the deposition since they impair the vacuum in the deposition chamber. Several of these foreign molecules were found by measuring the background atmosphere during evaporation with a mass spectrometer. These molecules are evidence of decomposition reactions. These reactions happen in parallel to the evaporation, strongly influencing the background pressure as these products are very volatile. The pressure in the vessel is consequently directly dependent on the processing temperature and the crucible filling of FAI. Besides the varying pressure and its influence on the composition, the filling and the distribution of the material inside the crucible influence the amount of material that reaches the substrate, compared to what is measured at the QCMs. Here, an increase in tooling factor was found throughout an evaporation since the material starts to evaporate from the walls and later from the centre of the crucible.

In conclusion, triple source co-evaporation of $\text{FA}_{1-x}\text{Cs}_x\text{PbI}_{3-x}\text{Br}_x$ was successfully implemented for the production of solar cells. Through the detailed tracking of all accessible process parameters, a significant instability of the process became evident since, although every controllable parameter was kept as constant as possible, the results changed. This will be very problematic for later implementation in the PV industry since variations in commercial products are unacceptable. Further questions arise from the degradation of FAI during film production and the various influences on the final result, that is, whether the process can be finely supervised and adjusted enough to compensate for these variations.

There are ultimately still open questions regarding the evaporation of perovskite, especially the transition to industrial-scale evaporation systems and the extent of new problems arising there are of increased interest. To ensure well-controlled evaporation on larger scales, a novel evaporation source design could solve the problem. One important criterion here is to keep the amount of heated FAI constant. This issue can be solved by replenishing material during evaporation to compensate for the evaporating and decomposing material in the crucible.

Another approach could be the exclusion of FAI in the composition. Since MAI is also known to have problematic evaporation behaviour, the inorganic salt CsI is the evident candidate due to its unproblematic sublimation behaviour. Besides the better processability in vacuum, Cs-based perovskites also have shown a higher long-term stability[156] and also fully thermally-evaporated de-

vices based on CsPbI₃ have already been shown[157]. One disadvantage is the lower PCE up to now and the larger bandgap of the resulting fully-inorganic perovskite in comparison to FA-based compounds, which limits the maximum PCE.

The next years will show if perovskite-based solar cells can accomplish the transition from the laboratories to the real world. It would be a major turning point for photovoltaics, if future devices are made out of perovskite, and if so, whether co-evaporation is the way to go remains an open question.

A. Appendix

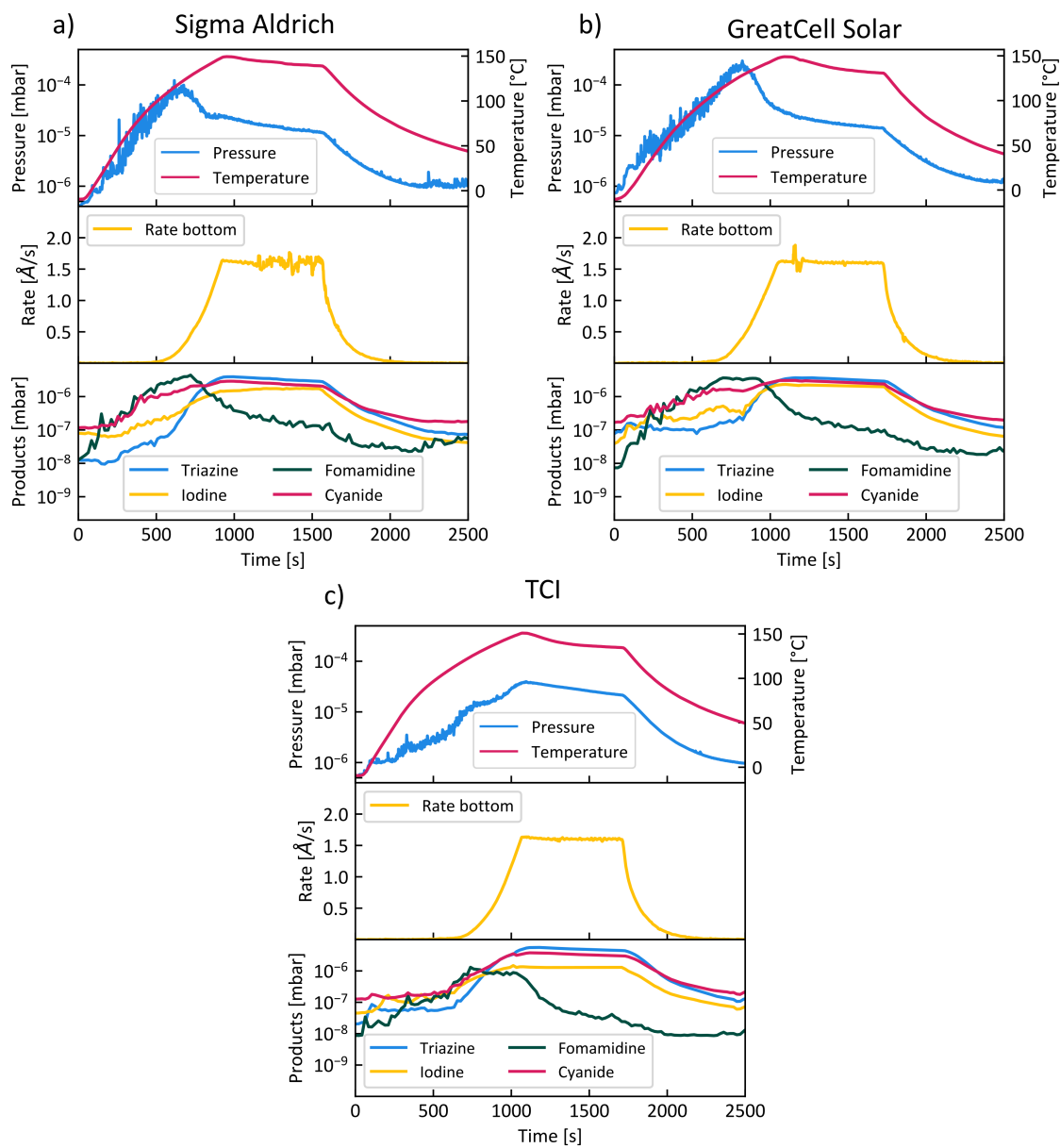


Figure A.1.: Evaporation properties of FAI from different vendors; a),b),c): Outgassing behaviour of materials from different suppliers. a),b) show very similar behaviour, which leads to the assumption that the material is from the same production line, c) shows a lower increase in pressure in the beginning, which originates from a finer milled powder.

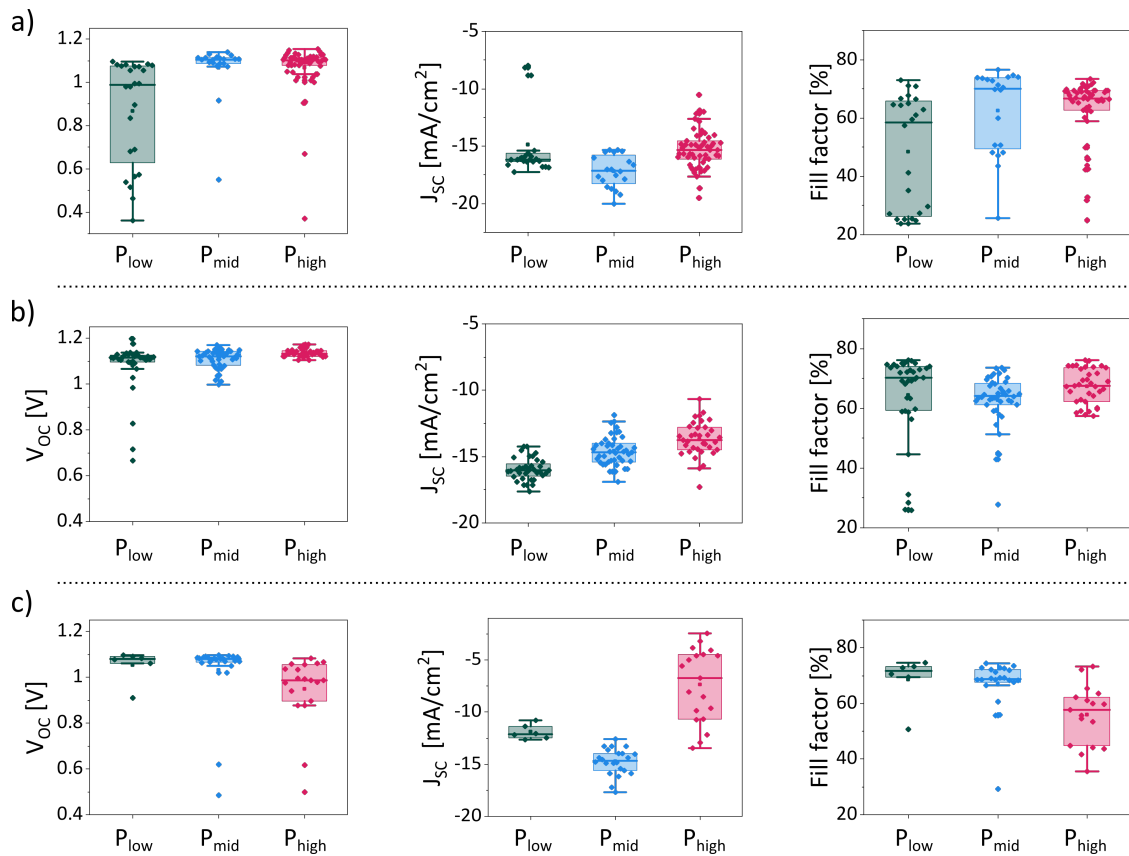


Figure A.2.: The photovoltaic parameters corresponding to the batches presented in Fig. 4.12a),b), and c): The open-circuit voltage (V_{oc}), short current density (J_{sc}), and fill factor (FF) are displayed. $P_{low}=5 \cdot 10^{-6}$ mbar, $P_{mid}=2 \cdot 10^{-5}$ mbar, $P_{high}=1 \cdot 10^{-4}$ mbar.

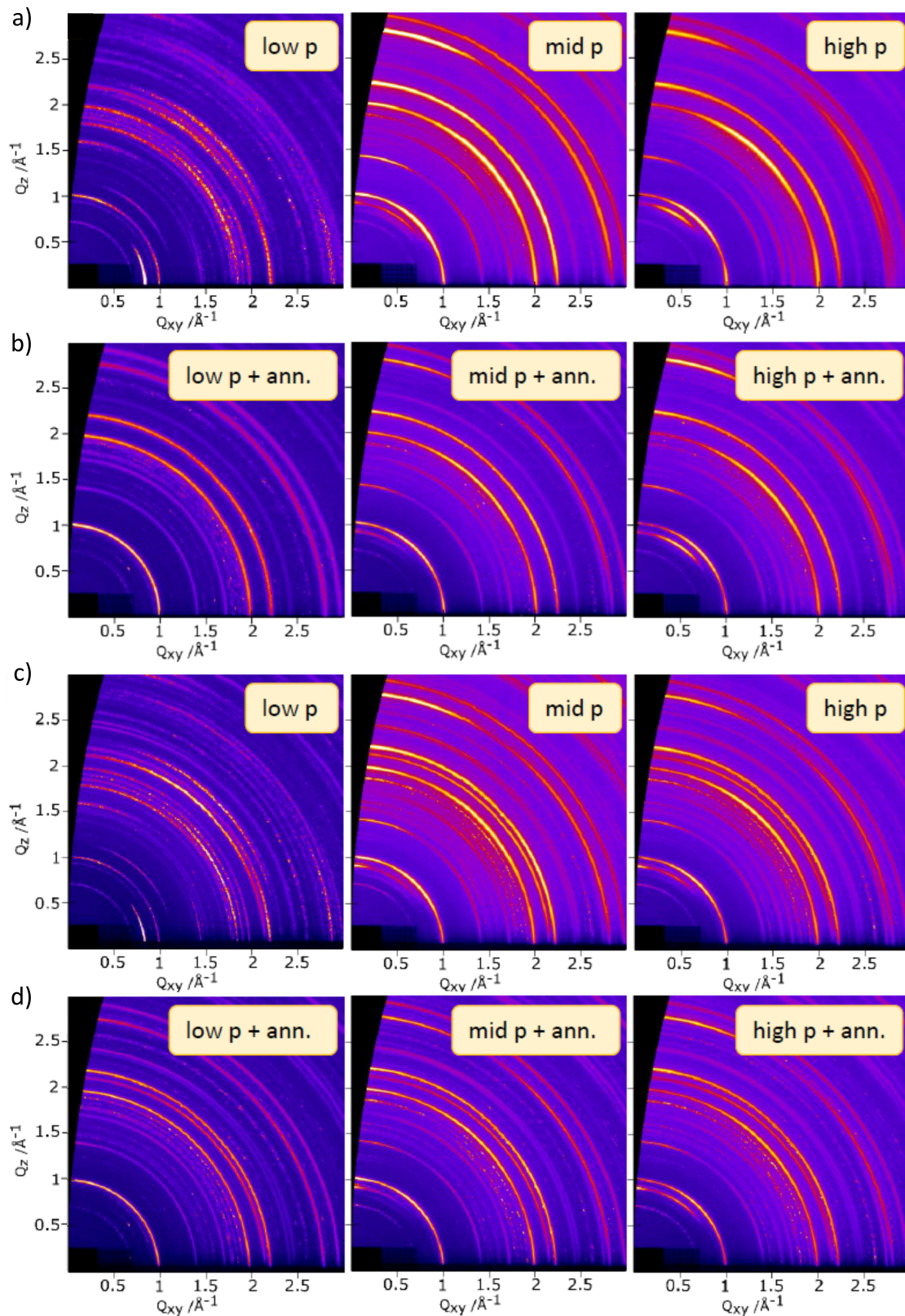


Figure A.3.: Reciprocal space maps of GIWAXS measurements of samples prepared at varying background pressures: a) surface, as deposited, b) surface annealed, c) bulk as deposited, d) bulk annealed. $P_{\text{low}}=5 \cdot 10^{-6}$ mbar, $P_{\text{mid}}=2 \cdot 10^{-5}$ mbar, $P_{\text{high}}=1 \cdot 10^{-4}$ mbar.

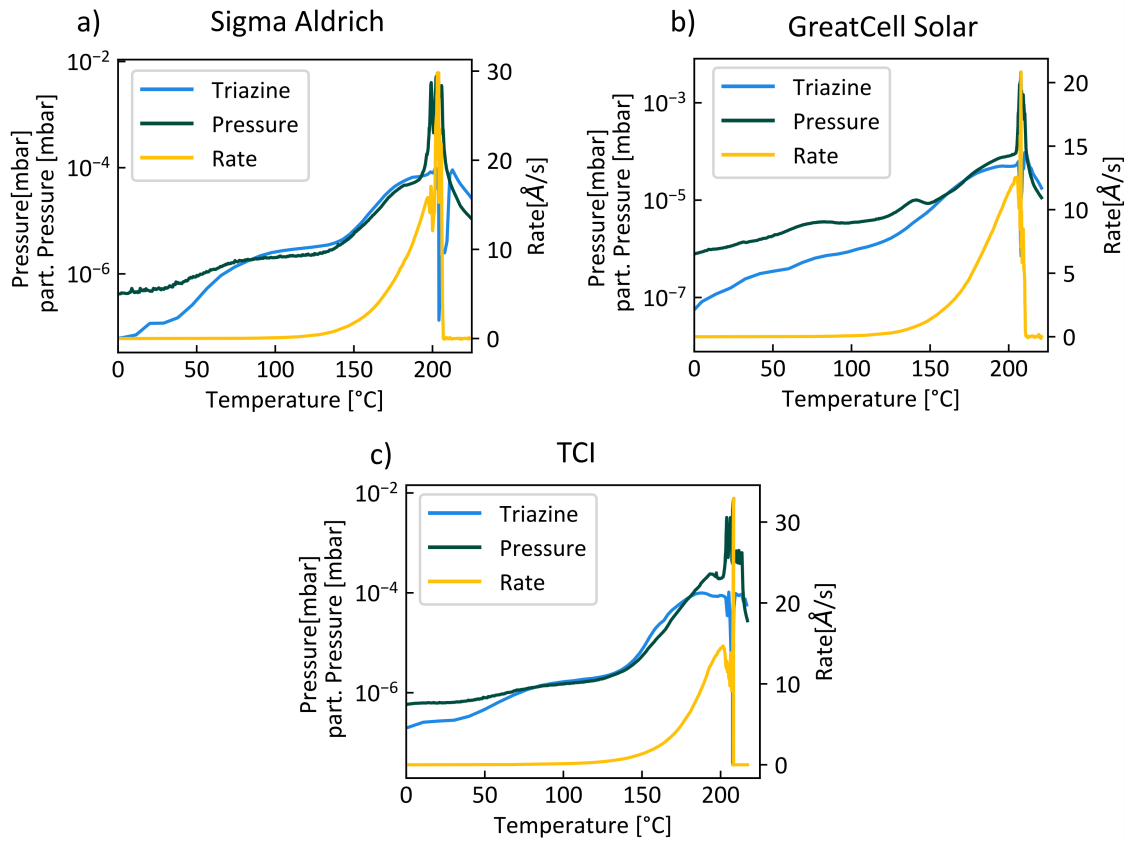


Figure A.4.: Degradation properties of FAI from different vendors in dependence of the crucible temperature

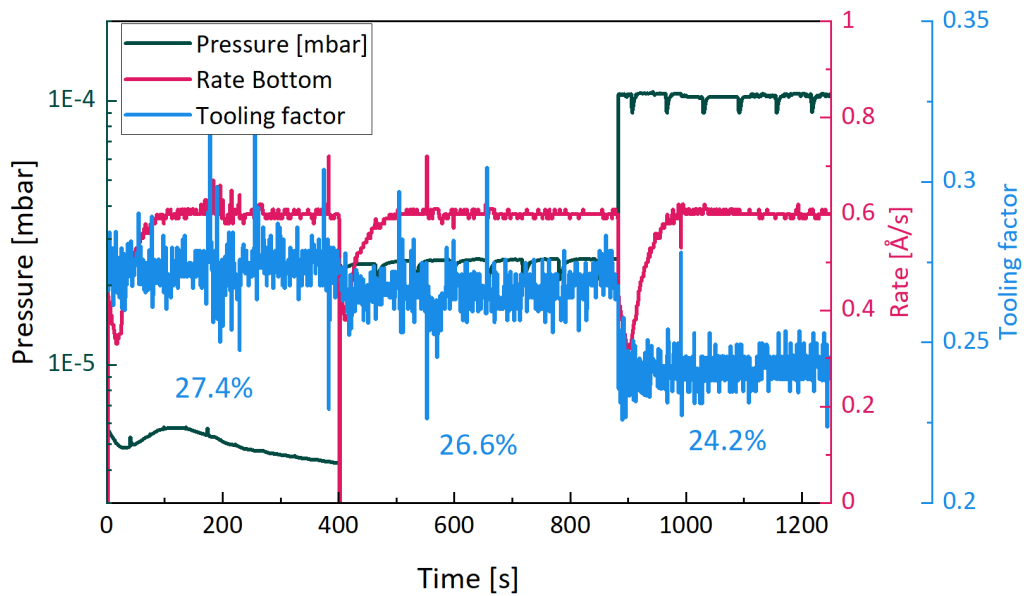


Figure A.5.: Tooling properties of Pbl₂ depending on the background pressure

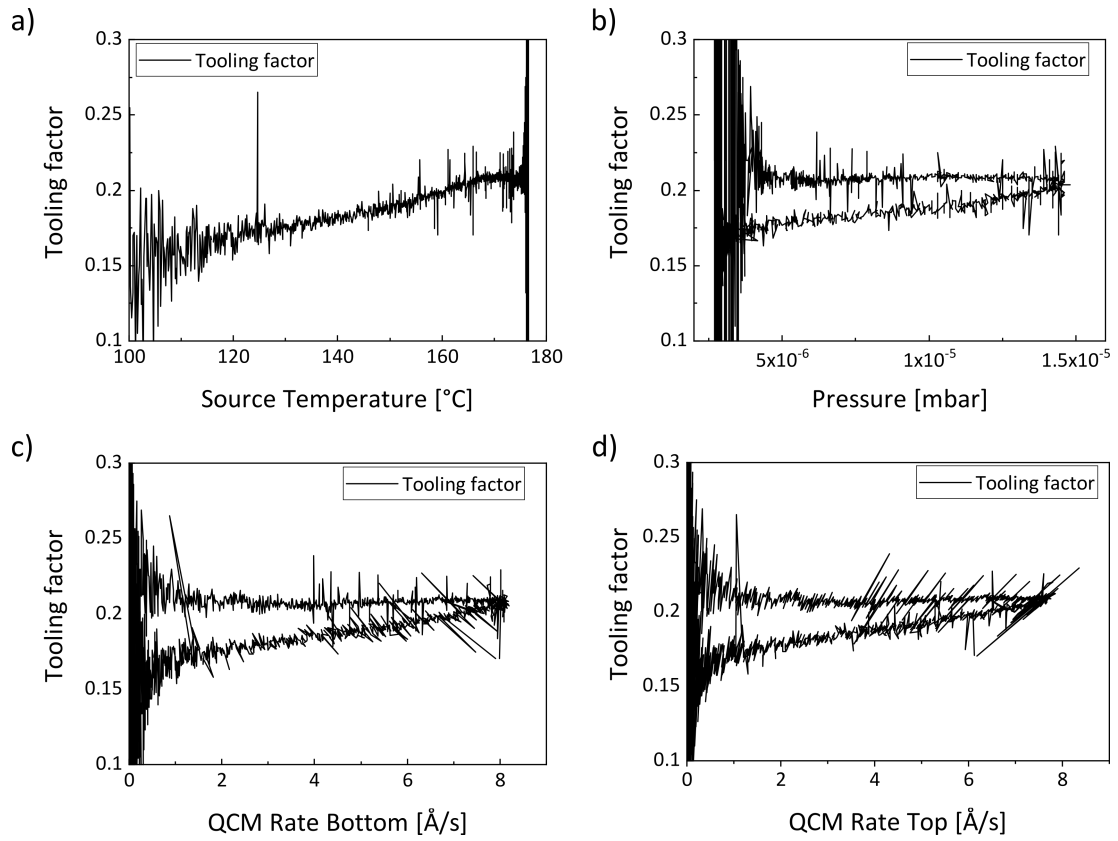


Figure A.6.: The tooling factor depicted in Fig. 5.5 in dependence of various process parameters: a) the source temperature, b) the pressure, c) the rate measured by the bottom QCM, d) the rate measured by the top QCM.

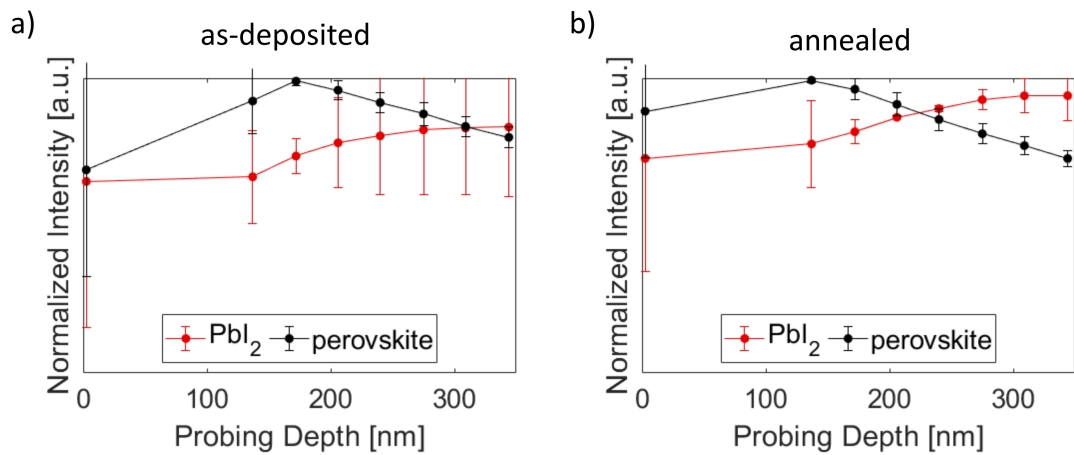


Figure A.7.: Development of the (100)-perovskite peak with increasing probing depth: a) an as deposited thin-film, b) an annealed thin-film (10min at 100 °C)

List of Figures

| | |
|--|----|
| 1.1. Planned PV-construction and price development | 3 |
| 2.1. Exemplary device stack of thin-film solar cell | 6 |
| 2.2. Working principle of a CdTe thin-film solar cell | 9 |
| 2.3. Data analysis from the perovskite database-project | 12 |
| 2.4. Perovskite structure in orthorhombic crystallisation | 14 |
| 2.5. Band structure of perovskite and energy levels of defects | 16 |
| 2.6. Band gap variations of metal halide perovskites | 17 |
| 2.7. Schematic illustration of different perovskite deposition method | 19 |
| 2.8. Scematics of scalable linear solution processing techniques | 21 |
| 2.9. The adhesion of MAI to the substrate | 24 |
| 2.10. Illustration for growth conditions | 25 |
| 3.1. Illustration of the vapor deposition of a thin film | 28 |
| 3.2. Picture of the vacuum deposition setup | 30 |
| 3.3. XRD-measurement setup | 33 |
| 3.4. Schematic of an SEM-setup | 35 |
| 3.5. Schematics of a typical AFM configuration | 36 |
| 3.6. Illustration of XPS-measurement | 37 |
| 4.1. Preheating of fresh FAI: Pressure development | 40 |
| 4.2. Preheating procedure of fresh FAI: mass spectrometry measurement | 41 |
| 4.3. X-ray diffractogram of as-deposited $\text{FA}_{1-x}\text{Cs}_x\text{PbI}_{3-x}\text{Br}_x$ | 44 |
| 4.5. Schematics of the perovskite crystallite orientation | 47 |
| 4.6. SEM-pictures of as-deposited $\text{FA}_{1-x}\text{Cs}_x\text{PbI}_{3-x}\text{Br}_x$ | 48 |
| 4.7. Tauc plot from absorption measurements | 49 |
| 4.8. Photoluminescence spectra of $\text{FA}_{1-x}\text{Cs}_x\text{PbI}_{3-x}\text{Br}_x$ -films | 50 |
| 4.9. XPS measurement results | 51 |
| 4.10. Solar cell stack of the devices | 52 |
| 4.11. Thickness measurements of $\text{FA}_{1-x}\text{Cs}_x\text{PbI}_{3-x}\text{Br}_x$ -films | 53 |
| 4.12. Photo conversion efficiency of solar cell devices | 54 |

List of Figures

| | |
|--|----|
| 5.1. Degradation reactions of formamidinium iodide | 58 |
| 5.2. Evaporation parameters of formamidinium iodide | 60 |
| 5.3. The free mean path of FA and PbI_2 in triazine atmosphere | 62 |
| 5.4. Tooling properties of FAI under different background pressures . . | 65 |
| 5.5. The tooling behaviour of FAI at high rates | 66 |
| 5.6. PbI_2 -excess depth profile | 67 |
| A.1. Evaporation properties of FAI from different vendors | 76 |
| A.2. The photovoltaic parameters: The open-circuit voltage (V_{OC}), short current density (j_{SC}), and fill factor (FF) | 77 |
| A.3. Reciprocal space maps measured of samples prepared at varying background pressures | 78 |
| A.4. Degradation properties of FAI from different vendors | 79 |
| A.5. Tooling properties of PbI_2 depending on the background pressure | 79 |
| A.6. The tooling factor in dependence of various process parameters . | 80 |
| A.7. Development of the (100)-perovskite peak with increasing prob- ing depth | 80 |

List of Tables

| | |
|--|----|
| 4.1. Table of molecules leaving the material during preheating | 41 |
| 4.2. Analysis of the XRD peak fit | 45 |
| 5.1. Table of reactants and products, involved in the degradation re- actions | 62 |

List of Abbreviations

| | |
|---------------------|--|
| AFM | atomic force microscope |
| arb. | arbitrary unit |
| (α -Si) | amorphous silicon |
| BCP | bathocuproine |
| CIGS | copper indium gallium diselenide |
| CIS | copper indium sulfide |
| deg. | degree |
| DFT | density functional theory |
| DMSO | dimethyl sulfoxide |
| DMF | dimethylformamide |
| ETL | electron transport layer |
| FF | fill factor |
| FTO | fluorine-doped tin oxide |
| FA | formamidinium |
| FWHM | full width at half maximum |
| GIWAXS | grazing incidence wide-angle X-ray scattering |
| GA | guanidinium |
| HTL | hole-transport layer |
| ITO | indium tin oxide |
| MA | methylammonium |
| V _{oc} | open-circuit voltage |
| PC ₆₁ BM | 3H-Cyclopropa[1,9] [5,6]fulleren-C60-1h-3-butanoic acid-3-phenyl-methylester |
| PERCs | passivated emitter and rear cells |
| PV | photovoltaic |
| PVD | physical vapour deposition |
| PTAA | poly[bis(4-phenyl)(2,4,6-trimethylphenyl)amine] |
| PCE | power conversion efficiency |
| QCM | quartz crystal microbalances |
| SEM | scanning electron microscopy |
| j _{sc} | short current density |
| TCO | transparent conductive electrode |
| XRD | X-ray diffraction |
| XPS | X-ray photoelectron spectroscopy |

Bibliography

- [1] A. Einstein, "Über einen die Erzeugung und Verwandlung des Lichtes betreffenden heuristischen Gesichtspunkt", *Annalen der Physik* **322**, 132–148 (1905).
- [2] Fraunhofer ISE, "Aktuelle Fakten zur Photovoltaik in Deutschland", *Brand* **49**, 1–51 (2012).
- [3] A. Kojima, K. Teshima, Y. Shirai, and T. Miyasaka, "Organometal halide perovskites as visible-light sensitizers for photovoltaic cells", *Journal of the American Chemical Society* **131**, 6050–6051 (2009).
- [4] *NREL-chart*, <https://www.nrel.gov/pv/cell-efficiency.htm>, 2022.
- [5] G. Hong, X. Gan, C. Leonhardt, Z. Zhang, J. Seibert, J. M. Busch, and S. Bräse, "A Brief History of OLEDs—Emitter Development and Industry Milestones", *Advanced Materials* **33**, 2005630 (2021).
- [6] S. Reineke, M. Thomschke, B. Lüssem, and K. Leo, "White organic light-emitting diodes: Status and perspective", *Reviews of Modern Physics* **85**, 1245–1293 (2013).
- [7] M. Liu, M. B. Johnston, and H. J. Snaith, "Efficient planar heterojunction perovskite solar cells by vapour deposition", *Nature* **501**, 395–398 (2013).
- [8] C. Momblona, L. Gil-Escrig, E. Bandiello, E. M. Hutter, M. Sessolo, K. Lederer, J. Blochwitz-Nimoth, and H. J. Bolink, "Efficient vacuum deposited p-i-n and n-i-p perovskite solar cells employing doped charge transport layers", *Energy Environ. Sci.* **9**, 3456–3463 (2016).
- [9] J. Li, H. Wang, X. Y. Chin, H. A. Dewi, K. Vergeer, T. W. Goh, J. W. M. Lim, J. H. Lew, K. P. Loh, C. Soci, T. C. Sum, H. J. Bolink, N. Mathews, S. Mhaisalkar, and A. Bruno, "Highly Efficient Thermally Co-evaporated Perovskite Solar Cells and Mini-modules", *Joule* **4**, 1035–1053 (2020).
- [10] J. Feng, Y. Jiao, H. Wang, X. Zhu, Y. Sun, M. Du, Y. Cao, D. Yang, and S. F. Liu, "High-throughput large-area vacuum deposition for high-performance formamidine-based perovskite solar cells", *Energy and Environmental Science* **14**, 3035–3043 (2021).

- [11] J. Jeong, M. Kim, J. Seo, H. Lu, P. Ahlawat, A. Mishra, Y. Yang, M. A. Hope, F. T. Eickemeyer, M. Kim, Y. J. Yoon, I. W. Choi, B. P. Darwich, S. J. Choi, Y. Jo, J. H. Lee, B. Walker, S. M. Zakeeruddin, L. Emsley, U. Rothlisberger, A. Hagfeldt, D. S. Kim, M. Grätzel, and J. Y. Kim, "Pseudo-halide anion engineering for α -FAPbI₃ perovskite solar cells", *Nature* **592**, 381–385 (2021).
- [12] A. G. Aberle, "Thin-film solar cells", *Thin Solid Films* **517**, 4706–4710 (2009).
- [13] X. Mathew, J. P. Enriquez, A. Romeo, and A. N. Tiwari, "CdTe/CdS solar cells on flexible substrates", *Solar Energy* **77**, 831–838 (2004).
- [14] Y. Li, G. Xu, C. Cui, and Y. Li, "Flexible and Semitransparent Organic Solar Cells", *Advanced Energy Materials* **8**, 1701791 (2018).
- [15] Y. Li, L. Meng, Y. Yang, G. Xu, Z. Hong, Q. Chen, J. You, G. Li, Y. Yang, and Y. Li, "High-efficiency robust perovskite solar cells on ultrathin flexible substrates", *Nature Communications* **7**, 10214 (2016).
- [16] R. Wuerz, A. Eicke, M. Frankenfeld, F. Kessler, M. Powalla, P. Rogin, and O. Yazdani-Assl, "CIGS thin-film solar cells on steel substrates", *Thin Solid Films* **517**, 2415–2418 (2009).
- [17] K. Schulze, B. Maennig, K. Leo, Y. Tomita, C. May, J. Hüpkes, E. Brier, E. Reinold, and P. Bäuerle, "Organic solar cells on indium tin oxide and aluminum doped zinc oxide anodes", *Applied Physics Letters* **91**, 1–4 (2007).
- [18] Y. Park, L. Bormann, L. Müller-Meskamp, K. Vandewal, and K. Leo, "Efficient flexible organic photovoltaics using silver nanowires and polymer based transparent electrodes", *Organic Electronics* **36**, 68–72 (2016).
- [19] S. Schubert, J. Meiss, L. Müller-Meskamp, and K. Leo, "Improvement of Transparent Metal Top Electrodes for Organic Solar Cells by Introducing a High Surface Energy Seed Layer", *Advanced Energy Materials* **3**, 438–443 (2013).
- [20] L. E. Polander, P. Pahner, M. Schwarze, M. Saalfrank, C. Koerner, K. Leo, L. E. Polander, P. Pahner, M. Schwarze, M. Saalfrank, C. Koerner, and K. Leo, "Hole-transport material variation in fully vacuum deposited perovskite solar cells Hole-transport material variation in fully vacuum deposited perovskite solar cells", *APL Materials* **2**, 1–6 (2014).
- [21] P.-K. Kung, M.-H. Li, P.-Y. Lin, Y.-H. Chiang, C.-R. Chan, T.-F. Guo, and P. Chen, "A Review of Inorganic Hole Transport Materials for Perovskite Solar Cells", *Advanced Materials Interfaces* **5**, 1800882 (2018).
- [22] W. Tress, K. Leo, and M. Riede, "Influence of Hole-Transport Layers and Donor Materials on Open-Circuit Voltage and Shape of I-V Curves of Organic Solar Cells", *Advanced Functional Materials* **21**, 2140–2149 (2011).

- [23] E. Siebert-Henze, V. Lyssenko, J. Fischer, M. Tietze, R. Brueckner, T. Menke, K. Leo, and M. Riede, "Electroabsorption studies of organic p-i-n solar cells: Increase of the built-in voltage by higher doping concentration in the hole transport layer", *Organic Electronics* **15**, 563–568 (2014).
- [24] V. M. Le Corre, M. Stolterfoht, L. Perdigón Toro, M. Feuerstein, C. Wolff, L. Gil-Escrig, H. J. Bolink, D. Neher, and L. J. A. Koster, "Charge Transport Layers Limiting the Efficiency of Perovskite Solar Cells: How to Optimize Conductivity, Doping, and Thickness", *ACS Applied Energy Materials* **2**, 6280–6287 (2019).
- [25] G. Bauhuis, J. Schermer, P. Mulder, M. Voncken, and P. Larsen, "Thin film GaAs solar cells with increased quantum efficiency due to light reflection", *Solar Energy Materials and Solar Cells* **83**, 81–90 (2004).
- [26] A. K. Chandiran, M. K. Nazeeruddin, and M. Grätzel, "The Role of Insulating Oxides in Blocking the Charge Carrier Recombination in Dye-Sensitized Solar Cells", *Advanced Functional Materials* **24**, 1615–1623 (2014).
- [27] M. Degani, Q. An, M. Albaladejo-Siguan, Y. J. Hofstetter, C. Cho, F. Paulus, G. Grancini, and Y. Vaynzof, "23.7% Efficient inverted perovskite solar cells by dual interfacial modification", *Science Advances* **7**, 1–10 (2021).
- [28] D. Bouhafs, "Design and simulation of antireflection coating systems for optoelectronic devices: Application to silicon solar cells", *Solar Energy Materials and Solar Cells* **52**, 79–93 (1998).
- [29] W. Qarony, M. I. Hossain, R. Dewan, S. Fischer, V. B. Meyer-Rochow, A. Salleo, D. Knipp, and Y. H. Tsang, "Approaching Perfect Light Incoupling in Perovskite and Silicon Thin Film Solar Cells by Moth Eye Surface Textures", *Advanced Theory and Simulations* **1**, 1800030 (2018).
- [30] D. M. Callahan, J. N. Munday, and H. A. Atwater, "Solar Cell Light Trapping beyond the Ray Optic Limit", *Nano Letters* **12**, 214–218 (2012).
- [31] J. Czochralski, "Ein neues Verfahren zur Messung der Kristallisationsgeschwindigkeit der Metalle", *Zeitschrift für Physikalische Chemie* **92U**, 219–221 (1918).
- [32] W. Wang, *N-type market growth*, <https://www.pv-magazine.com/2020/10/20/n-type-market-growth/>, 2020.
- [33] F. Ye, W. Deng, W. Guo, R. Liu, D. Chen, Y. Chen, Y. Yang, N. Yuan, J. Ding, Z. Feng, P. P. Altermatt, and P. J. Verlinden, "22.13% Efficient industrial p-type mono PERC solar cell", 2017 IEEE 44th Photovoltaic Specialist Conference, PVSC 2017, 1614–1618 (2017).

- [34] M. Hutchins, *Solar Frontier hits new CIS cell efficiency record*, <https://www.pv-magazine.com/2019/01/21/solar-frontier-hits-new-cis-cell-efficiency-record/>, 2019.
- [35] C. A. Miller, I. M. Peters, and Z. Shivam, "Thin Film CdTe Photovoltaics and the U.S. Energy Transition in 2020", (2020).
- [36] S. Philipps, "Photovoltaics Report, Fraunhofer Institute for Solar Energy Systems", <https://www.ise.fraunhofer.de/de/veroeffentlichungen/studien/photovoltaics-report.html> (2021).
- [37] D. Bonnet and H. Rabenhorst, "New results on the development of a thin film p-CdTe-n-CdS heterojunction solar cell", in In proceedings of the 9th photovoltaic specialists conference, silver spring, md, usa (1972), pp. 129–131.
- [38] A. Supekar, R. Kapadnis, S. Bansode, P. Bhujbal, S. Kale, S. Jadkar, and H. Pathan, "Cadmium Telluride/Cadmium Sulfide Thin Films Solar Cells: A Review", *ES Energy & Environment*, 3–12 (2020).
- [39] J. C. Perrenoud, "Low temperature grown CdTe thin film solar cells for the application on flexible substrates", Dissertation (ETH ZURICH, 2012).
- [40] M. Raugei, S. Bargigli, and S. Ulgiati, "Life cycle assessment and energy pay-back time of advanced photovoltaic modules: CdTe and CIS compared to poly-Si", *Energy* **32**, 1310–1318 (2007).
- [41] B. M. Basol and B. McCandless, "Brief review of cadmium telluride-based photovoltaic technologies", *Journal of Photonics for Energy* **4**, 040996 (2014).
- [42] W. D. Cyrs, H. J. Avens, Z. A. Capshaw, R. A. Kingsbury, J. Sahmel, and B. E. Tvermoes, "Landfill waste and recycling: Use of a screening-level risk assessment tool for end-of-life cadmium telluride (CdTe) thin-film photovoltaic (PV) panels", *Energy Policy* **68**, 524–533 (2014).
- [43] T. D. Lee and A. U. Ebong, "A review of thin film solar cell technologies and challenges", *Renewable and Sustainable Energy Reviews* **70**, 1286–1297 (2017).
- [44] P. Jackson, D. Hariskos, R. Wuerz, O. Kiowski, A. Bauer, T. M. Friedlmeier, and M. Powalla, "Properties of Cu(In,Ga)Se₂ solar cells with new record efficiencies up to 21.7%", *Physica Status Solidi - Rapid Research Letters* **9**, 28–31 (2015).
- [45] K. Maraun, *Solar Frontier Achieves World Record Thin-Film Solar Cell Efficiency: 22.3%*, <https://www.solar-frontier.com/eng/news/2015/C051171.html>, 2015.
- [46] R. Diermann, *Avancis claims 19.64% efficiency for CIGS module*, <https://www.pv-magazine.com/2021/03/04/avancis-claims-19-64-efficiency-for-cigs-module/>, 2021.

- [47] Y. Cai, Y. Li, R. Wang, H. Wu, Z. Chen, J. Zhang, Z. Ma, X. Hao, Y. Zhao, C. Zhang, F. Huang, and Y. Sun, "A Well-Mixed Phase Formed by Two Compatible Non-Fullerene Acceptors Enables Ternary Organic Solar Cells with Efficiency over 18.6%", *Advanced Materials* **33**, 1–9 (2021).
- [48] M. Riede, D. Spoltore, and K. Leo, "Organic Solar Cells—The Path to Commercial Success", *Advanced Energy Materials* **11**, 1–10 (2021).
- [49] W. Shockley and H. Queisser, "Detailed Balance Limit of Efficiency of p–n Junction Solar Cells", in *Renewable energy*, Vol. 2-4, May 1960 (Routledge, Dec. 2018), pp. 35–54.
- [50] M. Saliba, T. Matsui, J. Y. Seo, K. Domanski, J. P. Correa-Baena, M. K. Nazeeruddin, S. M. Zakeeruddin, W. Tress, A. Abate, A. Hagfeldt, and M. Grätzel, "Cesium-containing triple cation perovskite solar cells: Improved stability, reproducibility and high efficiency", *Energy and Environmental Science* **9**, 1989–1997 (2016).
- [51] J.-P. Correa-Baena, A. Abate, M. Saliba, W. Tress, T. Jesper Jacobsson, M. Grätzel, and A. Hagfeldt, "The rapid evolution of highly efficient perovskite solar cells", *Energy Environ. Sci.* **10**, 710–727 (2017).
- [52] M. Saliba, J. P. Correa-Baena, C. M. Wolff, M. Stolterfoht, N. Phung, S. Albrecht, D. Neher, and A. Abate, "How to Make over 20% Efficient Perovskite Solar Cells in Regular (n-i-p) and Inverted (p-i-n) Architectures", *Chemistry of Materials* **30**, 4193–4201 (2018).
- [53] A. D. Taylor, Q. Sun, K. P. Goetz, Q. An, T. Schramm, Y. Hofstetter, M. Litterst, F. Paulus, and Y. Vaynzof, "A general approach to high-efficiency perovskite solar cells by any antisolvent", *Nature Communications* **12**, 1878 (2021).
- [54] T. J. Jacobsson, A. Hultqvist, A. García-Fernández, A. Anand, A. Al-Ashouri, A. Hagfeldt, A. Crovetto, A. Abate, A. G. Ricciardulli, A. Vijayan, A. Kulkarni, A. Y. Anderson, B. P. Darwich, B. Yang, B. L. Coles, C. A. R. Perini, C. Rehermann, D. Ramirez, D. Fairen-Jimenez, D. Di Girolamo, D. Jia, E. Avila, E. J. Juarez-Perez, F. Baumann, F. Mathies, G. S. A. González, G. Boschloo, G. Nasti, G. Paramasivam, G. Martínez-Denegri, H. Näsström, H. Michaels, H. Köbler, H. Wu, I. Benesperi, M. I. Dar, I. Bayrak Pehlivan, I. E. Gould, J. N. Vagott, J. Dagar, J. Kettle, J. Yang, J. Li, J. A. Smith, J. Pascual, J. J. Jerónimo-Rendón, J. F. Montoya, J.-P. Correa-Baena, J. Qiu, J. Wang, K. Sveinbjörnsson, K. Hirslandt, K. Dey, K. Frohna, L. Mathies, L. A. Castriotta, M. H. Aldamasy, M. Vasquez-Montoya, M. A. Ruiz-Preciado, M. A. Flatken, M. V. Khenkin, M. Grischek, M. Kedia, M. Saliba, M. Anaya, M. Veldhoen, N. Arora, O. Shargaieva, O. Maus, O. S. Game, O. Yudilevich, P. Fassel, Q. Zhou, R. Betancur, R. Munir, R. Patidar, S. D. Stranks, S. Alam, S. Kar, T. Unold, T. Abzieher, T. Edvinsson, T. W. David, U. W. Paetzold, W. Zia, W. Fu, W. Zuo, V. R. F. Schröder, W. Tress, X. Zhang,

- Y.-H. Chiang, Z. Iqbal, Z. Xie, and E. Unger, "An open-access database and analysis tool for perovskite solar cells based on the FAIR data principles", *Nature Energy* **7**, 107–115 (2022).
- [55] J. M. White, M. Low, and L. Marshall, *Oxford PV hits new world record for solar cell*, <https://www.oxfordpv.com/news/oxford-pv-hits-new-world-record-solar-cell>, 2020.
- [56] T. Sherahilo, *Perovskite world record*, [https://www.oxfordpv.com/news/\\\$\\backslash\\\$\\backslash\\\$oxford-pv-perovskite-solar-cell-achieves-28-efficiency](https://www.oxfordpv.com/news/\$\\backslash\$\\backslash\$oxford-pv-perovskite-solar-cell-achieves-28-efficiency), 2018.
- [57] K. P. Goetz, A. D. Taylor, Y. J. Hofstetter, and Y. Vaynzof, "Sustainability in Perovskite Solar Cells", *ACS Applied Materials and Interfaces* **13**, 1–17 (2021).
- [58] G. Rose, "In De Novis Quibusdam Fossilibus Quae In Montibus Uraliis Inveniuntur", in *De perowskite, fossili novo*. (1839), pp. 3–5.
- [59] V. M. Goldschmidt, "Die Gesetze der Krystallochemie", *Die Naturwissenschaften* **14**, 477–485 (1926).
- [60] W. Travis, E. N. Glover, H. Bronstein, D. O. Scanlon, and R. G. Palgrave, "On the application of the tolerance factor to inorganic and hybrid halide perovskites: A revised system", *Chemical Science* **7**, 4548–4556 (2016).
- [61] N. D. Marco, H. Zhou, Q. Chen, P. Sun, Z. Liu, L. Meng, E. P. Yao, Y. Liu, A. Schiffer, and Y. Yang, "Guanidinium: A Route to Enhanced Carrier Lifetime and Open-Circuit Voltage in Hybrid Perovskite Solar Cells", *Nano Letters* **16**, 1009–1016 (2016).
- [62] S.-H. Turren-Cruz, A. Hagfeldt, and M. Saliba, "Methylammonium-free, high-performance, and stable perovskite solar cells on a planar architecture", *Science* **362**, 449–453 (2018).
- [63] S. De Wolf, J. Holovsky, S. J. Moon, P. Löper, B. Niesen, M. Ledinsky, F. J. Haug, J. H. Yum, and C. Ballif, "Organometallic halide perovskites: Sharp optical absorption edge and its relation to photovoltaic performance", *Journal of Physical Chemistry Letters* **5**, 1035–1039 (2014).
- [64] G. E. Eperon, S. D. Stranks, C. Menelaou, M. B. Johnston, L. M. Herz, and H. J. Snaith, "Formamidinium lead trihalide: A broadly tunable perovskite for efficient planar heterojunction solar cells", *Energy and Environmental Science* **7**, 982–988 (2014).
- [65] S. D. Stranks, V. M. Burlakov, T. Leijtens, J. M. Ball, A. Goriely, and H. J. Snaith, "Recombination Kinetics in Organic-Inorganic Perovskites: Excitons, Free Charge, and Subgap States", *Physical Review Applied* **2**, 034007 (2014).

- [66] S. D. Stranks, G. E. Eperon, G. Grancini, C. Menelaou, M. J. P. Alcocer, T. Leijtens, L. M. Herz, A. Petrozza, and H. J. Snaith, "Electron-Hole Diffusion Lengths Exceeding 1 Micrometer in an Organometal Trihalide Perovskite Absorber", *Science* **342**, 341–344 (2013).
- [67] K. P. Goetz, A. D. Taylor, F. Paulus, and Y. Vaynzof, "Shining Light on the Photoluminescence Properties of Metal Halide Perovskites", *Advanced Functional Materials* **30**, 1910004 (2020).
- [68] L. M. Herz, "Charge-Carrier Mobilities in Metal Halide Perovskites: Fundamental Mechanisms and Limits", *ACS Energy Letters* **2**, 1539–1548 (2017).
- [69] L. Schmidt-Mende, V. Dyakonov, S. Olthof, F. Ünlü, K. M. T. Lê, S. Mathur, A. D. Karabanov, D. C. Lupascu, L. M. Herz, A. Hinderhofer, F. Schreiber, A. Chernikov, D. A. Egger, O. Shargaieva, C. Cocchi, E. Unger, M. Saliba, M. M. Byranvand, M. Kroll, F. Nehm, K. Leo, A. Redinger, J. Höcker, T. Kirchartz, J. Warby, E. Gutierrez-Partida, D. Neher, M. Stollerfoht, U. Würfel, M. Unmüßig, J. Herterich, C. Baretzky, J. Mohanraj, M. Thelakkat, C. Maheu, W. Jaegermann, T. Mayer, J. Rieger, T. Fauster, D. Niesner, F. Yang, S. Albrecht, T. Riedl, A. Fakharuddin, M. Vasilopoulou, Y. Vaynzof, D. Moia, J. Maier, M. Franckevičius, V. Gulbinas, R. A. Kerner, L. Zhao, B. P. Rand, N. Glück, T. Bein, F. Matteocci, L. A. Castriotta, A. Di Carlo, M. Scheffler, and C. Draxl, "Roadmap on organic-inorganic hybrid perovskite semiconductors and devices", *APL Materials* **9**, 109202 (2021).
- [70] J. Kang and L.-W. Wang, "High Defect Tolerance in Lead Halide Perovskite CsPbBr₃", *The Journal of Physical Chemistry Letters* **8**, 489–493 (2017).
- [71] A. Miyata, A. Mitioglu, P. Plochocka, O. Portugall, J. T.-W. Wang, S. D. Stranks, H. J. Snaith, and R. J. Nicholas, "Direct measurement of the exciton binding energy and effective masses for charge carriers in organic–inorganic tri-halide perovskites", *Nature Physics* **11**, 582–587 (2015).
- [72] S. Tao, I. Schmidt, G. Brocks, J. Jiang, I. Tranca, K. Meerholz, and S. Olthof, "Absolute energy level positions in tin- and lead-based halide perovskites", *Nature Communications* **10**, 2560 (2019).
- [73] F. Bella, P. Renzi, C. Cavallo, and C. Gerbaldi, "Caesium for Perovskite Solar Cells: An Overview", *Chemistry - A European Journal* **24**, 12183–12205 (2018).
- [74] O. A. Syzgantseva, M. Saliba, M. Grätzel, and U. Rothlisberger, "Stabilization of the Perovskite Phase of Formamidinium Lead Triiodide by Methylammonium, Cs, and/or Rb Doping", *The Journal of Physical Chemistry Letters* **8**, 1191–1196 (2017).

- [75] S.-H. Turren-Cruz, M. Saliba, M. T. Mayer, H. Juárez-Santiesteban, X. Mathew, L. Nienhaus, W. Tress, M. P. Erodici, M.-J. Sher, M. G. Bawendi, M. Grätzel, A. Abate, A. Hagfeldt, and J.-P. Correa-Baena, "Enhanced charge carrier mobility and lifetime suppress hysteresis and improve efficiency in planar perovskite solar cells", *Energy & Environmental Science* **11**, 78–86 (2018).
- [76] E. T. Hoke, D. J. Slotcavage, E. R. Dohner, A. R. Bowring, H. I. Karunadasa, and M. D. McGehee, "Reversible photo-induced trap formation in mixed-halide hybrid perovskites for photovoltaics", *Chemical Science* **6**, 613–617 (2015).
- [77] A. J. Knight, A. D. Wright, J. B. Patel, D. P. McMeekin, H. J. Snaith, M. B. Johnston, and L. M. Herz, "Electronic Traps and Phase Segregation in Lead Mixed-Halide Perovskite", *ACS Energy Letters* **4**, 75–84 (2019).
- [78] L. Huang, Z. Hu, J. Xu, K. Zhang, J. Zhang, and Y. Zhu, "Multi-step slow annealing perovskite films for high performance planar perovskite solar cells", *Solar Energy Materials and Solar Cells* **141**, 377–382 (2015).
- [79] S. R. Raga, M.-C. Jung, M. V. Lee, M. R. Leyden, Y. Kato, and Y. Qi, "Influence of Air Annealing on High Efficiency Planar Structure Perovskite Solar Cells", *Chemistry of Materials* **27**, 1597–1603 (2015).
- [80] A. Dualeh, N. Tétreault, T. Moehl, P. Gao, M. K. Nazeeruddin, and M. Grätzel, "Effect of Annealing Temperature on Film Morphology of Organic-Inorganic Hybrid Perovskite Solid-State Solar Cells", *Advanced Functional Materials* **24**, 3250–3258 (2014).
- [81] M. M. Tavakoli, P. Yadav, D. Prochowicz, M. Sponseller, A. Osherov, V. Bulović, and J. Kong, "Controllable Perovskite Crystallization via Antisolvent Technique Using Chloride Additives for Highly Efficient Planar Perovskite Solar Cells", *Advanced Energy Materials* **9**, 1803587 (2019).
- [82] A. Mahapatra, D. Prochowicz, M. M. Tavakoli, S. Trivedi, P. Kumar, and P. Yadav, "A review of aspects of additive engineering in perovskite solar cells", *Journal of Materials Chemistry A* **8**, 27–54 (2020).
- [83] F. Zhang and K. Zhu, "Additive Engineering for Efficient and Stable Perovskite Solar Cells", *Advanced Energy Materials* **10**, 1902579 (2020).
- [84] Y. Vaynzof, "The Future of Perovskite Photovoltaics—Thermal Evaporation or Solution Processing?", *Advanced Energy Materials* **10**, 2003073 (2020).
- [85] D. Huang, P. Xie, Z. Pan, H. Rao, and X. Zhong, "One-step solution deposition of CsPbBr₃ based on precursor engineering for efficient all-inorganic perovskite solar cells", *Journal of Materials Chemistry A* **7**, 22420–22428 (2019).

- [86] Q. An, Q. Sun, A. Weu, D. Becker-Koch, F. Paulus, S. Arndt, F. Stuck, A. S. K. Hashmi, N. Tessler, and Y. Vaynzof, "Enhancing the Open-Circuit Voltage of Perovskite Solar Cells by up to 120 mV Using π -Extended Phosphoniumfluorene Electrolytes as Hole Blocking Layers", *Advanced Energy Materials* **9**, 1901257 (2019).
- [87] Q. Jiang, Z. Chu, P. Wang, X. Yang, H. Liu, Y. Wang, Z. Yin, J. Wu, X. Zhang, and J. You, "Planar-Structure Perovskite Solar Cells with Efficiency beyond 21%", *Advanced Materials* **29**, 1703852 (2017).
- [88] T. Abzieher, F. Mathies, M. Hetterich, A. Welle, D. Gerthsen, U. Lemmer, U. W. Paetzold, and M. Powalla, "Additive-Assisted Crystallization Dynamics in Two-Step Fabrication of Perovskite Solar Cells", *Physica Status Solidi (A) Applications and Materials Science* **214**, 1–9 (2017).
- [89] N. Li, X. Niu, L. Li, H. Wang, Z. Huang, Y. Zhang, Y. Chen, X. Zhang, C. Zhu, H. Zai, Y. Bai, S. Ma, H. Liu, X. Liu, Z. Guo, G. Liu, R. Fan, H. Chen, J. Wang, Y. Lun, X. Wang, J. Hong, H. Xie, D. S. Jakob, X. G. Xu, Q. Chen, and H. Zhou, "Liquid medium annealing for fabricating durable perovskite solar cells with improved reproducibility", *Science* **373**, 561–567 (2021).
- [90] N. J. Jeon, J. H. Noh, Y. C. Kim, W. S. Yang, S. Ryu, and S. I. Seok, "Solvent engineering for high-performance inorganic–organic hybrid perovskite solar cells", *Nature Materials* **13**, 897–903 (2014).
- [91] M. Abbas, L. Zeng, F. Guo, M. Rauf, X. C. Yuan, and B. Cai, "A critical review on crystal growth techniques for scalable deposition of photovoltaic perovskite thin films", *Materials* **13**, 1–42 (2020).
- [92] W. Q. Wu, Q. Wang, Y. Fang, Y. Shao, S. Tang, Y. Deng, H. Lu, Y. Liu, T. Li, Z. Yang, A. Gruverman, and J. Huang, "Molecular doping enabled scalable blading of efficient hole-transport-layer-free perovskite solar cells", *Nature Communications* **9**, 1–8 (2018).
- [93] Y. Deng, E. Peng, Y. Shao, Z. Xiao, Q. Dong, and J. Huang, "Scalable fabrication of efficient organolead trihalide perovskite solar cells with doctor-bladed active layers", *Energy & Environmental Science* **8**, 1544–1550 (2015).
- [94] R. Patidar, D. Burkitt, K. Hooper, D. Richards, and T. Watson, "Slot-die coating of perovskite solar cells: An overview", *Materials Today Communications* **22**, 100808 (2020).
- [95] H. Eggers, F. Schackmar, T. Abzieher, Q. Sun, U. Lemmer, Y. Vaynzof, B. S. Richards, G. Hernandez-Sosa, and U. W. Paetzold, "Inkjet-Printed Micrometer-Thick Perovskite Solar Cells with Large Columnar Grains", *Advanced Energy Materials* **10**, 1903184 (2020).

- [96] J. Gu, G. Yan, Y. Lian, Q. Mu, H. Jin, Z. Zhang, Z. Deng, and Y. Peng, "Bandgap engineering of a lead-free defect perovskite Cs₃Bi₂I₉ through trivalent doping of Ru³⁺", *RSC Advances* **8**, 25802–25807 (2018).
- [97] J. B. Whitaker, D. H. Kim, B. W. Larson, F. Zhang, J. J. Berry, M. F. Van Hest, and K. Zhu, "Scalable slot-die coating of high performance perovskite solar cells", *Sustainable Energy and Fuels* **2**, 2442–2449 (2018).
- [98] Y. Deng, X. Zheng, Y. Bai, Q. Wang, J. Zhao, and J. Huang, "Surfactant-controlled ink drying enables high-speed deposition of perovskite films for efficient photovoltaic modules", *Nature Energy* **3**, 560–566 (2018).
- [99] F. Di Giacomo, S. Shanmugam, H. Fledderus, B. J. Bruijnaers, W. J. Verhees, M. S. Dorenkamper, S. C. Veenstra, W. Qiu, R. Gehlhaar, T. Merckx, T. Aernouts, R. Andriessen, and Y. Galagan, "Up-scalable sheet-to-sheet production of high efficiency perovskite module and solar cells on 6-in. substrate using slot die coating", *Solar Energy Materials and Solar Cells* **181**, 53–59 (2018).
- [100] C. Liang, P. Li, H. Gu, Y. Zhang, F. Li, Y. Song, G. Shao, N. Mathews, and G. Xing, "One-Step Inkjet Printed Perovskite in Air for Efficient Light Harvesting", *Solar RRL* **2**, 1700217 (2018).
- [101] F. Schackmar, H. Eggers, M. Frericks, B. S. Richards, U. Lemmer, G. Hernandez-Sosa, and U. W. Paetzold, "Perovskite Solar Cells with All-Inkjet-Printed Absorber and Charge Transport Layers", *Advanced Materials Technologies* **6**, 2000271 (2021).
- [102] N.-G. Park and K. Zhu, "Scalable fabrication and coating methods for perovskite solar cells and solar modules", *Nature Reviews Materials* **5**, 333–350 (2020).
- [103] C. W. Han and Y. H. Tak, "OLED Manufacturing Process for TV Application", in *Flat panel display manufacturing* (John Wiley & Sons Ltd, Chichester, UK, Aug. 2018), pp. 143–158.
- [104] S. Lobe, A. Bauer, S. Uhlenbruck, and D. Fattakhova-Rohlfing, "Physical Vapor Deposition in Solid-State Battery Development: From Materials to Devices", *Advanced Science* **8**, 2002044 (2021).
- [105] D. Zhao, W. Ke, C. R. Grice, A. J. Cimaroli, X. Tan, M. Yang, R. W. Collins, H. Zhang, K. Zhu, and Y. Yan, "Annealing-free efficient vacuum-deposited planar perovskite solar cells with evaporated fullerenes as electron-selective layers", *Nano Energy* **19**, 88–97 (2016).
- [106] T. Abzieher, T. Feeney, F. Schackmar, Y. J. Donie, I. M. Hossain, J. A. Schwenzler, T. Hellmann, T. Mayer, M. Powalla, and U. W. Paetzold, "From Groundwork to Efficient Solar Cells: On the Importance of the Substrate Material in Co-Evaporated Perovskite Solar Cells", *Advanced Functional Materials* **31**, 2104482 (2021).

- [107] R. Ji, Z. Zhang, C. Cho, Q. An, F. Paulus, M. Kroll, M. Löffler, F. Nehm, B. Rellinghaus, K. Leo, and Y. Vaynzof, "Thermally evaporated methylammonium-free perovskite solar cells", *Journal of Materials Chemistry C* **8**, 7725–7733 (2020).
- [108] M. Kam, Y. Zhu, D. Zhang, L. Gu, J. Chen, and Z. Fan, "Efficient Mixed-Cation Mixed-Halide Perovskite Solar Cells by All-Vacuum Sequential Deposition Using Metal Oxide Electron Transport Layer", *Solar RRL* **3**, 1900050 (2019).
- [109] Y. H. Chiang, M. Anaya, and S. D. Stranks, "Multisource Vacuum Deposition of Methylammonium-Free Perovskite Solar Cells", *ACS Energy Letters* **5**, 2498–2504 (2020).
- [110] L. Gil-Escrig, C. Momblona, M. G. La-Placa, P. P. Boix, M. Sessolo, and H. J. Bolink, "Vacuum Deposited Triple-Cation Mixed-Halide Perovskite Solar Cells", *Advanced Energy Materials* **8**, 1–6 (2018).
- [111] J. Borchert, R. L. Milot, J. B. Patel, C. L. Davies, A. D. Wright, L. Martínez Maestro, H. J. Snaith, L. M. Herz, and M. B. Johnston, "Large-Area, Highly Uniform Evaporated Formamidinium Lead Triiodide Thin Films for Solar Cells", *ACS Energy Letters* **2**, 2799–2804 (2017).
- [112] L. Gil-Escrig, C. Dreessen, I. C. Kaya, B. S. Kim, F. Palazon, M. Sessolo, and H. J. Bolink, "Efficient vacuum-deposited perovskite solar cells with stable cubic FA1-xMAxPbI3", *ACS Energy Letters* **5**, 3053–3061 (2020).
- [113] S.-Y. Hsiao, H.-L. Lin, W.-H. Lee, W.-L. Tsai, K.-M. Chiang, W.-Y. Liao, C.-Z. Ren-Wu, C.-Y. Chen, and H.-W. Lin, "Efficient All-Vacuum Deposited Perovskite Solar Cells by Controlling Reagent Partial Pressure in High Vacuum", *Advanced Materials* **28**, 7013–7019 (2016).
- [114] K. L. Heinze, O. Dolynchuk, T. Burwig, J. Vaghani, R. Scheer, and P. Pistor, "Importance of methylammonium iodide partial pressure and evaporation onset for the growth of co-evaporated methylammonium lead iodide absorbers", *Scientific Reports* **11**, 15299 (2021).
- [115] V. Arivazhagan, J. Xie, Z. Yang, P. Hang, M. M. Parvathi, K. Xiao, C. Cui, D. Yang, and X. Yu, "Vacuum co-deposited CH₃NH₃PbI₃ films by controlling vapor pressure for efficient planar perovskite solar cells", *Solar Energy* **181**, 339–344 (2019).
- [116] J. Borchert, I. Levchuk, L. C. Snoek, M. U. Rothmann, R. Haver, H. J. Snaith, C. J. Brabec, L. M. Herz, and M. B. Johnston, "Impurity Tracking Enables Enhanced Control and Reproducibility of Hybrid Perovskite Vapor Deposition", *ACS Applied Materials & Interfaces* **11**, 28851–28857 (2019).
- [117] *Ross_2020_SI_Co-Evaporated p-i-n Perovskite Solar Cells beyond 20% Efficiency Impact of Substrate Temperature and Hole-Transport Layer-.pdf*.

- [118] B.-S. Kim, L. Gil-Escrig, M. Sessolo, and H. J. Bolink, "Deposition Kinetics and Compositional Control of Vacuum-Processed CH₃NH₃PbI₃ Perovskite", *The Journal of Physical Chemistry Letters* **11**, 6852–6859 (2020).
- [119] J. Ávila, C. Momblona, P. P. Boix, M. Sessolo, and H. J. Bolink, "Vapor-Deposited Perovskites: The Route to High-Performance Solar Cell Production?", *Joule* **1**, 431–442 (2017).
- [120] N. Klipfel, C. Momblona, H. Kanda, N. Shibayama, Y. Nakamura, M. D. Mensi, C. Liu, C. Roldán-Carmona, and M. K. Nazeeruddin, "Crystallographically Oriented Hybrid Perovskites via Thermal Vacuum Codeposition", *Solar RRL* **5**, 2100191 (2021).
- [121] S. Olthof and K. Meerholz, "Substrate-dependent electronic structure and film formation of MAPbI₃ perovskites", *Scientific Reports* **7**, 1–10 (2017).
- [122] K. B. Lohmann, J. B. Patel, M. U. Rothmann, C. Q. Xia, R. D. Oliver, L. M. Herz, H. J. Snaith, and M. B. Johnston, "Control over Crystal Size in Vapor Deposited Metal-Halide Perovskite Films", *ACS Energy Letters* **5**, 710–717 (2020).
- [123] R. Kottokaran, H. A. Gaonkar, H. A. Abbas, M. Noack, and V. Dalal, "Performance and stability of co-evaporated vapor deposited perovskite solar cells", *Journal of Materials Science: Materials in Electronics* **30**, 5487–5494 (2019).
- [124] J. E. Mahan, *Physical vapor deposition of thin films* (Wiley, 2000).
- [125] J. Tauc, R. Grigorovici, and A. Vancu, "Optical Properties and Electronic Structure of Amorphous Germanium", *physica status solidi (b)* **15**, 627–637 (1966).
- [126] HZDR, *X-ray reflectometry*, <https://www.hzdr.de/db/!ContMan.Export.Pdf?p0id=11657&pContLang=de&pNid=309>.
- [127] Zeiss, *Field Emission Scanning Electron Microscope*, <https://www.zeiss.de/mikroskopie/produkte/rasterelektronenmikroskope/sigma.html>, 2022.
- [128] G. Wielgoszewski, *Atomic force microscope*, [https://commons.wikimedia.org/wiki/File:AFM{.}schematic{.}\(EN\).svg](https://commons.wikimedia.org/wiki/File:AFM{.}schematic{.}(EN).svg), 2011.
- [129] K. Ortstein, "Investigations on Energy Level Engineering in Organic Semiconductors", PhD thesis (TU Dresden, 2020).
- [130] S. D. Oez, "Optimization of the co-evaporation of FAPbI₃ perovskite", PhD thesis (University of Cologne, 2021).
- [131] L. Gil-Escrig, C. Dreessen, I. C. Kaya, B.-S. Kim, F. Palazon, M. Sessolo, and H. J. Bolink, "Efficient Vacuum-Deposited Perovskite Solar Cells with Stable Cubic FA_{1-x}MA_xPbI₃", *ACS Energy Letters* **5**, 3053–3061 (2020).

- [132] O. Malinkiewicz, A. Yella, Y. H. Lee, G. M. Espallargas, M. Graetzel, M. K. Nazeeruddin, and H. J. Bolink, "Perovskite solar cells employing organic charge-transport layers", *Nature Photonics* **8**, 128–132 (2014).
- [133] O. Malinkiewicz, A. Yella, Y. H. Lee, G. M. Espallargas, M. Graetzel, M. K. Nazeeruddin, and H. J. Bolink, "Perovskite solar cells employing organic charge-transport layers", *Nature Photonics* **8**, 128–132 (2014).
- [134] W. Rehman, D. P. McMeekin, J. B. Patel, R. L. Milot, M. B. Johnston, H. J. Snaith, and L. M. Herz, "Photovoltaic mixed-cation lead mixed-halide perovskites: links between crystallinity, photo-stability and electronic properties", *Energy & Environmental Science* **10**, 361–369 (2017).
- [135] W. Nie, H. Tsai, J.-C. Blancon, F. Liu, C. C. Stoumpos, B. Traore, M. Kepenekian, O. Durand, C. Katan, S. Tretiak, J. Crochet, P. M. Ajayan, M. Kanatzidis, J. Even, and A. D. Mohite, "Critical Role of Interface and Crystallinity on the Performance and Photostability of Perovskite Solar Cell on Nickel Oxide", *Advanced Materials* **30**, 1703879 (2018).
- [136] T. J. Jacobsson, J.-P. Correa-Baena, E. Halvani Anaraki, B. Philippe, S. D. Stranks, M. E. F. Bouduban, W. Tress, K. Schenk, J. Teuscher, J.-E. Moser, H. Rensmo, and A. Hagfeldt, "Unreacted PbI₂ as a Double-Edged Sword for Enhancing the Performance of Perovskite Solar Cells", *Journal of the American Chemical Society* **138**, 10331–10343 (2016).
- [137] D. P. McMeekin, G. Sadoughi, W. Rehman, G. E. Eperon, M. Saliba, M. T. Hörantner, A. Haghighirad, N. Sakai, L. Korte, B. Rech, M. B. Johnston, L. M. Herz, and H. J. Snaith, "A mixed-cation lead mixed-halide perovskite absorber for tandem solar cells", *Science* **351**, 151–155 (2016).
- [138] O. Telschow, M. Albaladejo-Siguan, L. Merten, A. D. Taylor, K. P. Goetz, T. Schramm, O. V. Konovalov, M. Jankowski, A. Hinderhofer, F. Paulus, F. Schreiber, and Y. Vaynzof, "Preserving the stoichiometry of triple-cation perovskites by carrier-gas-free antisolvent spraying", *Journal of Materials Chemistry A, Advance Article* (2022).
- [139] K. A. Bush, K. Frohna, R. Prasanna, R. E. Beal, T. Leijtens, S. A. Swifter, and M. D. McGehee, "Compositional Engineering for Efficient Wide Band Gap Perovskites with Improved Stability to Photoinduced Phase Segregation", *ACS Energy Letters* **3**, 428–435 (2018).
- [140] Y. H. Chiang, M. Anaya, and S. D. Stranks, "Multisource Vacuum Deposition of Methylammonium-Free Perovskite Solar Cells", *ACS Energy Letters* **5**, 2498–2504 (2020).

- [141] D. Luo, W. Yang, Z. Wang, A. Sadhanala, Q. Hu, R. Su, R. Shivanna, G. F. Trindade, J. F. Watts, Z. Xu, T. Liu, K. Chen, F. Ye, P. Wu, L. Zhao, J. Wu, Y. Tu, Y. Zhang, X. Yang, W. Zhang, R. H. Friend, Q. Gong, H. J. Snaith, and R. Zhu, "Enhanced photovoltage for inverted planar heterojunction perovskite solar cells", *Science* **360**, 1442–1446 (2018).
- [142] T. T. Ava, A. Al Mamun, S. Marsillac, and G. Namkoong, "A review: Thermal stability of methylammonium lead halide based perovskite solar cells", *Applied Sciences (Switzerland)* **9**, 188 (2019).
- [143] A. Latini, G. Gigli, and A. Ciccioli, "A study on the nature of the thermal decomposition of methylammonium lead iodide perovskite, $\text{CH}_3\text{NH}_3\text{PbI}_3$: an attempt to rationalise contradictory experimental results", *Sustainable Energy & Fuels* **1**, 1351–1357 (2017).
- [144] G. Divitini, S. Cacovich, F. Matteocci, L. Cinà, A. Di Carlo, and C. Ducati, "In situ observation of heat-induced degradation of perovskite solar cells", *Nature Energy* **1**, 15012 (2016).
- [145] J. Borchert, H. Boht, W. Fränzel, R. Csuk, R. Scheer, and P. Pistor, "Structural investigation of co-evaporated methyl ammonium lead halide perovskite films during growth and thermal decomposition using different PbX_2 ($X = \text{I}, \text{Cl}$) precursors", *Journal of Materials Chemistry A* **3**, 19842–19849 (2015).
- [146] Z. Song, A. Abate, S. C. Watthage, G. K. Liyanage, A. B. Phillips, U. Steiner, M. Graetzel, and M. J. Heben, "Perovskite Solar Cell Stability in Humid Air: Partially Reversible Phase Transitions in the $\text{PbI}_2\text{-CH}_3\text{NH}_3\text{-H}_2\text{O}$ System", *Advanced Energy Materials* **6**, 1600846 (2016).
- [147] N. Aristidou, I. Sanchez-Molina, T. Chotchuangchutchaval, M. Brown, L. Martinez, T. Rath, and S. A. Haque, "The Role of Oxygen in the Degradation of Methylammonium Lead Trihalide Perovskite Photoactive Layers", *Angewandte Chemie* **127**, 8326–8330 (2015).
- [148] B. Conings, J. Drijkoningen, N. Gauquelin, A. Babayigit, J. D'Haen, L. D'Olieslaeger, A. Ethirajan, J. Verbeeck, J. Manca, E. Mosconi, F. De Angelis, and H. G. Boyen, "Intrinsic Thermal Instability of Methylammonium Lead Trihalide Perovskite", *Advanced Energy Materials* **5**, 1–8 (2015).
- [149] E. J. Juarez-Perez, Z. Hawash, S. R. Raga, L. K. Ono, and Y. Qi, "Thermal degradation of $\text{CH}_3\text{NH}_3\text{PbI}_3$ perovskite into NH_3 and CH_3I gases observed by coupled thermogravimetry–mass spectrometry analysis", *Energy & Environmental Science* **9**, 3406–3410 (2016).

- [150] J. W. Lee, D. H. Kim, H. S. Kim, S. W. Seo, S. M. Cho, and N. G. Park, "Formamidinium and cesium hybridization for photo- and moisture-stable perovskite solar cell", *Advanced Energy Materials* **5**, 1501310 (2015).
- [151] E. J. Juarez-Perez, L. K. Ono, and Y. Qi, "Thermal degradation of formamidinium based lead halide perovskites into sym-triazine and hydrogen cyanide observed by coupled thermogravimetry-mass spectrometry analysis", *Journal of Materials Chemistry A* **7**, 16912–16919 (2019).
- [152] G. Kieslich, S. Sun, and A. K. Cheetham, "An extended Tolerance Factor approach for organic–inorganic perovskites", *Chemical Science* **6**, 3430–3433 (2015).
- [153] M. Roß, S. Severin, M. B. Stutz, P. Wagner, H. Köbler, M. Favin-Lévêque, A. Al-Ashouri, P. Korb, P. Tockhorn, A. Abate, B. Stannowski, B. Rech, and S. Albrecht, "Co-Evaporated Formamidinium Lead Iodide Based Perovskites with 1000 h Constant Stability for Fully Textured Monolithic Perovskite/Silicon Tandem Solar Cells", *Advanced Energy Materials* **11**, 2101460 (2021).
- [154] P. Fassel, V. Lami, A. Bausch, Z. Wang, M. T. Klug, H. J. Snaith, and Y. Vaynzof, "Fractional deviations in precursor stoichiometry dictate the properties, performance and stability of perovskite photovoltaic devices", *Energy and Environmental Science* **11**, 3380–3391 (2018).
- [155] B. Dänekamp, C. Müller, M. Sendner, P. P. Boix, M. Sessolo, R. Lovrincic, and H. J. Bolink, "Perovskite–Perovskite Homojunctions via Compositional Doping", *The Journal of Physical Chemistry Letters* **9**, 2770–2775 (2018).
- [156] X. Zhao, T. Liu, Q. C. Burlingame, T. Liu, R. Holley, G. Cheng, N. Yao, F. Gao, and Y.-L. Loo, "Accelerated aging of all-inorganic, interface-stabilized perovskite solar cells", *Science* **5679**, 1–10 (2022).
- [157] Z. Zhang, R. Ji, M. Kroll, Y. J. Hofstetter, X. Jia, D. Becker-Koch, F. Paulus, M. Löffler, F. Nehm, K. Leo, and Y. Vaynzof, "Efficient Thermally Evaporated γ -CsPbI₃ Perovskite Solar Cells", *Advanced Energy Materials* **11**, 2100299 (2021).

Danksagung

Zu guter Letzt möchte ich mich bei allen Bedanken die zum Gelingen dieser Arbeit beigetragen haben. Als allererstes möchte ich Karl Leo danken, für das Ermöglichen dieser Promotion und weiterhin für die hervorragende Betreuung im Verlauf. Mit seiner fördernden Art hat er mich durch viele erfolglose und auch einige erfolgreiche Projekte geleitet. Das Vertrauen das mir entgegengebracht wurde, hat mich mit den Aufgaben wachsen lassen und sehr viel gelehrt.

Außerdem möchte ich allen Post-Docs danken die mich auf dem Weg begleitet haben. Sie sind mir immer mit ihrer Erfahrung zur Seite gestanden, hatten immer ein offenes Ohr und haben mit sinnvolle Ratschläge nicht gespart. Angefangen mit Freddi und Changsoon, über Alex und Katelyn, sowie Axel, Johannes, Reinhard, Markas und insbesondere Hans. Desweiteren möchte ich Yana für ihre unglaubliche Expertise, zahlreichen Ideen, Liz für die vielen Korrekturen und der gesamten Emsol-Gruppe für die gute Zusammenarbeit Danken. Natürlich möchte ich auch der PeroVap-Gruppe um Freddi, Ran, Zongbao, Changsoon, Tim und Tobias für viele Stunden gemeinsames Putzen, Reparieren und Verdampfen meinen Dank aussprechen. Außerdem möchte ich allen Kollegen der Ergeschoßlabore um Katrin, Steffi, den ODSlern und insbesondere Jörn für die Unterstützung an all den guten und den schlechten Tagen, d sowieso allen Mitarbeitern des Instituts, wie Fanny, Angelika, Annette, Thomas, Peter und Kai, Paulius, Marco, Dinara und allen Anderen danken. Es war eine hervorragende Zeit, die ich nicht missen möchte und wir sehen uns bald auf ein Freitagsbier.

Bedanken möchte ich mich auch bei Frank Schreiber für die Übernahme des zweiten Gutachten und seinen Kollegen Alex und Lena für die hervorragende Zusammenarbeit und die gute Zeit in Hamburg. Desweiteren möchte ich Selina für die vielen Tipps, die Aufnahme in die "Verdampfer"-community und die vielen Ratschläge und Diskussionen, vom Anfang in Regensburg bis zur Fertigstellung des Papers danken.

Natürlich möchte ich noch allen Freunden, die mich außerhalb der Arbeit auf dem langen Weg unterstützt und mir das Leben zur Freude gemacht haben danken. Den "Physikern", Robert, Lukas, Kravitz, Max, Mo und Felix. Den "Münchnern", den "Regensburgern", den "Nittendorfern" und allen die nirgendwo genau dazu gehören wie Martin, Lion, Anete, Mo, Lea, Franzy, Emely, Paul und so vielen mehr.

Zu guter Letzt möchte ich meiner Familie, meinen Geschwistern und insbesondere meinen Eltern für alles und noch mehr von Herzen Danken.

Erklärung

Hiermit versichere ich, dass ich die vorliegende Arbeit zum Thema:

Physical vapour deposition of Perovskite for solar cell application

ohne unzulässige Hilfe Dritter und ohne Benutzung anderer als der angegebenen Hilfsmittel angefertigt habe. Die aus fremden Quellen direkt oder indirekt übernommenen Gedanken sind als solche kenntlich gemacht. Die Arbeit wurde bisher weder im Inland noch im Ausland in gleicher oder ähnlicher Form einer anderen Prüfungsbehörde vorgelegt. Weiterhin versichere ich, dass bisher kein Promotionsverfahren stattgefunden hat.

Diese Dissertation wurde am *Institut für angewandte Physik* der Technischen Universität Dresden unter wissenschaftlicher Betreuung von *Prof. Dr. Karl Leo* angefertigt.

Ich erkenne die Promotionsordnung des Bereiches Mathematik und Naturwissenschaften an der Technischen Universität Dresden vom 23.02.2011 in geänderter Fassung vom 23.05.2018 an.

Martin Kroll

Dresden, am 19. Juli, 2022